SANDIA REPORT

SAND2019-1037
Unlimited Release
Printed January 2019

November 2016 HERMES Outdoor Shot Series 10268-313: Air Conductivity Measurements

Benjamin T. Yee, Keith L. Cartwright

Prepared by
Sandia National Laboratories
Albuquerque, New Mexico 87185 and Livermore, California 94550

Sandia National Laboratories is a multimission laboratory managed and operated by National Technology & Engineering Solutions of Sandia, LLC, a wholly owned subsidiary of Honeywell International, Inc., for the U.S. Department of Energy's National Nuclear Security Administration under contract DE-NA-0003525.

Sandia National Laboratories

Issued by Sandia National Laboratories, operated for the United States Department of Energy by Sandia Corporation.

Available to DOE and DOE contractors from
U.S. Department of Energy
Office of Scientific and Technical Information
P.O. Box 62
Oak Ridge, TN 37831

Telephone: (865) 576-8401
Facsimile: (865) 576-5728
E-Mail: reports@adonis.osti.gov
Online ordering: http://www.osti.gov/bridge

Available to the public from
U.S. Department of Commerce
National Technical Information Service
5285 Port Royal Rd
Springfield, VA 22161

Telephone: (800) 553-6847
Facsimile: (703) 605-6900
E-Mail: orders@ntis.fedworld.gov
Online ordering: http://www.ntis.gov/help/ordermethods.asp?loc=7-4-0#online

SAND2019-1037
Unlimited Release
Printed January 2019

November 2016 HERMES Outdoor Shot Series 10268-313: Air Conductivity Measurements

Benjamin T. Yee
Applied Optical and Plasma Sciences
Sandia National Laboratories
P.O. Box 5800
Albuquerque, NM 87185-1423
btyee@sandia.gov

Keith L. Cartwright
Electromagnetic Theory
Sandia National Laboratories
P.O. Box 5800
Albuquerque, NM 87185-1152
klcartw@sandia.gov

Acknowledgments

We gratefully acknowledge Cheryl Lam, Bryan Oliver, Estevan Sisneros, Olga Lavrova, Renee Gooding, Sean Coffey, Debra Kirschner, Gary Tilley, Joe Stewart, Tom Zarick, Jarod Delhotal, Joe Rudys, Forest (Gene) White, Barbara Lewis, Steve Glover, Mike Dinallo, Tim Pointon, Iain Thurston, Rob Beacham, Georgia Wright, and Michael Moutrie for their support of the experiment. We gratefully acknowledge Larry Bacon and Pat Griffin for insight in interpreting the results.

Contents

Appendix

List of Figures

Nomenclature

ABS Acrylonitrile Butadiene Styrene

CAD Computer Aided Design

HERMES High-Energy Radiation Megavolt Electron Source

Hz Hertz

EMI ElectroMagnetic Interference

EMP ElectroMagnetic Pulse

EM ElectroMagnetic

RF Radio Frequency

MITL Magnetically Insulated Transmission Line

PPD Parallel Plate Dipole

SCD Spherical Compton Diode

SMA SubMiniature versionA

This page intentionally left blank.

Introduction

Of specific concern to this report and the related experiments is ionization of air by gammas rays and the cascading electrons in the High-Energy Radiation Megavolt Electron Source (HERMES) III courtyard. When photons generated by HERMES encounter a neutral atom or molecule, there is a chance that they will interact via one of several mechanisms: photoelectric effect, Compton scattering, or pair production.

In both the photoelectric effect and Compton scattering, an electron is liberated from the atom or molecule with a direction of travel preferentially aligned with the gamma ray. This results in a flow of electrons away from the source region, which results in large scale electric and magnetic fields. The strength of these fields and their dynamics are dependent on the conductivity of the air. A more comprehensive description is provided by Longmire and Gilbert [1].

As the conductivity of air helps to determine the strength of the electromagnetic fields, it is critical to develop an understanding of its magnitude and evolution. The complex interplay of the gamma ray flux, the character of the electron beam it produces, and the resulting free charges make this task challenging. Predictive understanding of this phenomena relies on the measurement and simulation of devices designed to create comparable conditions. By confirmation of the air conductivity in experiment, greater confidence can be placed in simulation capabilities.

Sandia National Laboratories (SNL) hosts the HERMES accelerator which provides the opportunity to make such measurements. At its core, HERMES is a pulsed power machine which accelerates electrons to energies of up to 20 MeV and guides them into a target, called a converter, composed of tantalum. The slowing the electrons in this target generates a broad spectrum of gamma rays (or more technically, x-rays, as they do not originate from nuclear processes) which are released into an indoor test cell or an outdoor test area.

In the November 2016 a series of 45 shots on HERMES were taken over a period of two weeks for the. During this time HERMES was configured to emit a 20 ns gamma ray pulse into the outdoor test area. Several experiments were fielded in the test area as well as many sensors intended to characterize the environment generated by HERMES. Among the fielded sensors were so-called "pie pan" sensors, designed to measure the local magnitude and evolution of the conductivity. This report concerns the design, implementation, and analysis of these sensors. The outcome of this work is an improved understanding of the operation of these sensors and estimates of the conductivity in the courtyard, simultaneous to the measurement of other critical quantities.

In this report, we first describe the relevant experimental conditions, the sensors used, and their location during the trials. After that, the signal processing and analysis of the current and field sensor results are both described. Then, results from the trial are discussed, addressing the new sensors, the effect of partially closed doors, radiation driven currents, and other topics. Finally, this report concludes with several recommendations for the improvement of the conductivity measurements.

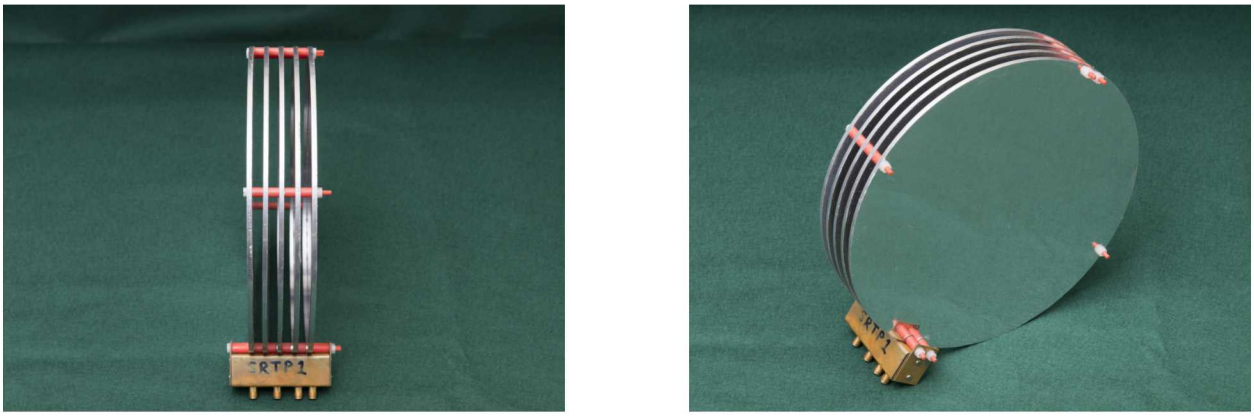

Figure 1: Photographs of the original pie pan sensor.

Equipment

Conductivity Sensors

The conductivity of the air in the courtyard was measured using two pie pan sensors of an older design, two new pie pan sensors, and two mesh pie pans. Figure 1 includes two photographs of the original pie pan sensor. These sensors were originally created for the previous set of trials at HERMES which ran from 1994 through 1997. Scant information is available regarding the design, operation, and analysis of these sensors. Examination of EMP sensor literature shows that though they closely resemble radiation-hardened parallel plate dipoles [2].

The two older-style sensors fielded for these trials had model numbers of SRTP2,and SRTP3. In the trials, they were designated 702PP and 703PP respectively and will be referred to as the 700-series pie pans. The primary components of each sensor are its five plates from which its name derives. These plates are composed of an aluminum ring which acts as a mechanical support and electrical connection. The outer diameter of each ring is 212 mm and the inner diameter is 200 mm. The thickness of each ring is 3.27 mm.

Held taught across each ring is a thin sheet of aluminum with a thickness of 35 μm. The aluminum sheet is affixed to the ring with a conductive epoxy. This sheet proved to be very delicate during the course of the trials. Each ring features four through-holes equally spaced about the perimeter. These holes allow the five individual plates to be joined by plastic spacers. On one side, an additionally through hole is provided for mounting of the sensing circuitry, describe below. The spacing between the plates is 10 mm.

On one side of the rings a copper box is attached containing the sensing circuitry for the plates. Figure 2 is a photograph of the sensing circuitry. The pie pan can essentially be divided into two sets of sensors, one set for the electric field, and one set for the current driven by the field. The three plates on the left hand side in Figure 2 comprise two electric field sensors. The middle plate is connected to the circuit box (chassis ground) while the other two plates are soldered to the center conductor of SMA connectors in series with 5.1 kΩ resistors. This forms a resistive divider in

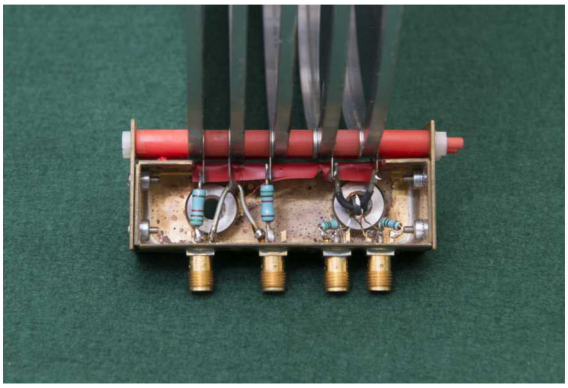

Figure 2: Photograph of the sensing circuitry for the pie-pan sensors.

concert with the impedance of the attached cable.

The two plates on the right hand side sense the current driven by the ambient field and the gamma flux. The plates are connected together via a hand-built balun and dc-block, formed by an insulated wire passed through a ferrite core, forming one leg of a transformer. The other leg of the transformer is formed by two wires each wrapped around the core approximately four times. One end of each wire is soldered to the center conductor of its own SMA connector, while the opposite end is soldered to ground. In parallel for each wire is a 51 Ω resistor.

From an theoretical standpoint, the newer pie pans are intended to be identical to the legacy versions. However, several changes were made to improve more practical aspects of their usage. The circuit was transitioned from hand-soldered connections to a printed circuit board. The box housing the circuitry was constructed of machined aluminum instead of copper sheet. Provisions were made for easier removal of damaged plates. Despite these changes, the response of these sensors are expected to be identical to the 700-series.

In contrast to the 700-series, the mesh designs fielded in the November 2016 trials were not differential. Instead, a single pair of plates was used to measure both the electric fields and the currents. The intent of this design change was to simplify construction, reduce material subject to radiation drive, and ease analysis of the sensors. The use of non-differential signals rests on the assumption that common mode signal rejection is not necessary.

The foundation of the mesh sensors was a 3D-printed ABS support structure, seen on the left of Figure 3. The two plates are separated by 10 mm and the diameter of the sensor is approximately 111 mm, yielding a total area of 0.01 m^2. All metal components of the sensor, with the exception of the circuit components, are made of aluminum in order to inhibit the radiation drive on the sensor. In many of the tests, an aluminum mesh was used instead of a continuous piece of foil or plate. Previous work [3] suggested that a mesh may provide an electrically equivalent surface, while reducing the system-generated electromagnetic pulse (SGEMP) response of the sensor.

Glued to the bottom of the support structure was an aluminum box, with approximate outer dimensions of 12 mm by 12 mm by 50 mm. Inside the field sensing version of the mesh sensor, a high precision potentiometer (Vishay VFR 1240) with low inductance (0.08 μH) and low capacitance

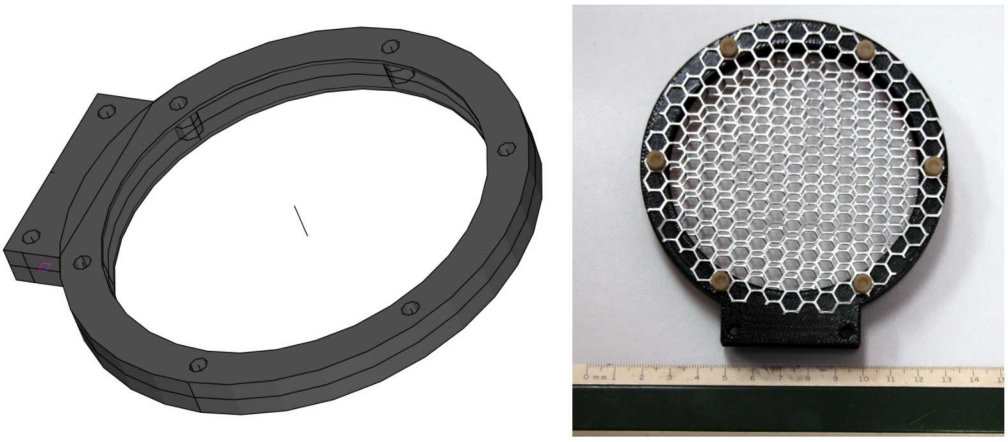

Figure 3: CAD rendering of support structure for mesh sensors (left) and the sensor with the mesh plates in place.

(0.5 pF) was set to 5.1 kΩ and connected in series with one of the plates to the center conductor of an SMA connector. The other plate was attached to the outer conductor and chassis ground. The current sensing version of the mesh sensor a Pulse Electronics PE-65968NL transformer as a balun which had a nominal bandwidth of 500 MHz.

Signal Acquisition

Each set of conductivity sensors was connected to the local screen room of the HERMES III facility via long runs of coaxial cable. The mesh sensors, the 703 sensor, and the PP-16 sensors were all connected to the local screen room by 60 ft of RGA-402 followed by 60 ft of LMR-240. In contrast, the 702 sensors was connected by 80 ft of RGA-402 followed by 60 ft of LMR-240.

Once inside the local screen room, the individual sensor channels were connected to Tektronix 011 attenuators. The individual attenuation values were changed depending on signal strength in order to maximize the dynamic range of the signal without clipping. The PP-16-3, mesh sensors, and 702 sensors were recorded using Tektronix DPO 5204B oscilloscopes which possess a bandwidth of 2 GHz. The PP-16-4 and 703 sensor are recorded using Tektronix DPO 4104B oscilloscopes which have a 1 GHz bandwidth.

Locations

Figure 4 displays the locations of each set of conductivity sensors throughout the trials. The origin of the coordinate system used in this report is located at ground level, immediately below the converter of HERMES III. The z-axis is parallel to the central axis of HERMES (the "beam axis") and the positive x direction is toward the open side of the courtyard. During most of shots, the 703 sensor and the mesh sensors were placed symmetrically about the beam axis so that the two could later be compared. Meanwhile, the 702 sensor was always adjacent to the canonical shape that was

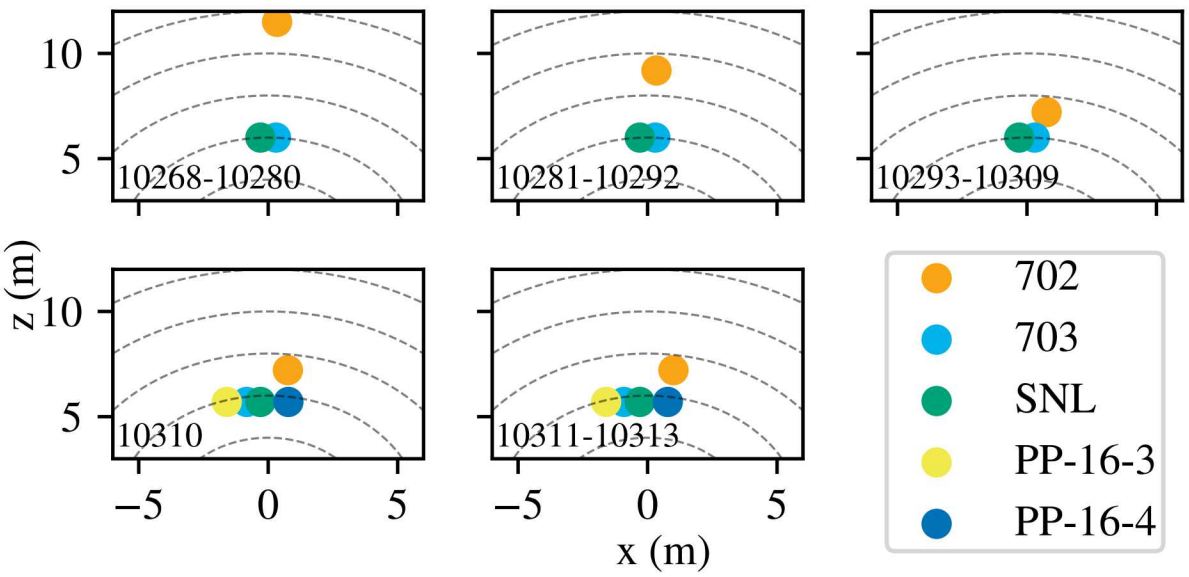

Figure 4: Locations of the conductivity sensors.

fielded as part of the trials. As a result, the 702 sensor moved progressively closer to the HERMES III converter over the course of the trials. During the final four shots, the new sensors were fielded near the 703 and mesh sensors so that comparisons could later be made.

With the exception of the 702 sensor, all conductivity sensors were placed at a height of 1 m. The 702 sensor was set at a height of 0.87 m, corresponding to the height of the canonical shape's central axis. The sensors were mounted on Delrin shelves, attached to fiberglass I-beams, as seen in Figure 5. The mesh sensors also used additional fiberglass angle stock in their mounting. All connections to coaxial cables featured additional EMI shielding in the former of copper wool and aluminum foil. Copper braid was also used along much of the length of the coaxial cables to provide further protection from interference.

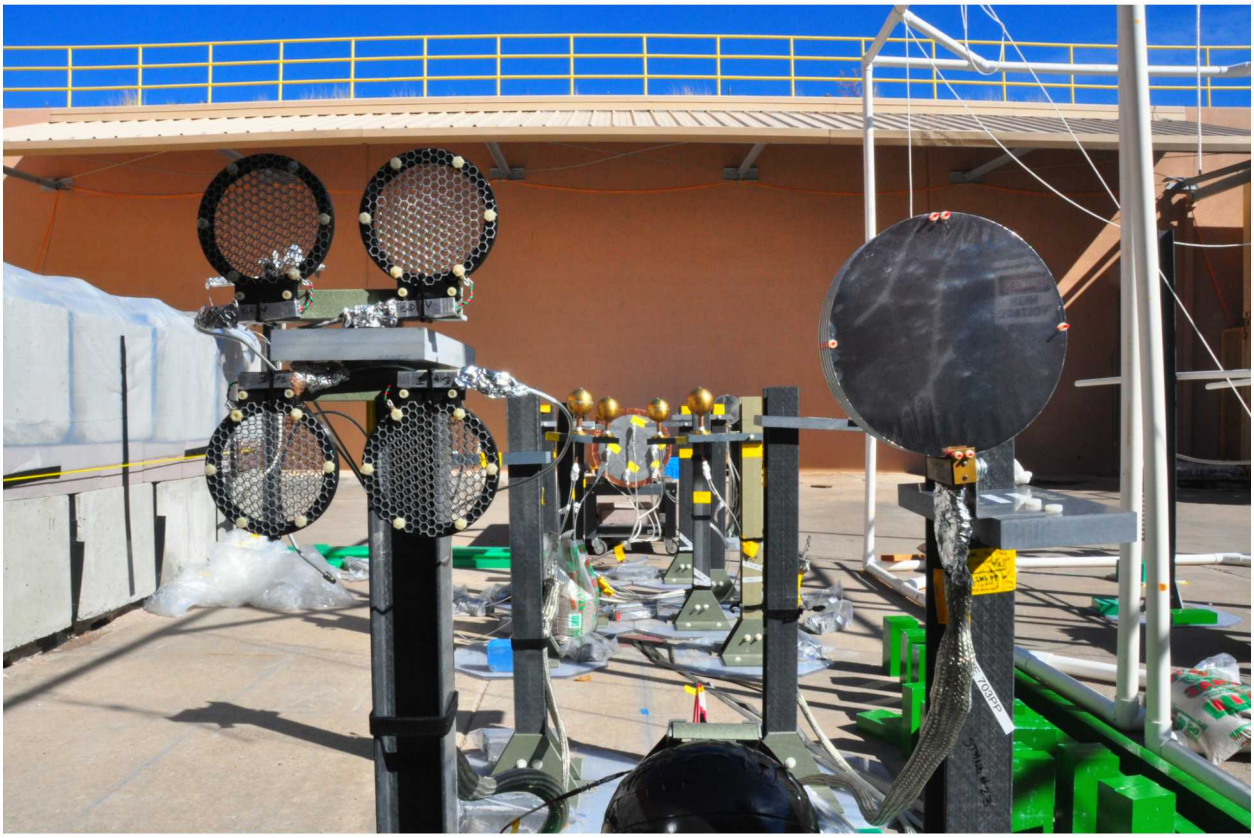

Figure 5: Photograph of the mesh conductivity sensors and the 703 pie pan sensor on their mounting stands.

Signal Analysis

The signals from the conductivity sensors were processed in a similar manner to that described in the report on the spherical Compton diodes from this same series. Briefly, each signal was first compensated for the frequency-dependent attenuation in the coaxial cables connecting the sensor to the local screen room. The compensation used was an analytic approach developed by Boyer [4] which was found to adequately recover sub-nanosecond step functions from pre-trial measurements. That said, this compensation method also leads to strong amplification of digitizer noise at high frequencies (greater than 1 GHz). In order to suppress the compensation noise and to eliminate frequencies where the current sensors were nonlinear, a fifth-order Butterworth filter was subsequently applied with a cutoff frequency of 800 MHz.

In the present analysis, several potentially important factors are neglected. Firstly, though Boyer describes variations of up to 10% between cables of identical construction, all cables of similar construction are treated the same in this analysis. Furthermore, the attenuators used during the course of the trials were assumed to be accurate to their stated value and to have a flat response across all frequencies in question. Unlike other sensors, no the conductivity signals were not split and therefore there was no concern about the frequency response of power splitters.

As with the analyses presented in other reports, all time values (unless otherwise mentioned) refer to retarded time with respect to radiation emission from the HERMES III converter. Corrections are made for jitter in the firing of HERMES III with respect to the facility trigger signal, for time of flight in the cables, and for the distance of the sensors from the converter. In the case of sensor 703, the signals were offset by 29.6 μs for some shots relative to the other conductivity sensors. A similar offset was observed in several of the field and current sensors. While the origin of this offset is unknown, a manual correction is made for it in this report.

Unlike many of the sensors in the courtyard, none of the conductivity sensors featured witness lines. That said, the differential nature of the original sensors meant that any common mode signal (for example, radiation drive) could easily be subtracted out. To illustrate the steps involved in signal processing, Figure 6 shows the progression from the raw signal to the filtered version used to determine the electric fields and current densities for sensor 703 from shot 10308. The attenuation of the signal cables at the frequencies in the field sensors is particularly strong, leading to approximately a factor of two difference between the compensated and uncompensated signals. While not as extreme, the current signal also sees a significant change in its amplitude due to the compensation. The peak amplitudes for the field sensors are reduced somewhat due to the use of the 800 MHz low pass filter, but these values should be a significant improvement over the originals.

Also shown in Figure 6 are the individual channels of the differential field and current sensors. As mentioned above, a simple subtraction of the two channels (divided by two) should be sufficient to eliminate common mode signals, while retaining the intended signal. From this, we can conclude that the field sensors are subject to a great deal of common mode noise, so much that the desired signal is dwarfed by the noise. By comparison, the current signals are well-balanced, exhibiting relatively little common mode noise.

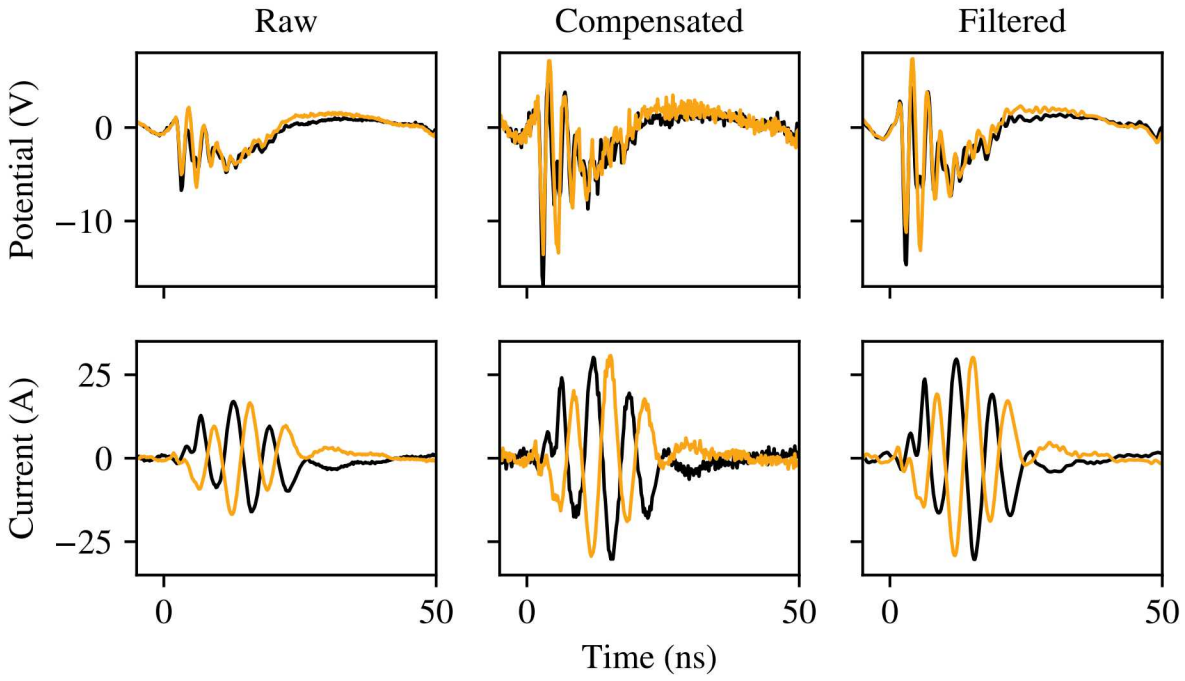

Figure 6: Steps in the analysis of the 703 sensor from shot 10308.

Electric Field Sensors

The electric field sensors and associated resistive dividers are a form of the parallel plate dipole (PPD) sensor. Though variations of such a sensor have been used as far back as 1916 [5], the application to EMP environments is clearly more recent. The modern analyses of these sensors is largely recorded in the "Sensor and Simulation Notes" series, edited by Baum [6, 3, 7, 8, 9, 10, 2].

PPD sensors have been frequently used in the study of both EMPs and lightning [11, 12, 13, 14, 15, 16]. The geometry employed in the original pie pan sensors most closely resemble the double-ended, differential sensor described in [2]. As described in [8], the dipole responds to waves propagating parallel to the normal of the plate surface at arbitrarily high frequencies. Wave components perpendicular to surface normal will not induce an electrical signal.

A theoretical circuit model for the PPD component of the pie pan sensor can be seen in Figure 7. In this figure $\mathbf{E}$ is the time-dependent electric field, $\mathbf{l_{eq}}$ is the equivalent height of the sensor, C_s is the capacitance of the plates, Z is the load impedance, and V_o is the output voltage (sensed by the digitizer). $G_s(t,E)$ is the conductance of the capacitor in the special case that the air is ionized. For our analysis, the air conductivity will be assumed to be negligibly small for the field sensor's operation. As will be shown later, the maximum expected conductivity is 0.58 mS/m. At this level, the conductivity between the plates cannot be considered negligible, however high levels of conductivity are expected to last only momentarily.

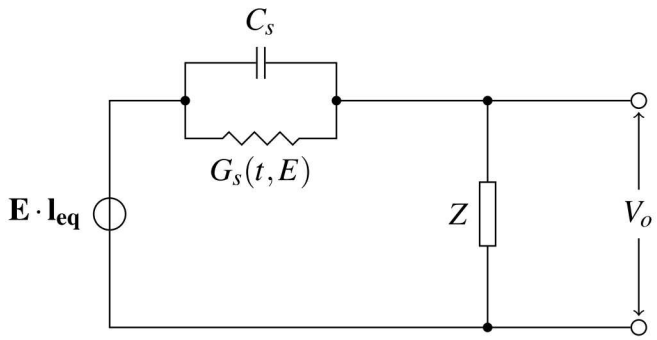

Figure 7: Thévenin equivalent circuit for one half of the differential field sensor employed in the original pie pans.

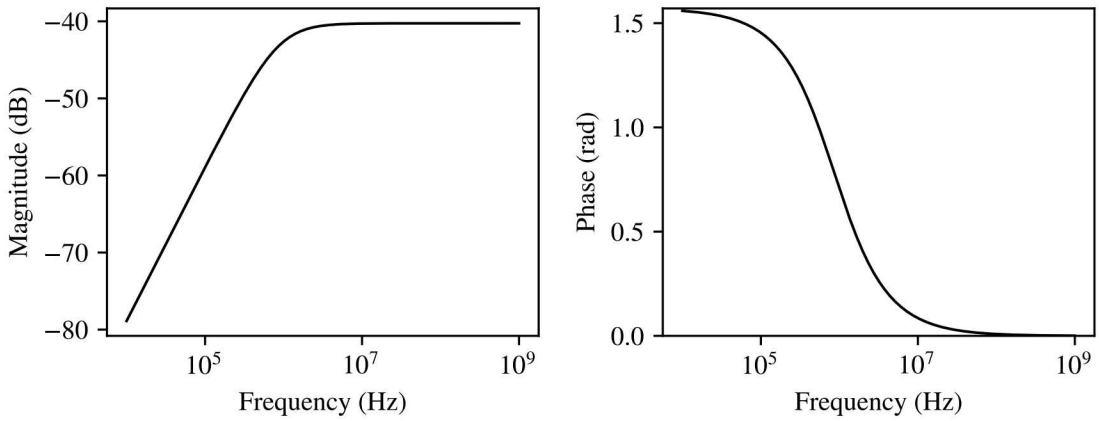

Figure 8: Theoretical frequency response of a PPD field sensor assuming no conductivity.

If $G_s(t,E) = 0$, then the circuit behaves as a high pass voltage divider. In the frequency domain, the response can be represented as [2]

$$\tilde{V}_o(s) = -\tilde{\mathbf{E}}(s)\cdot\mathbf{l_{eq}}\frac{Z}{R+Z}\frac{sC_s(Z+R)}{sC_s(Z+R)+1}. \tag{1}$$

Here, s is the complex frequency, $j\omega$, and the tilde represents a Laplace-transformed quantity. Here, R is the load resistance and Z is the characteristic impedance of the connecting cable. Figure 8 is a Bode plot of the field sensor response for values of C_s, Z, and R which are representative of the 700-series pie pan sensors used in these trials. The value of C_s (36.2 pF) is calculated using the asymptotic formula of Hutson and Ursell [17] for a large disk radius relative separation.

The characteristic frequency of the high pass filter displayed in Figure 8 is $1/((Z+R)C_s)$, or 8.5 MHz for the original sensors (1.6 MHz for the mesh sensors). For frequencies significantly below this value, the measured output voltage, V_o, is proportional to the frequency of the applied field. This is the regime in which a conventional D-dot sensor operates. For this report, we will focus on the response of the sensor at frequencies higher than the high pass filter cutoff where the output voltage is strictly proportional to the applied field. For both the original and mesh sensors,

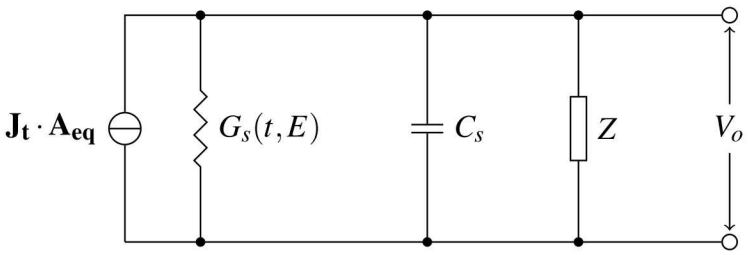

Figure 9: Norton equivalent circuit used in the basic analysis of the current sensor response.

the electric field can be found from the equation $|\mathbf{E} \cdot \hat{z}| = 10^{-2} V_o/h$.

Current Sensors

While geometrically identical, the current sensors drive a substantially different load than the field sensors which allows them to sense the current (displacement and actual) driven by the field [7]. The design of the current sensors is similar to that used for ion chambers [18], a fact acknowledged in other studies [19, 20]. The crucial difference from the present studies is that the current sensors of the pie pan are not active devices, that is, there is no externally applied potential.

Figure 9 shows the Norton equivalent circuit for a current sensor. In the limit that $Z \ll 1/G$ (and a small RC), the current in this circuit is simply $I = JA_{eq}$, where J is the total current density (including displacement current), and A_{eq} is the equivalent area of the sensor. From the ratio of the primary to secondary turns in the balun, N, the measured signal is equal to $2N/(ZA_{eq})$, where the factor of two accounts for the 50 Ω resistor. As with the field sensor, we expect that the air conductivity will be negligible relative to the load resistance. In this case, the assumption is a bit more robust as the circuit resistance between the plates is rather low compared to the field sensors.

The current sensor frequency response is determined by the load resistance, plate capacitance, and the balun. Based on Figure 9, one can infer that the system will act as a low-pass filter. In the case of the original sensor, the cutoff frequency occurs at approximately 870 MHz (the mesh sensors have a somewhat higher cutoff). Furthermore, the balun acts to block any dc signals and therefore makes the current sensor act as a band-pass filter. An estimate of the mutual inductance of the balun yields 68 nH and a resulting lower cutoff frequency of 117 MHz. By comparison, the lower cutoff frequency for the mesh sensor is estimated to be 420 kHz. However, in the absence of measured cutoff frequencies, the analyses presented here will apply a high-pass filter at 1 MHz. Ultimately, The electric field and measurements of the current density can be used to calculate the conductivity dynamics via the relation $\sigma = J/E$.

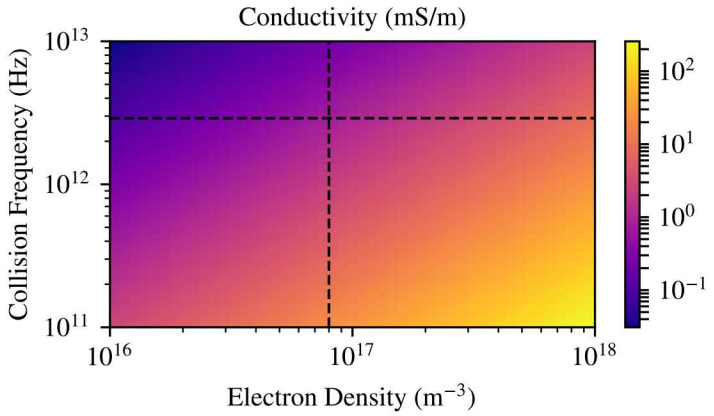

Figure 10: Estimated dc conductivity for a range of densities and collision frequencies.

Discussion

Conductivity Estimates

The conductivity of an ionized gas can be calculated based on the charge density and the neutral collision rate. At higher frequencies, this conductivity is frequency dependent, but in the DC limit, it can be expressed as [21],

$$\sigma_{dc} = \frac{n_e e^2}{m_e \nu}, \tag{2}$$

where n_e is the electorn density, e is the elementary charge, m_e is the electron mass, and ν is the electron-neutral collision frequency. The electron density in the air is time-varying, but an estimate can be made of the peak density based on the measured radiation dose. At the location of the meshand 703 sensors, dosimeters recorded an average of approximately 0.3 Gy which is roughly equivalent to 30 R. By definition, 1 R is equal to a charged particle density of 2×10^9 cm^{-3}. Therefore, the electron density is estimated to be 6×10^{10} cm^{-3}. From other sources [22], we can estimate the electron-neutral collision rate to be 2.9×10^{12} Hz, yielding an estimated conductivity of $\sigma_{dc} = 0.58$ mS/m.

To go further, Figure 10 shows the dc conductivity as a function of both the collision frequency and the electron density. Both of these values are believed to vary widely in the time soon after a shot from HERMES III. The dashed lines indicate the location of the above estimate of the conductivity. As can be seen, over the relatively small range of densities and collisionalities, we can expect the conductivity to vary by three orders of magnitude. Indeed, the range of conductivity values in the courtyard is likely even larger due to the strong variation of dose with respect to distance from the converter.

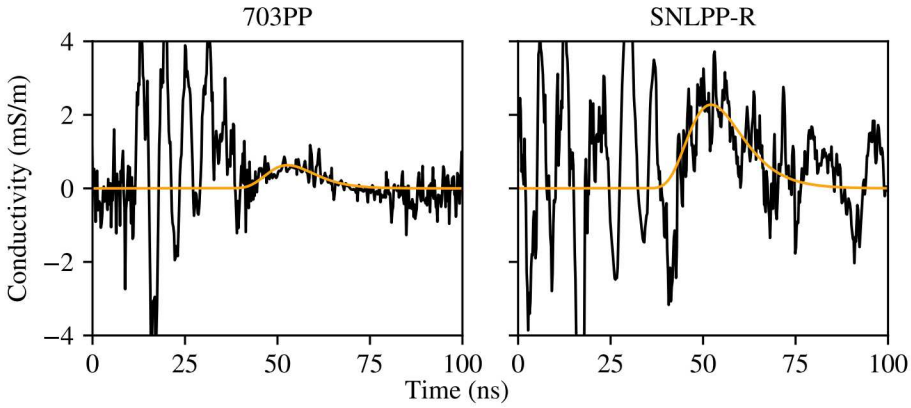

Figure 11: Average conductivity measured by the 703 and SNLPP-R sensors for all shots with the doors open.

Measured Conductivities

The conductivity dynamics for each sensor and shot are recored in appendix A. For an initial assessment of the conductivity in the courtyard, we will focus our attention on the 703 and mesh-sensors. As these sensors remained stationary throughout the majority of the shots, there are ample data to average, giving the best possible reconstruction of the conductivity dynamics after a shot. Figure 11 shows the average of the 703 and reference mesh sensor averaged over all shots with the exceptions of those where the doors were partially closed. In addition, least-squares fits for the two sensors are plotted with a log-normal curve as the model.

The conductivity measurements can be characterized by a significant degree of noise, particularly at early times. This can be inferred from Figure 6 where the magnitude of both the currents and fields are small and several zero crossings occur. By averaging many of the shots together and carefully fitting the results, as is done in Figure 11, some idea of the air conductivity can be determined. However, these results are subject to a number of qualifications.

First, the fits to the measured conductivities assume that conductivity during the radiation pulse from HERMES is effectively zero. This assumption may seem contradictory as the electron density should be at its highest during this time, and therefore so should the conductivity. However, it is important to bear in mind that conductivity is a macroscopic quantity that describes a material's ability to carry current. During the radiation pulse, the free charges are electrons with a very anisotropic distribution of energies, oriented along the beam propagation vector. At early times, the kinetic energy of these electrons is far in excess of the external electric field, meaning that the measured current at early times is not representative of the actual air conductivity.

It takes a finite time for the primary electrons, generated by the gamma rays, and the resulting secondary electrons due to neutral collisions to come to equilibrium with the external field. Per Longmire [23], this can be up to 10 ns in real time. Therefore, the fits are constrained to $t > 40$ ns, after the pulse has ended. Peak conductivities are 0.6 and 2.3 mS/m for the 703 and mesh sensors respectively. The standard deviations are approximately 6.7 ns and 7.8 ns for the two sensors,

comparable to the electron attachment rate which is 2×10^8 s^{-1} [1].

More insight on the behavior of the pie pans can be obtained through consideration of the individual signals. In Figure 6, we can see that the field sensors are subject to a large degree of common-mode noise; the signals are nearly equal. Therefore, we expect substantial uncertainty in the electric field measurements as they are dominated by noise. The exact source of this noise is unknown, but it is not representative of the actual electric fields as can be seen by comparison to D-dot measurements [24]. At present the most probable explanation is Compton current drive due to gamma ray interactions. Neglecting the high frequency noise, the shape is rather similar to that of the spherical Compton diodes [25]. The presence of a signal prior to $t = 0$ can likely be attributed to small errors.

The current signals in Figure 6 exhibit very different behavior from the field sensors. There is relatively little common mode noise in the signals, instead there is a very strong oscillatory behavior during the radiation pulse. However, these dynamics are contrary to expectations from theory and from the field measurements. Similar to the field sensors, the envelope of the oscillations is quite similar to the dose rate dynamics during a shot. This suggests that while the oscillations are not common mode, they may still be noise and not real current. It is possible that these oscillations are the natural resonance of the current sensor circuit due to the inductance of the balun.

As both the field and current sensors bear strong indications of noise during the radiation pulse, this provides further justification for limiting the conductivity fits to the post-pulse period. While the mesh sensors were designed assuming that common mode noise would not be a dominant factor, the results from the original sensors suggests otherwise. While the design choices of the mesh sensors may reduce the radiation drive and subsequently the noise, these results point toward a need for differential sensors. Therefore, the best estimate of the conductivity at this location is likely given by the 703 sensor. With its peak of 1.3 mS/m, it bears very good agreement with the dose-based estimate of the conductivity.

Partially Closed Doors

As previously mentioned, the HERMES doors were partially closed for several of the shots (10272, 10273, and 10276-10278). In each of these shots, the courtyard doors were closed down to approximately the diameter of the converter. With the doors fully open, the dose pattern of HERMES tends to be rather divergent. With the doors closed, the dose pattern is expected to be more collimated. That said, the mesh and original sensors are located very close to the axis of the beam which suggested that there should be minimal changes to their response.

Figure 12 compares the average conductivity measured with the doors partially closed to that with the doors open. Though there is substantial noise in the measurements, there appears to be an unexpected drop in the conductivity with the doors closed. This is particularly apparent when one considers the total dose delivered in the vicinity of the conductivity sensors. Figure 13 Shows the dose as measured by the thermoluminescent dosimeters (TLDs) placed on the 703 sensor stand for each shot. The shots with partially closed doors are shown in red. As can be seen, the doses

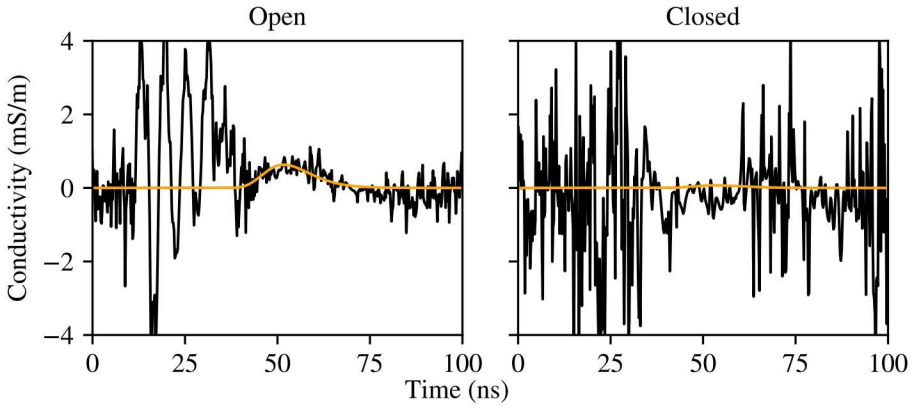

Figure 12: Comparison of the average conductivity with the courtyard doors both fully open (left) and partially closed (right).

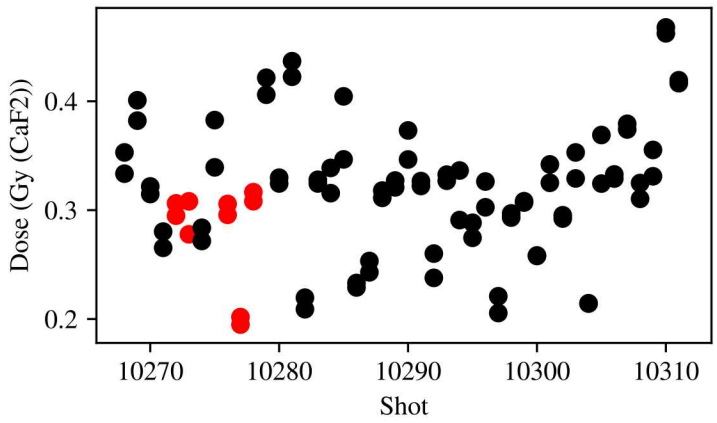

Figure 13: Dose at the 703 sensor stand for all shots. Shots with partially closed doors are in red.

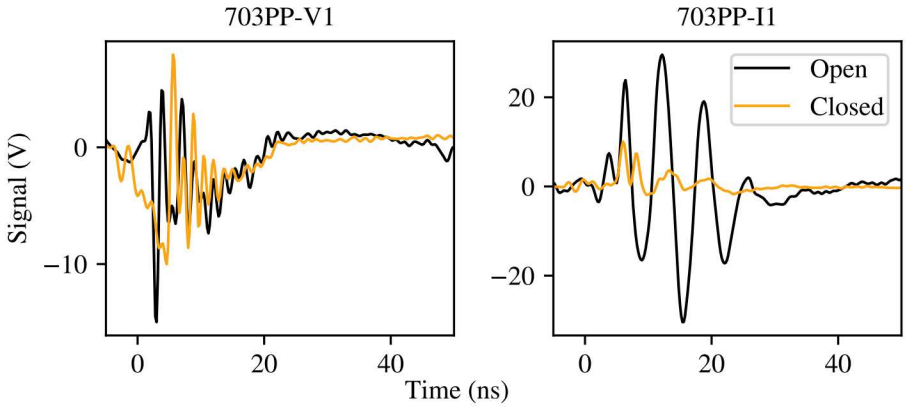

Figure 14: Comparison of channels from the 703 sensor for open (10308) and partially closed (10278) doors.

measured with the doors partially closed cluster about the average for the trials, indicating no significant reduction in dose. Under the assumption that conductivity is directly proportional to the dose, this suggests that no change in the measured conductivity should be observed.

Further insight may be gained by a comparison of the signals from the individual channels as seen in Figure 14. Both field and current sensors bear different dynamics with the doors partially closed, and this is particularly true for the current sensors. The current sensors show a strong reduction in the signal strength, despite comparable total doses for both shots. This indicates that a significant component of the current signal is not determined by the field-driven currents, but rather by some other mechanism. One possibility is that the signals are displacement currents driven either by the directional Compton current or from HERMES machine noise [26]. However, neither seems particularly likely as the measured fields near the conductivity sensors are roughly the same order of magnitude with the doors closed [24]. Alternatively, while the partially closed doors may not lead to a substantial change in dose, they may lead to a substantial change in spectrum. Recent simulations indicate the magnetic insulation of HERMES may be inadequate in the outdoor mode, leading to some x-ray emission along the length of the of the device with a cooler spectrum. As lower energy x-rays have a lower mean free path, they are more likely to interact with the conductivity sensors. Therefore, supposing that the normal mode noise observed in the current sensors is due to low energy x-ray interactions, if partially closing the doors reduces the flux of low energy x-rays while not altering the flux of high energy x-rays from the converter, then one might observe a reduction in noise without a substantial change in overall dose.

Canonical Shape Locations

As the canonical shape was moved in the courtyard, it experienced different environmental conditions including free fields and conductivities. The 702 sensor was always fielded alongside the canonical shape in order to provide an estimate of local conductivity for all cases. The sensor was positioned adjacent to the shape, halfway along its central axis and at the same height. The

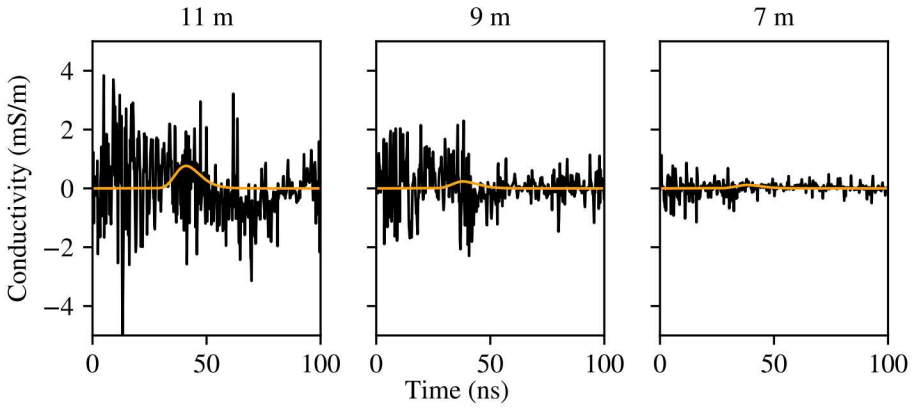

Figure 15: Conductivity at each of the canonical shape locations as measured by the 702 sensor.

canonical shape was fielded at three positions in the courtyard, roughly located at 11 m (10268-10280), 9 m (10281-10292), and 7 m (10293-10313).

The measured conductivity dynamics for each of these locations are shown in Figure 15. The results for all shots at each location (excepting the partially closed door cases) are averaged together. As before, an approximate fit to the data using a log-normal curve is provided, yielding conductivity estimates of 0.77 mS/m, 0.24 mS/m, and 0.12 mS/m at 11 m, 9 m, and 7 m respectively. Due to the noise in the signals, the least-squares fitting algorithm was unable to converge, necessitating manual fitting.

While the peak conductivity values are reasonable, the trends run contrary to expectation; the peak conductivity appears to decline as the canonical shape approach nears the converter. Again, assuming that dose is correlated with conductivity, this is opposite the expected trend. To determine the reason for these trends, we again must turn to the individual channel data for the 702 sensor.

A representative example of the 702 sensor at the 11 m position can be found in Figure 16. While the electric field sensor signals are not entirely dissimilar from those of the 703 sensor, the dominant oscillation frequency in the current sensors is quite different. Furthermore, while the results in this figure continue to show the two current sensors with opposite polarity, this changes following shot 10286. After this shot, the two signals are of the same polarity and nearly identical, causing the current signal to largely disappear. This causes the reduction in the conductivity signal seen in Figure 15.

The distinct difference between the current signals measured by the 702 and 703 sensors, both in magnitude and in frequency content, suggest a malfunction in one (or both) sensors during the trials. As will be seen below, the frequency content of the 702 sensor for shots before 10287 most closely matches that seen in the PP-16 and mesh sensors. However, the change in polarity of the 702PP-I2 channel and an accompanying change in dynamics indicates and an unrecorded alteration to the sensor during the trials.

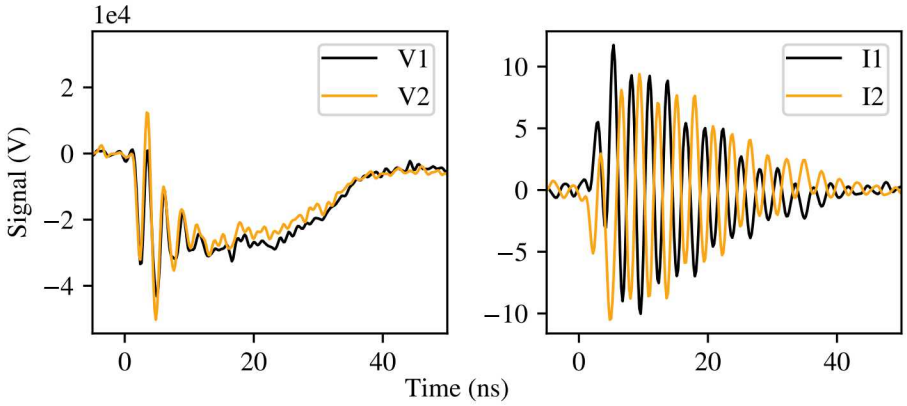

Figure 16: The signals from the individual channels of sensor 702 for shot 10280.

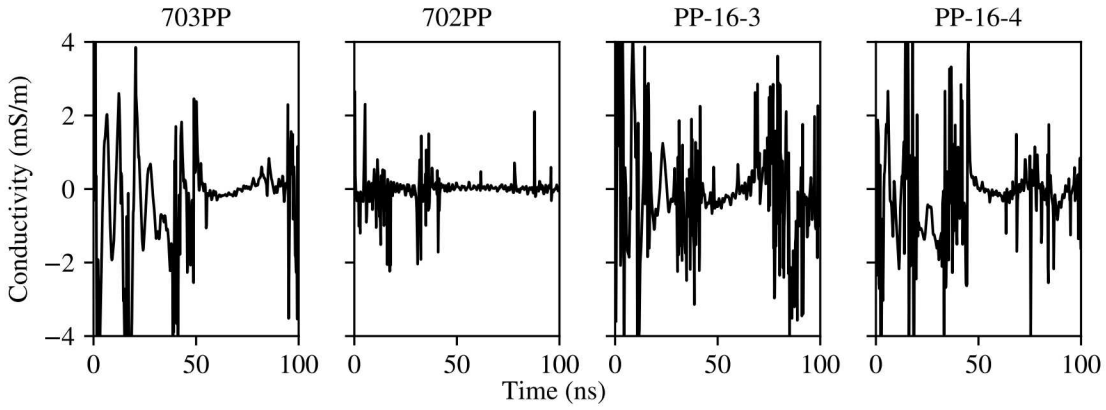

Figure 17: Comparison of the conductivity results from the 700 series sensors with the new ones fielded during 10310-10313.

New Pie Pan Sensors

The new pie pan sensors (PP-16-3 and PP-16-4) were fielded for shots 10310-10313. They were positioned a little over 5 m from the converter, at equal z to the 703 and mesh sensors. While the most natural point of comparison for the new sensors is the 703 sensors, the unusual behavior of its current sensors leads us to include the 702 results in the following comparison. Of course, as noted above, there are other concerns about the performance of the 702 sensor during the later shots. Therefore, any conclusions about the performance of the new sensors should be considered preliminary.

Figure 17 shows the average conductivity measurements for shots 10310-10313 for the four pie pan sensors. Despite the concerns about the performance of the 703 sensor, there are clear similarities with the measurements by the new sensors. In contrast, the 702 sensor signal bears less noise, but deviates substantially from the dynamics recorded by the other sensors. This reinforces the contention that something is wrong with the post-10286 results from 702.

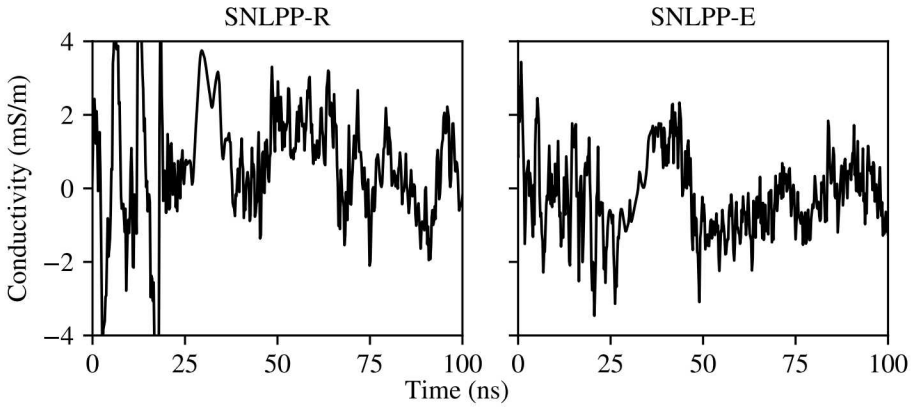

Figure 18: Comparison of the gridded (left) and plate (right) electrodes for the mesh conductivity sensors.

As with the other pie pan sensors, the PP-16 series also suffers from a significant amount of noise due to the low signals. While not shown here, the current sensors show similar frequency content to that of the 702 sensor and the two channels are of opposite polarity. This adds to the evidence that there is some issue with the performance of 703. The field sensor waveforms for the PP-16 sensors possess substantial common mode noise as with the older sensors. The dynamics are similar to the original sensors, however the signal strength on the 703 field sensor channels is noticeably higher. Despite relatively few shots, the PP-16 sensors appear to possess similar performance characteristics to the 700-series sensors.

Mesh Construction

After shot 10289, the SNLPP-E sensor had its sensing grids replaced with plates in an effort to test the effects of gamma driven current on the conductivity measurements. For thin, low-Z, structures gamma-ray interaction may not significantly impact measurements. However, these effects increase in importance for larger sensors and smaller signals.

Figure 18 compares the gridded (left) and plate (right) electrodes for shots 10290-10313. Overall, the magnitude of the measured signals are comparable, though there appears to be a low frequency offset. Noise content is comparable for the two sensors, however the gridded electrode results contain much higher oscillations during the HERMES pulse. An examination of the current and field sensor results show essentially no difference between the gridded and plate sensors. The current sensors for SNLPP-R and SNLPP-E show different dynamics for most of the shots, however this includes the shots for which both sensor sets had gridded electrodes. Therefore, at the levels under consideration, there appears to be no significant difference between the gridded and plate electrodes for the mesh sensors.

Conclusions and Recommendations

During November 2016, two weeks of trials at HERMES III were conducted in support of improved physics understanding. During the course of these trials, a number of old and new conductivity sensors were fielded. All of the sensors were essentially combinations of passive field and current probes, yielding the conductivity through the equation $\sigma = J/E$.

Background conductivity levels were estimated to be 0.6 mS/m based on an average of all open door shots from the 703 sensor. However, this estimate comes with a fair number of caveats due to the small signals in question, analysis difficulties, and noise. More specifically, our analysis ignores the times during the HERMES III shot during which the charged particles are not in equilibrium with the field. Furthermore, the differential sensors indicated a relatively small signal-to-noise for the field measurements and large normal mode noise on the current measurements. Relatively long-lived oscillations in the circuit components may dwarf the actual conductivity-driven signal.

Similar issues arose in attempts to analyze the air conductivity with partially closed doors. The conductivity, as measured by the 703 sensor, dropped to essentially negligible levels despite near-average radiation dose. There is some possibility that the reduced signal may be attributed to changes in the gamma spectrum associated with the partially closed doors, but more likely are noise issues as mentioned above. As the partially closed doors resulted in significant changes to the current sensor behavior while the fields (as measured by D-dots) were largely unchanged, these differences are likely related to radiation effects.

An attempt was made to analyze the change in conductivity in space as the 702 sensor was moved along with the canonical shape. Initial analysis showed a *decreasing* conductivity as the test article approached the converter. This runs contrary to expectation, and further investigation showed an unexpected change in the 702PP_I2 sensor polarity following shot 10286. Results after this shot show relatively little measured field or current, making any determination of the conductivity at the canonical shape difficult.

Lastly, an effort was made to assess the gamma-driven current contribution to the conductivity sensor measurements by comparing the performance of the SNL sensor with gridded electrodes to the performance with plate electrodes. While modest differences were observed in the average conductivity dynamics, a closer inspection of the channel signals showed no difference in the field sensor response. Meanwhile, there were notable differences in the SNLPP-R and SNLPP-E current sensor behaviors throughout the trials.

On the basis of these results, several recommendations can be made for the improvement of the conductivity sensor performance. The most basic of these recommendations is careful pre-trial testing of the sensors to ensure consistent response to external stimuli. During the trials, the signals from four of five sensors had indications of inconsistent behavior. To extend the measurements to multiple locations with confidence, the sensors must behave identically.

Furthermore, the response of both the field and current sensors must be improved. This can be accomplished by increasing both the diameter and distance of the sensing plates. Additional

changes to the sensing circuitry, such as the use of higher bandwidth transformers and better characterized resistors, may also improve the sensor response.

Finally, other approaches to measuring the conductivity should be explored. There are several alternatives which may provide more robust measurements of the conductivity in this challenging environment. One example would be the use of a combined D-dot and I-dot system, in a manner similar to the pie pan field and current sensing components. Another approach would be the use of an active sensor where a biased plate is contained within a Faraday cage; eliminating the need to measure the field. A third example is the use of microwave techniques involving carefully designed transmission lines, coaxial geometries, or waveguides. By fielding one (or many) of these sensors in smaller scale experiments, we can establish confidence in conductivity measurements prior to engaging in large scale trials, such as those at HERMES.

References

[1] C. L. Longmire and J. L. Gilbert, "Theory of EMP Coupling in the Source Region," Defense Nuclear Agency, Washington, D.C., Tech. Rep., 1980.

[2] C. E. Baum, E. L. Breen, J. C. Giles, J. O'Neill, and G. D. Sower, "Sensors for Electromagnetic Pulse Measurements Both Inside and Away from Nuclear Source Regions," *IEEE Trans. on Antennas and Prop.*, vol. 26, no. 1, pp. 22–35, 1978.

[3] C. E. Baum, "Radiation and Conductivity Constraints on the Design of a Dipole Electric Field Sensor," 1965.

[4] W. B. Boyer, "Computer compensation for cable signal degradations," Sandia National Laboratories, Tech. Rep. SAND87-3072, December 1987.

[5] C. T. R. Wilson, "On Some Determinations of the Sign and Magnitude of Electric Discharges in Lightning Flashes," *Proceedings of the Royal Society A: Mathematical, Physical and Engineering Sciences*, vol. 92, no. 644, pp. 555–574, sep 1916.

[6] R. E. Partridge, "Capacitive Probe E-Field Sensors," 1964.

[7] C. E. Baum, "Parameters for Some Electrically-Small Electromagnetic Sensors," 1967.

[8] ——, "The Circular Parallel-Plate Dipole," 1969.

[9] ——, "Some Further Considerations for the Circular Parallel-Plate Dipole," 1969.

[10] L. Marin, "Scattering by Two Perfectly Conducting, Circular, Coaxial Disks," 1971.

[11] C. E. Baum, E. L. Breen, F. L. Pitts, G. D. Sower, and M. E. Thomas, "The Measurement of Lightning Environmental Parameters Related to Interaction with Electronic Systems," *IEEE Trans. on Electromag. Compat.*, vol. EMC-24, no. 2, 1982.

[12] F. B. Brumley, D. C. Evans, and D. L. Mangan, "IEMP Studies of a Dielectric-Filled Cavity: A Comparison of Experiment and Theory," *IEEE Trans. on Nucl. Sci.*, vol. 20, no. 6, pp. 48–57, 1973.

[13] R. K. Baum, J. E. Lenz, D. W. Clifford, W. G. Butters, J. E. Nanevicz, E. F. Vance, R. M. Cosel, M. Figueroa, A. Plumer, J, A. W. Hanson, and B. J. C. Burrows, "Lightning Technology," in *Proceedings of the 1980 Symposium on Lightning Technology*, F. L. Pitts, Ed., 1980.

[14] P. L. Rustan, B. P. Kuhlman, A. Serrano, J. Reazer, and M. Risley, "Airborne Lightning Characterization," Air Force Wright Aeronautical Laboratories, Dayton, OH, Tech. Rep., 1983.

[15] R. J. Jost, "Effects of the Measurement Configuration on the Simulation of Lightning-Aircraft Interaction," Ph.D. dissertation, University of Missouri-Columbia, 1988.

[16] P. C. Gailey, "Modeling and Measurement of Electromagnetic Fields Near Loran-C and Omega Stations," United States Coast Guard, Oak Ridge, TN, Tech. Rep., 1987.

[17] V. Hutson and F. Ursell, "The circular plate condenser at small separations," *Math. Proc. Cambridge Philos. Soc.*, vol. 59, no. 01, p. 211, jan 1963.

[18] G. F. Knoll, *Radiation Detection and Measurement*, 3rd ed. Hoboken, NJ: John Wiley & Sons, Inc., 1999.

[19] M. Bushell, R. Manriquez, G. Merkel, W. Scharf, and D. Spohn, "Source-Region EMP Simulator - A Parallel Plate Transmission Line in the Aurora Test Cell," *IEEE Trans. Nucl. Sci.*, vol. 27, no. 6, pp. 1834–1838, 1980.

[20] M. Bushell, C. Kenyon, M. Litz, G. Merkel, and H. Roberts, "Macroscopic Conductivity Measurements of Ionized Air," *IEEE Trans. Nucl. Sci.*, vol. 32, no. 6, pp. 4301–4307, 1985.

[21] M. A. Lieberman and A. J. Lichtenberg, *Principles of plasma discharges and materials processing*. John Wiley & Sons, 2005.

[22] Y. P. Raizer and J. E. Allen, *Gas discharge physics*. Springer Berlin, 1997, vol. 2.

[23] C. L. Longmire, "On the electromagnetic pulse produced by nuclear explosions," *IEEE Trans. on Electromag. Compat.*, no. 1, pp. 3–13, 1978.

[24] B. T. Yee, K. L. Cartwright, and T. D. Pointon, "November 2016 WESC trials: Free space fields and current coupling," Sandia National Laboratories, Tech. Rep. SAND2017-XXXX, October 2017.

[25] B. T. Yee, K. L. Cartwright, T. D. Pointon, G. Wright, and M. Moutrie, "November 2016 WESC trials: Spherical compton diodes," Sandia National Laboratories, Tech. Rep. SAND2017-XXXX, October 2017.

[26] B. A. Lewis, N. R. Joseph, and J. D. Salazar, "Correlation of noise signature to pulsed power events at the HERMES III accelerator," Sandia National Laboratories, Tech. Rep. SAND2016-12104, November 2016.

[27] R. D. Evans, *The Atomic Nucleus*, 1st ed. New York, NY: McGraw-Hill, 1955.

[28] C. E. Baum, "A Compton Diode for Measuring Both the Gamma Flux and One Component of the Gamma Current," 1965.

[29] S. Seltzer, "XCOM: Photon Cross Sections Database," 2010.

[30] T. W. L. Sanford, J. A. Halbleib, J. W. Poukey, D. E. Beutler, G. A. Carlson, G. T. Baldwin, T. Sheridan, R. Mock, R. S. Klingler, and D. P. Knott, "Radiation field from an extended planar-anode diode on HERMES III," *IEEE Trans. Nucl. Sci.*, vol. 36, no. 6 pt 1, pp. 1931–1936, 1989.

[31] E. R. Keiter, T. Mei, T. V. Russo, R. L. Schiek, P. E. Sholander, H. K. Thornquist, J. C. Verley, and D. G. Baur, "Xyce Parallel Electronic Simulator Users ' Guide , Version 6.4," 2015.

A Conductivities

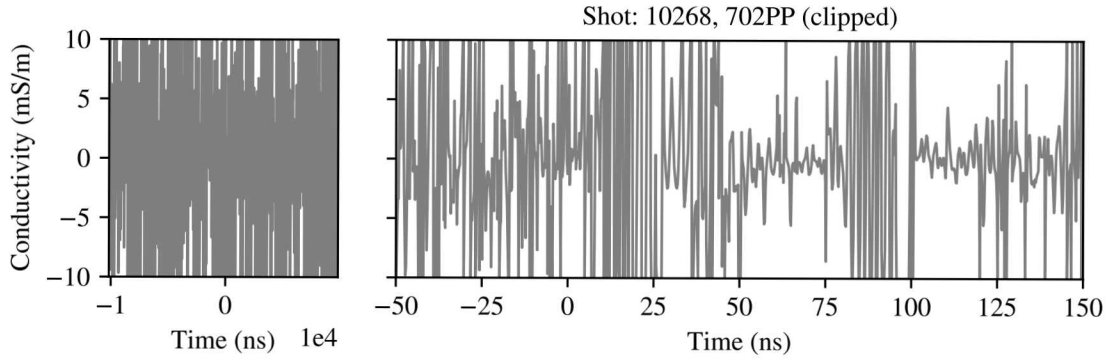
Shot: 10268, 702PP (clipped)
Conductivity (mS/m)
10
5
0
−5
−10
−1
0
Time (ns)
1e4
−50
−25
0
25
50
75
100
125
150
Time (ns)

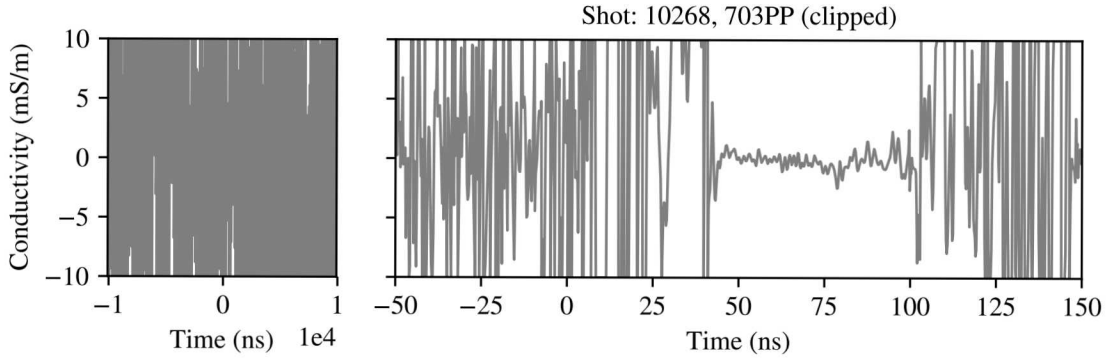
Shot: 10268, 703PP (clipped)
Conductivity (mS/m)
10
5
0
−5
−10
−1
0
1
Time (ns)
1e4
−50
−25
0
25
50
75
100
125
150
Time (ns)

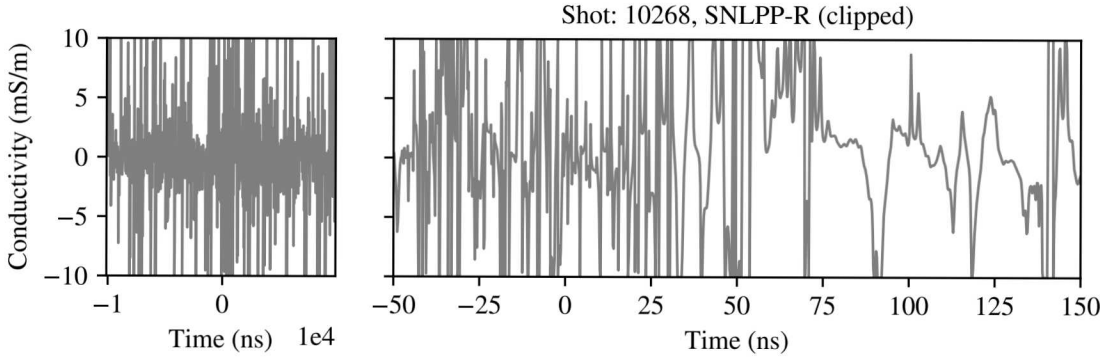
Shot: 10268, SNLPP-R (clipped)
Conductivity (mS/m)
10
5
0
−5
−10
−1
0
Time (ns)
1e4
−50
−25
0
25
50
75
100
125
150
Time (ns)

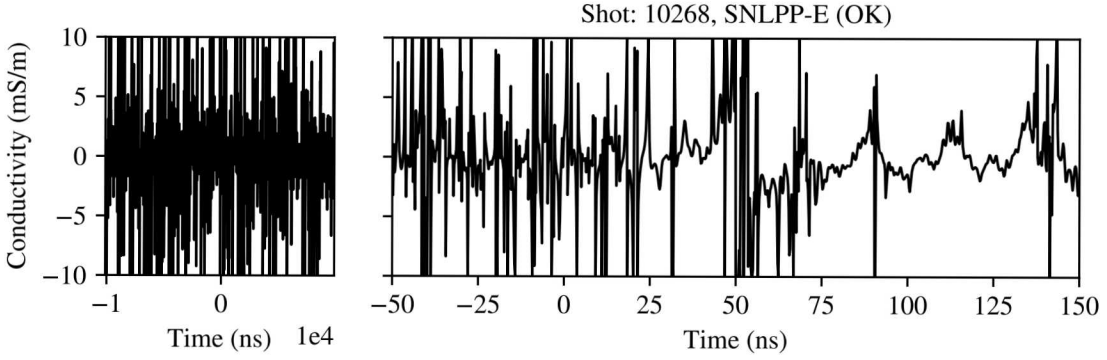
Shot: 10268, SNLPP-E (OK)
Conductivity (mS/m)
10
5
0
−5
−10
−1
0
Time (ns)
1e4
−50
−25
0
25
50
75
100
125
150
Time (ns)

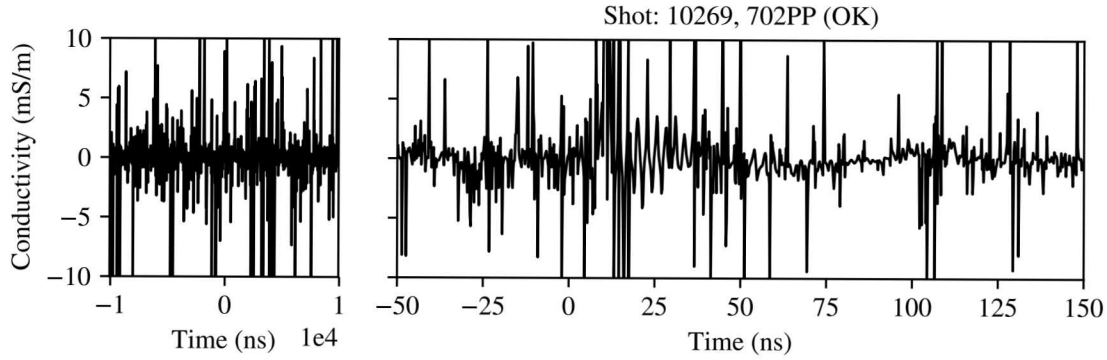
Shot: 10269, 702PP (OK)
Conductivity (mS/m)
10
5
0
−5
−10
−1
0
1
Time (ns)
1e4
−50
−25
0
25
50
75
100
125
150
Time (ns)

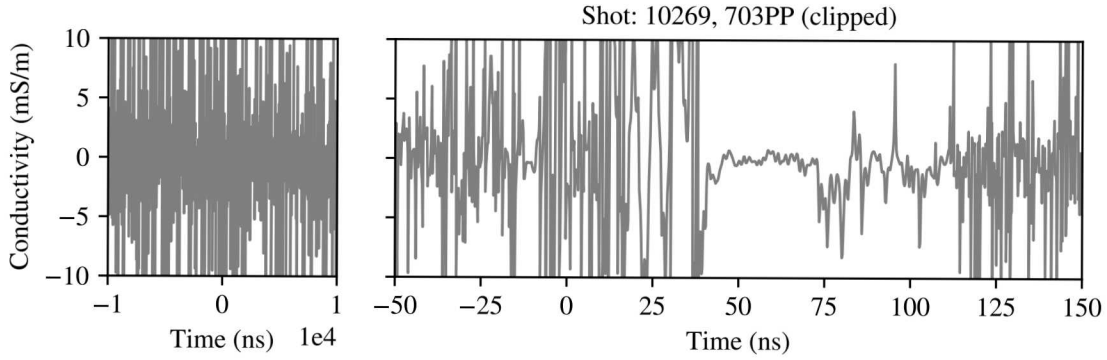
Shot: 10269, 703PP (clipped)
Conductivity (mS/m)
10
5
0
−5
−10
−1
0
1
Time (ns)
1e4
−50
−25
0
25
50
75
100
125
150
Time (ns)

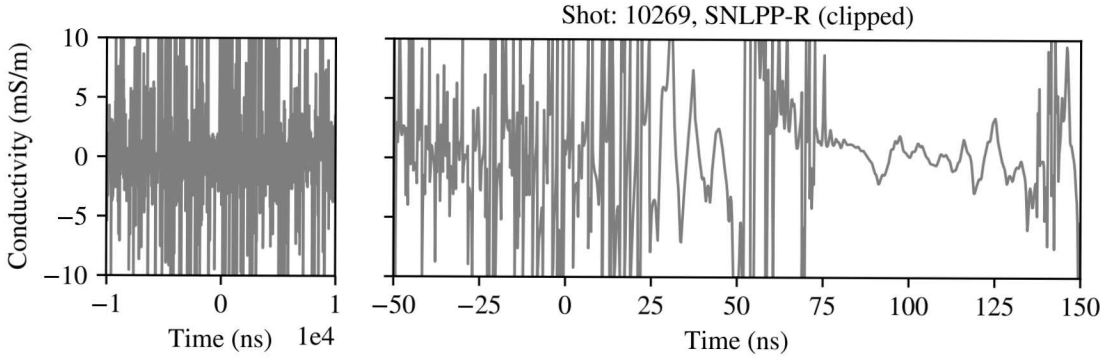
Shot: 10269, SNLPP-R (clipped)
Conductivity (mS/m)
10
5
0
−5
−10
−1
0
1
Time (ns)
1e4
−50
−25
0
25
50
75
100
125
150
Time (ns)

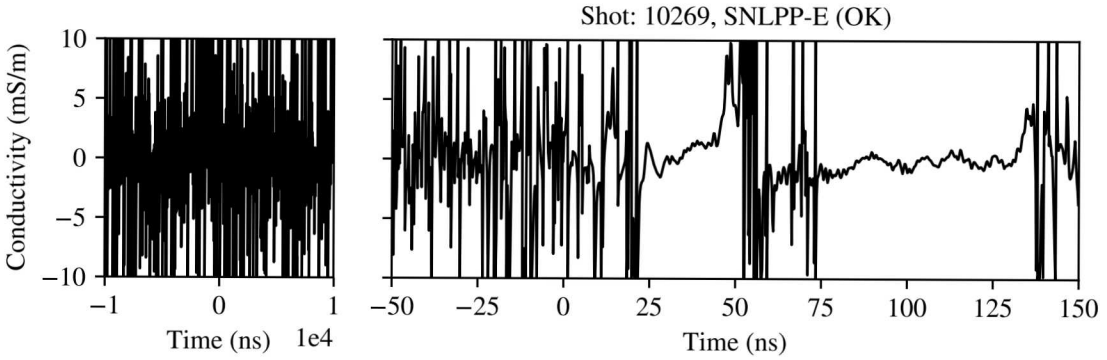
Shot: 10269, SNLPP-E (OK)
Conductivity (mS/m)
10
5
0
−5
−10
−1
0
1
Time (ns)
1e4
−50
−25
0
25
50
75
100
125
150
Time (ns)

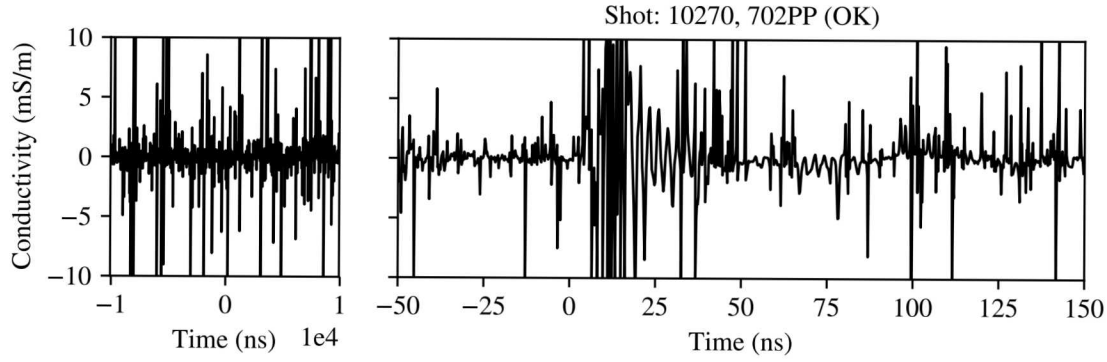
Shot: 10270, 702PP (OK)
Conductivity (mS/m)
10
5
0
−5
−10
−1
0
1
Time (ns)
1e4
−50
−25
0
25
50
75
100
125
150
Time (ns)

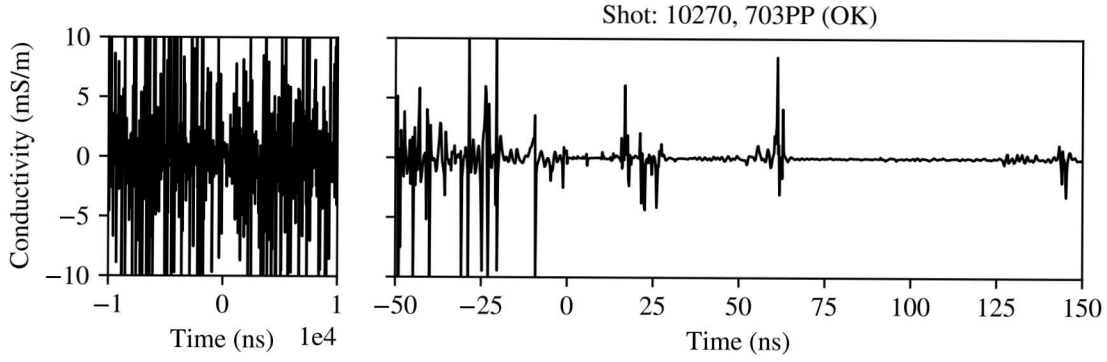
Shot: 10270, 703PP (OK)
Conductivity (mS/m)
10
5
0
−5
−10
−1
0
1
Time (ns)
1e4
−50
−25
0
25
50
75
100
125
150
Time (ns)

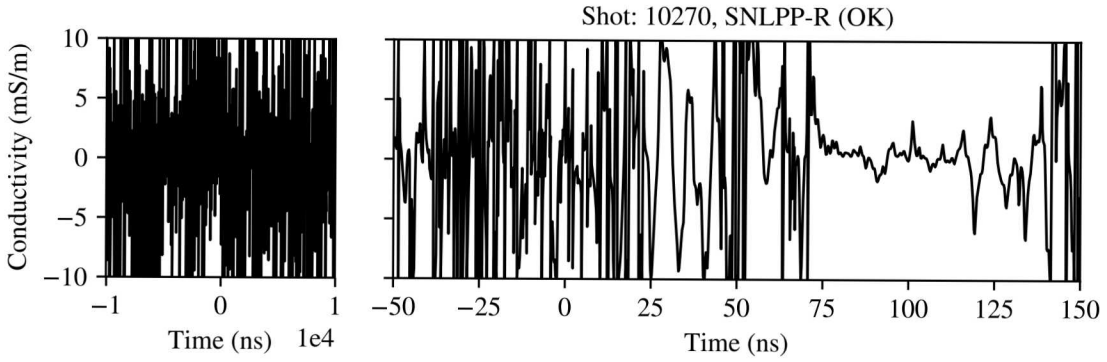
Shot: 10270, SNLPP-R (OK)
Conductivity (mS/m)
10
5
0
−5
−10
−1
0
1
Time (ns)
1e4
−50
−25
0
25
50
75
100
125
150
Time (ns)

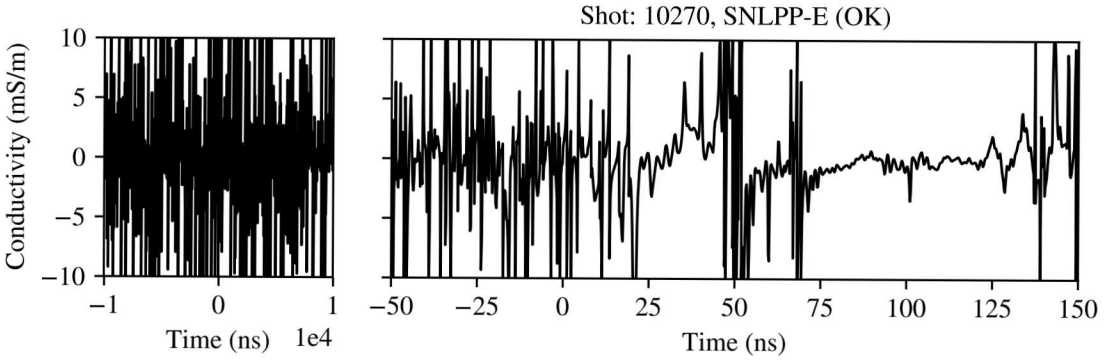
Shot: 10270, SNLPP-E (OK)
Conductivity (mS/m)
10
5
0
−5
−10
−1
0
1
Time (ns)
1e4
−50
−25
0
25
50
75
100
125
150
Time (ns)

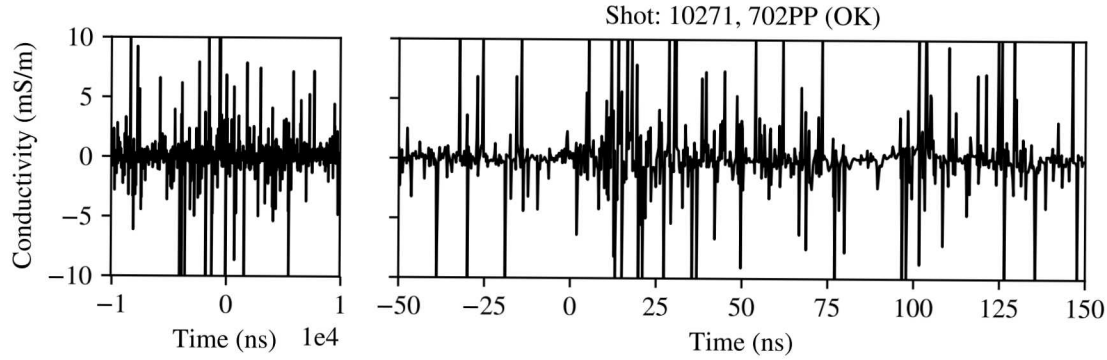
Shot: 10271, 702PP (OK)
Conductivity (mS/m)
10
5
0
−5
−10
−1
0
1
Time (ns)
1e4
−50
−25
0
25
50
75
100
125
150
Time (ns)

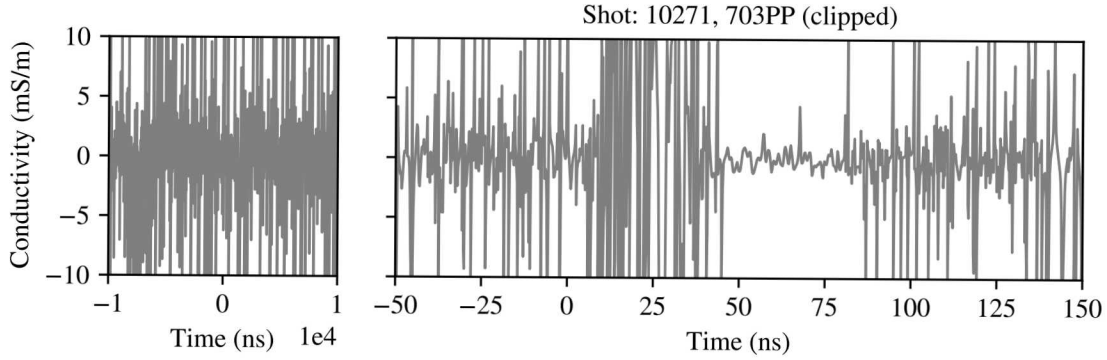
Shot: 10271, 703PP (clipped)
Conductivity (mS/m)
10
5
0
−5
−10
−1
0
1
Time (ns)
1e4
−50
−25
0
25
50
75
100
125
150
Time (ns)

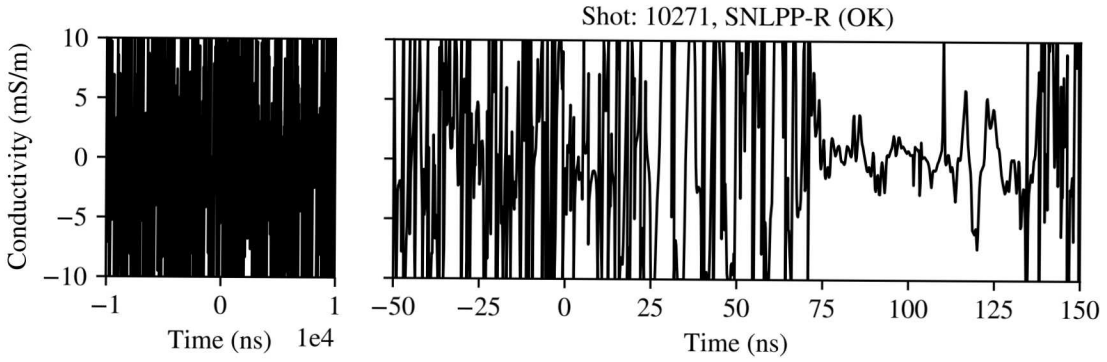
Shot: 10271, SNLPP-R (OK)
Conductivity (mS/m)
10
5
0
−5
−10
−1
0
1
Time (ns)
1e4
−50
−25
0
25
50
75
100
125
150
Time (ns)

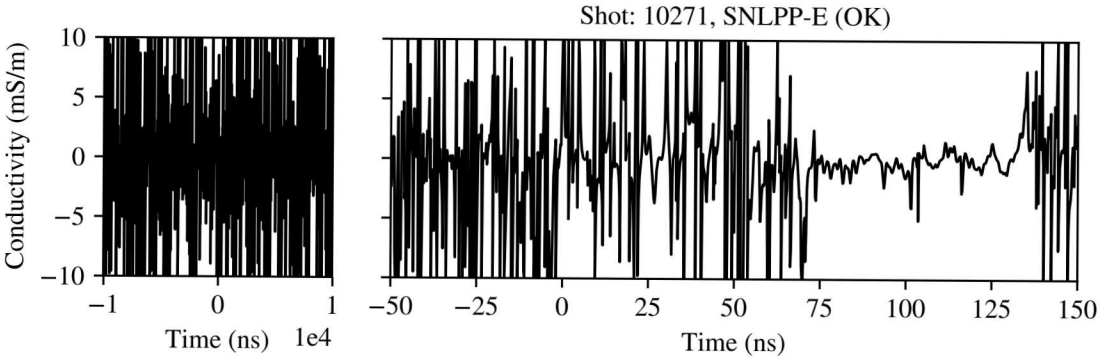
Shot: 10271, SNLPP-E (OK)
Conductivity (mS/m)
10
5
0
−5
−10
−1
0
1
Time (ns)
1e4
−50
−25
0
25
50
75
100
125
150
Time (ns)

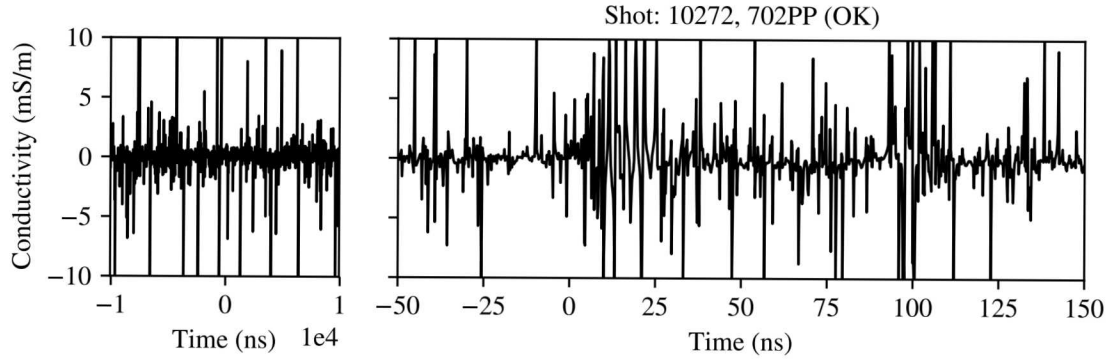
Shot: 10272, 702PP (OK)
Conductivity (mS/m)
10
5
0
−5
−10
−1
0
1
Time (ns)
1e4
−50
−25
0
25
50
75
100
125
150
Time (ns)

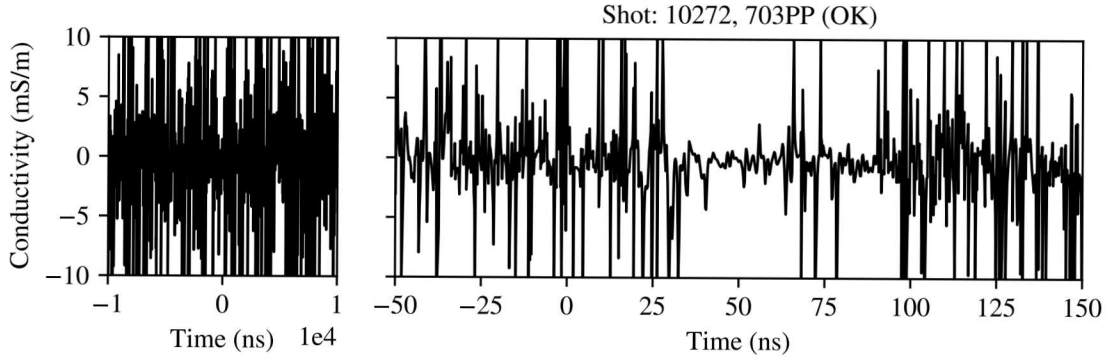
Shot: 10272, 703PP (OK)
Conductivity (mS/m)
10
5
0
−5
−10
−1
0
1
Time (ns)
1e4
−50
−25
0
25
50
75
100
125
150
Time (ns)

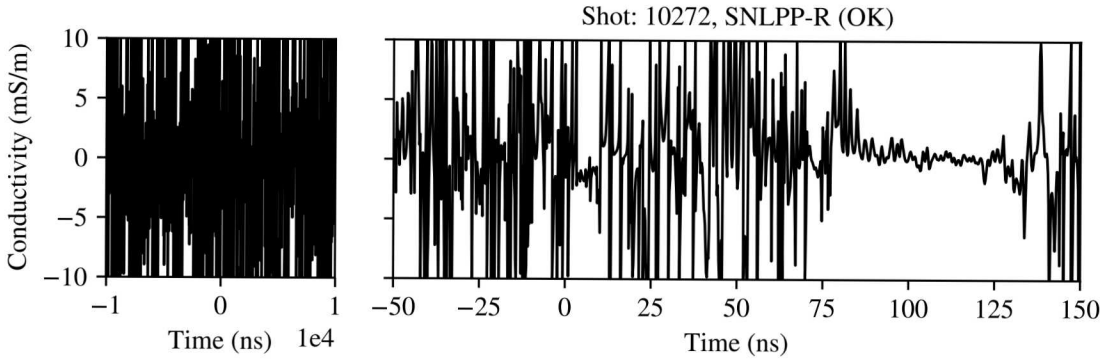
Shot: 10272, SNLPP-R (OK)
Conductivity (mS/m)
10
5
0
−5
−10
−1
0
1
Time (ns)
1e4
−50
−25
0
25
50
75
100
125
150
Time (ns)

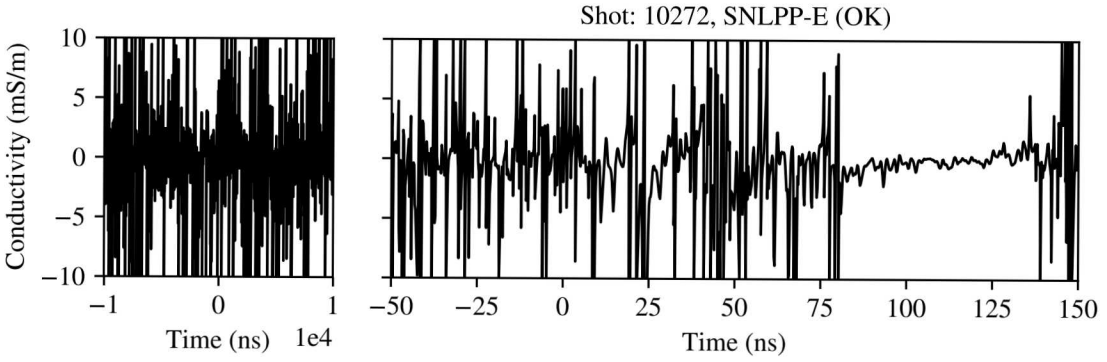
Shot: 10272, SNLPP-E (OK)
Conductivity (mS/m)
10
5
0
−5
−10
−1
0
1
Time (ns)
1e4
−50
−25
0
25
50
75
100
125
150
Time (ns)

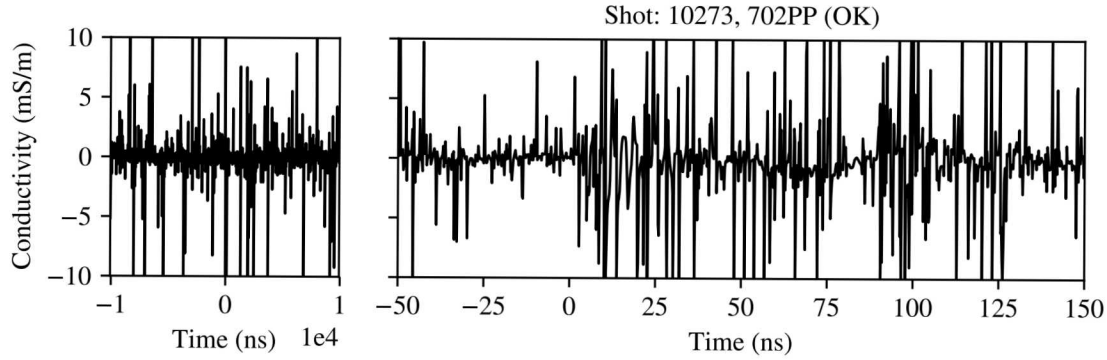
Shot: 10273, 702PP (OK)
Conductivity (mS/m)
10
5
0
−5
−10
−1
0
1
Time (ns)
1e4
−50
−25
0
25
50
75
100
125
150
Time (ns)

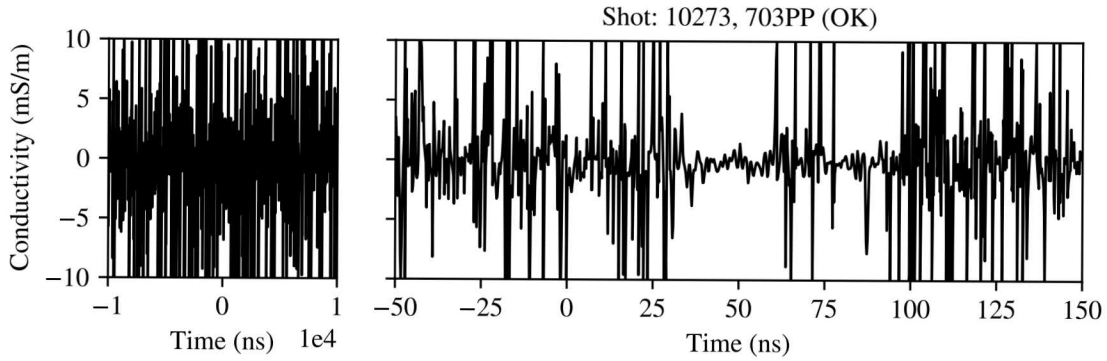
Shot: 10273, 703PP (OK)
Conductivity (mS/m)
10
5
0
−5
−10
−1
0
1
Time (ns)
1e4
−50
−25
0
25
50
75
100
125
150
Time (ns)

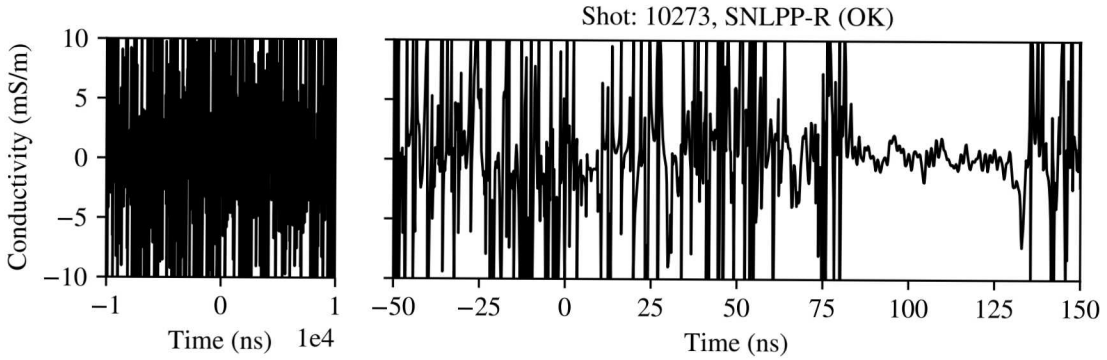
Shot: 10273, SNLPP-R (OK)
Conductivity (mS/m)
10
5
0
−5
−10
−1
0
1
Time (ns)
1e4
−50
−25
0
25
50
75
100
125
150
Time (ns)

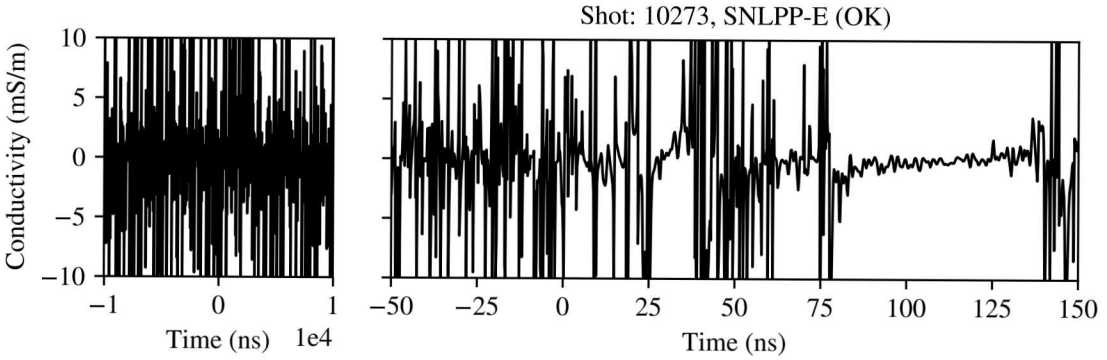
Shot: 10273, SNLPP-E (OK)
Conductivity (mS/m)
10
5
0
−5
−10
−1
0
1
Time (ns)
1e4
−50
−25
0
25
50
75
100
125
150
Time (ns)

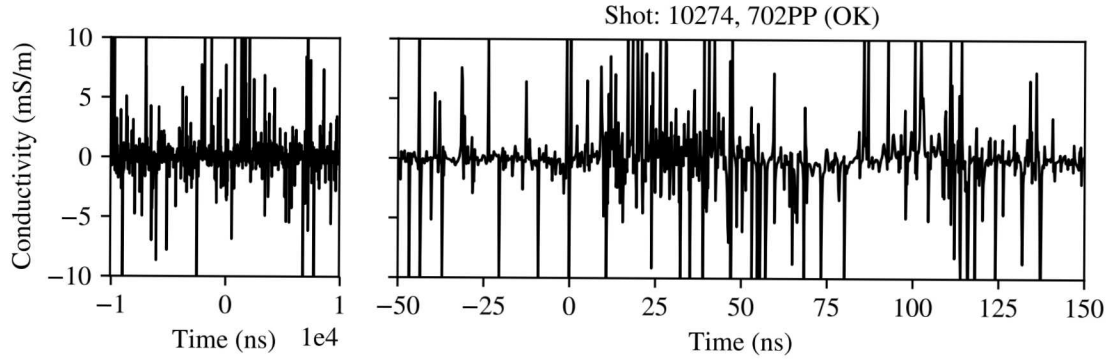
Shot: 10274, 702PP (OK)
Conductivity (mS/m)
10
5
0
−5
−10
−1
0
1
Time (ns)
1e4
−50
−25
0
25
50
75
100
125
150
Time (ns)

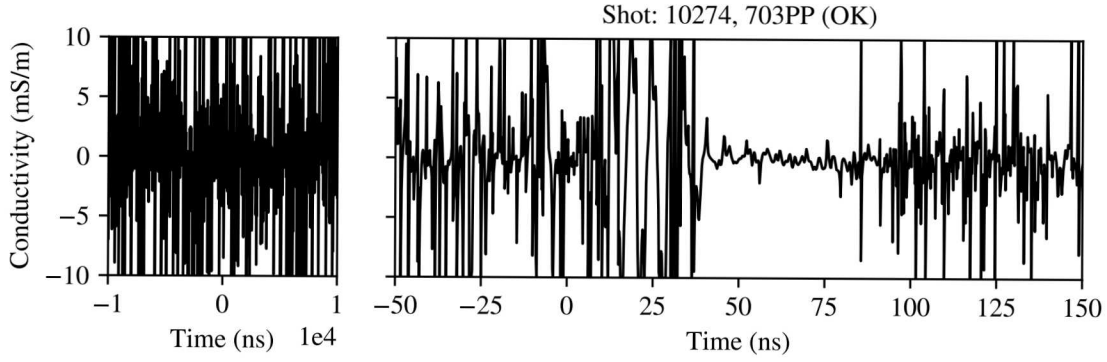
Shot: 10274, 703PP (OK)
Conductivity (mS/m)
10
5
0
−5
−10
−1
0
1
Time (ns)
1e4
−50
−25
0
25
50
75
100
125
150
Time (ns)

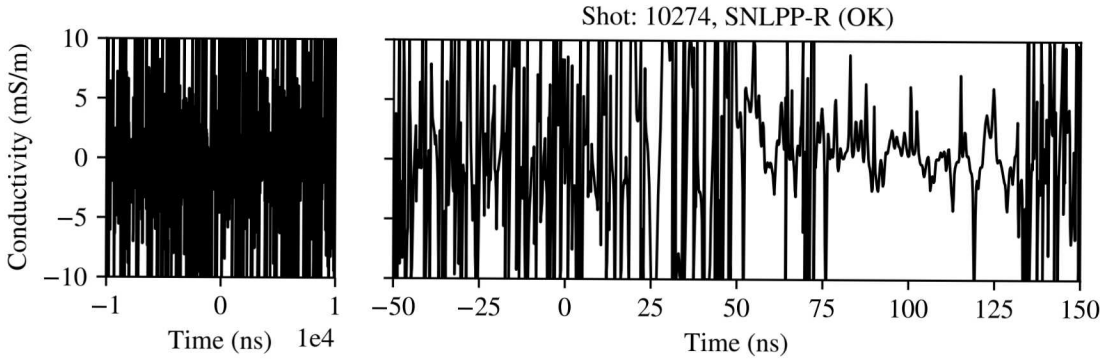
Shot: 10274, SNLPP-R (OK)
Conductivity (mS/m)
10
5
0
−5
−10
−1
0
1
Time (ns)
1e4
−50
−25
0
25
50
75
100
125
150
Time (ns)

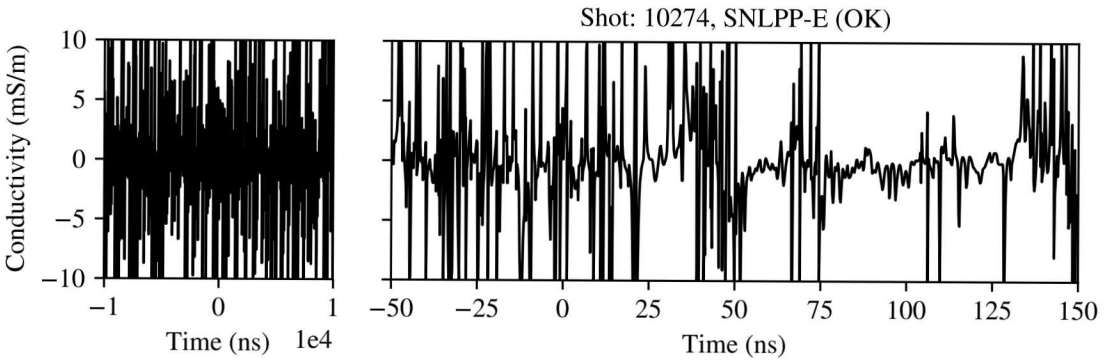
Shot: 10274, SNLPP-E (OK)
Conductivity (mS/m)
10
5
0
−5
−10
−1
0
1
Time (ns)
1e4
−50
−25
0
25
50
75
100
125
150
Time (ns)

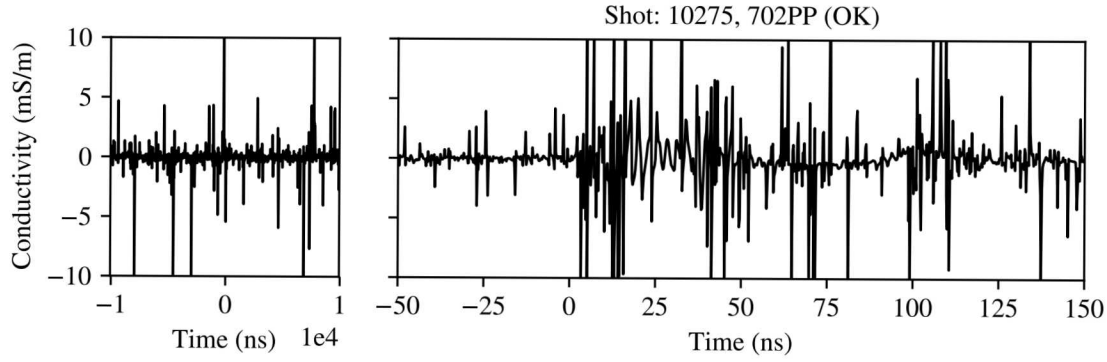
Shot: 10275, 702PP (OK)
Conductivity (mS/m)
10
5
0
−5
−10
−1
0
1
Time (ns)
1e4
−50
−25
0
25
50
75
100
125
150
Time (ns)

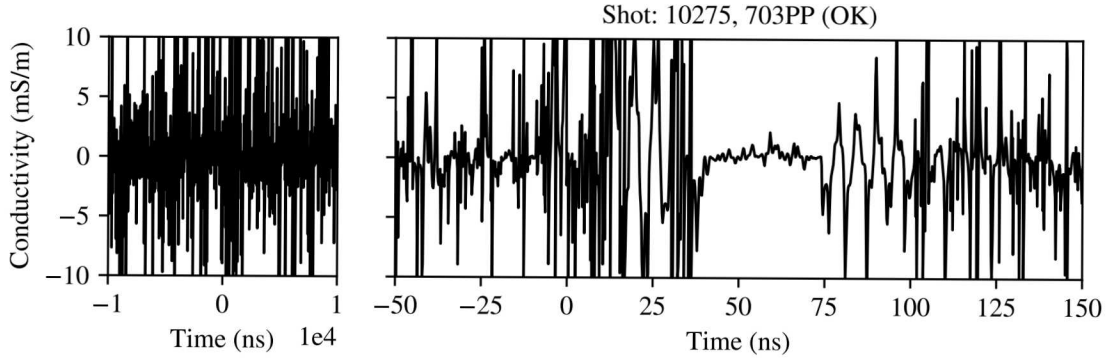
Shot: 10275, 703PP (OK)
Conductivity (mS/m)
10
5
0
−5
−10
−1
0
1
Time (ns)
1e4
−50
−25
0
25
50
75
100
125
150
Time (ns)

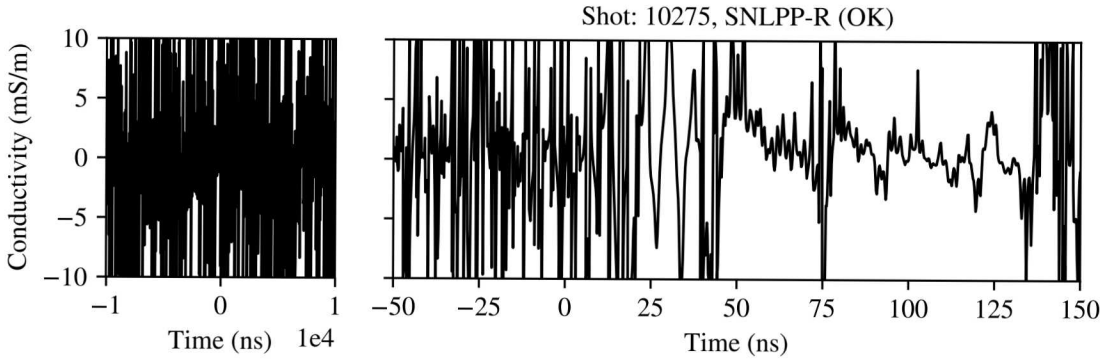
Shot: 10275, SNLPP-R (OK)
Conductivity (mS/m)
10
5
0
−5
−10
−1
0
1
Time (ns)
1e4
−50
−25
0
25
50
75
100
125
150
Time (ns)

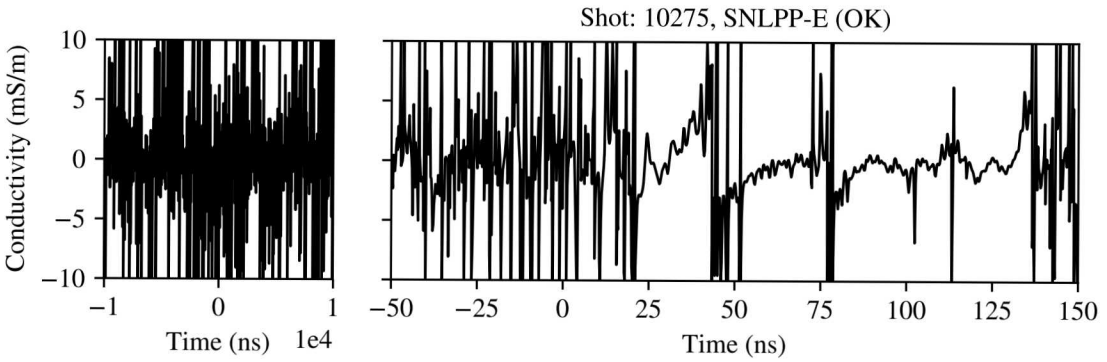
Shot: 10275, SNLPP-E (OK)
Conductivity (mS/m)
10
5
0
−5
−10
−1
0
1
Time (ns)
1e4
−50
−25
0
25
50
75
100
125
150
Time (ns)

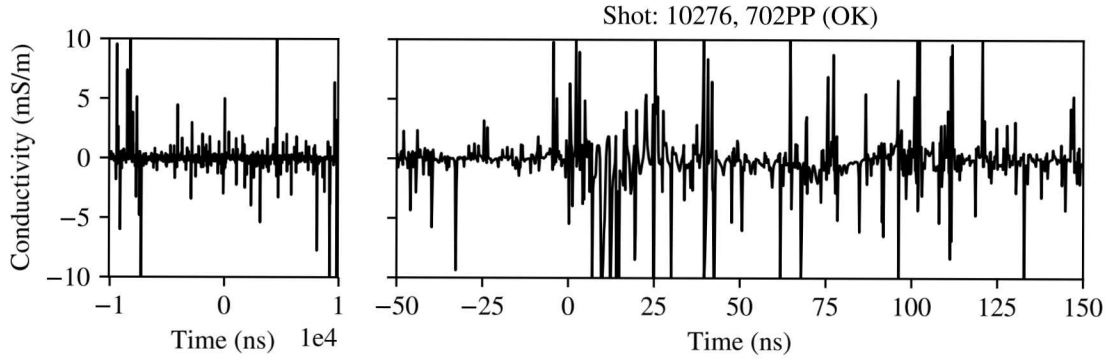
Shot: 10276, 702PP (OK)
Conductivity (mS/m)
10
5
0
−5
−10
−1
0
1
Time (ns)
1e4
−50
−25
0
25
50
75
100
125
150
Time (ns)

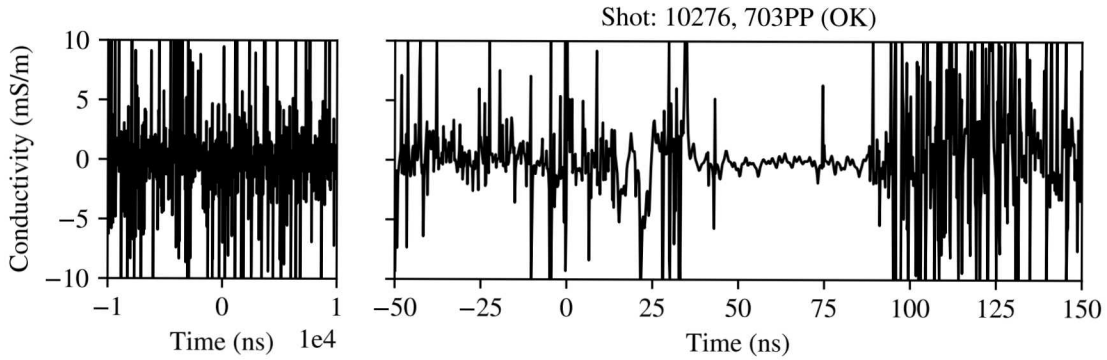
Shot: 10276, 703PP (OK)
Conductivity (mS/m)
10
5
0
−5
−10
−1
0
1
Time (ns)
1e4
−50
−25
0
25
50
75
100
125
150
Time (ns)

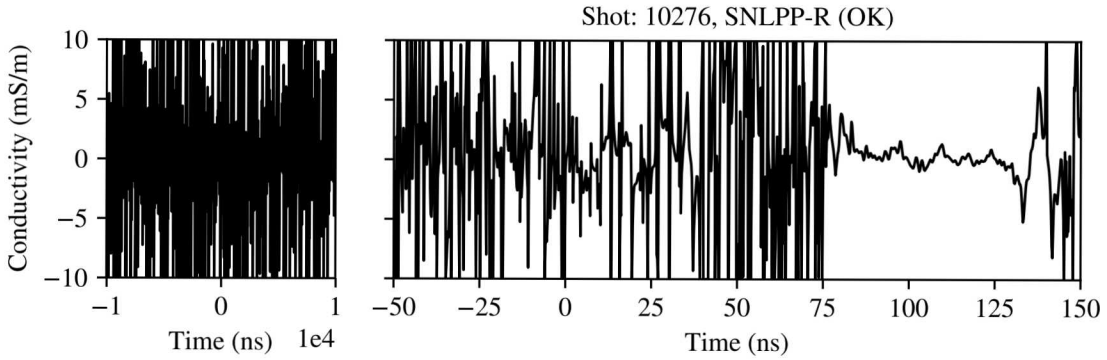
Shot: 10276, SNLPP-R (OK)
Conductivity (mS/m)
10
5
0
−5
−10
−1
0
1
Time (ns)
1e4
−50
−25
0
25
50
75
100
125
150
Time (ns)

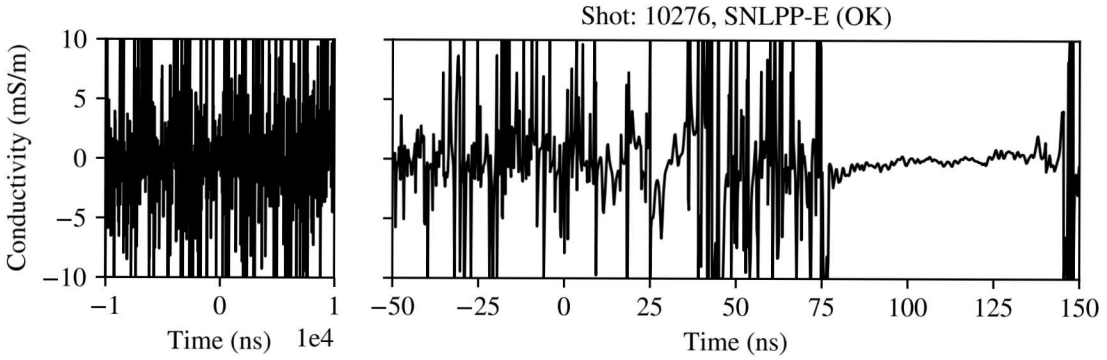
Shot: 10276, SNLPP-E (OK)
Conductivity (mS/m)
10
5
0
−5
−10
−1
0
1
Time (ns)
1e4
−50
−25
0
25
50
75
100
125
150
Time (ns)

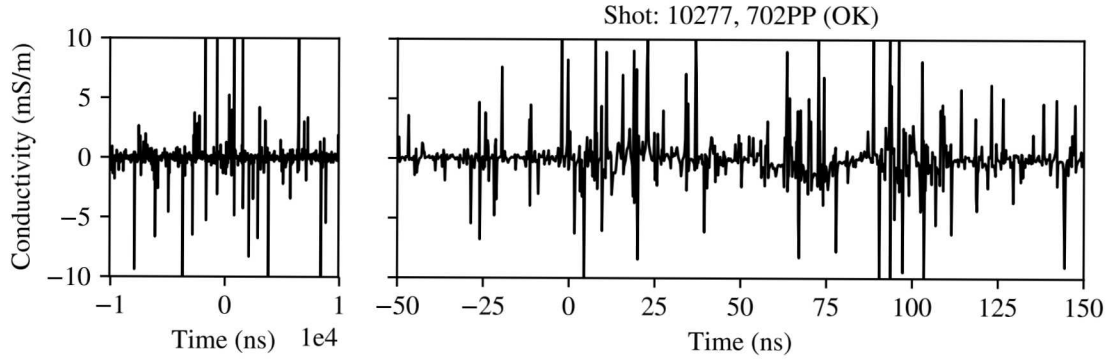
Shot: 10277, 702PP (OK)
Conductivity (mS/m)
10
5
0
−5
−10
−1
0
1
Time (ns)
1e4
−50
−25
0
25
50
75
100
125
150
Time (ns)

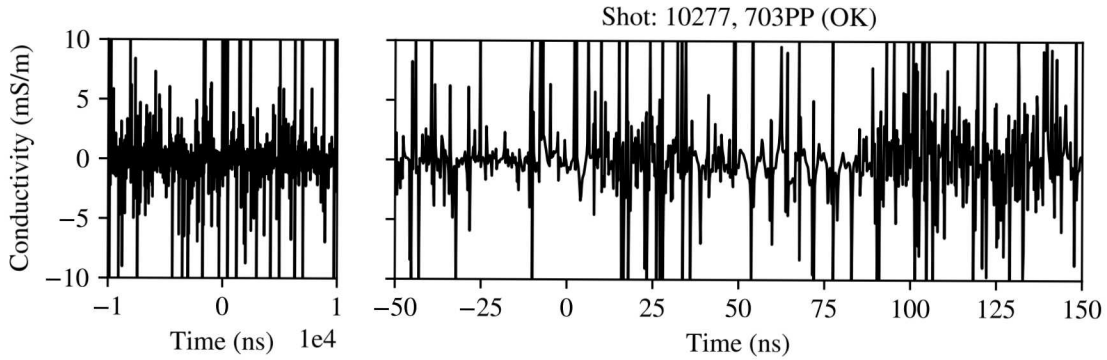
Shot: 10277, 703PP (OK)
Conductivity (mS/m)
10
5
0
−5
−10
−1
0
1
Time (ns)
1e4
−50
−25
0
25
50
75
100
125
150
Time (ns)

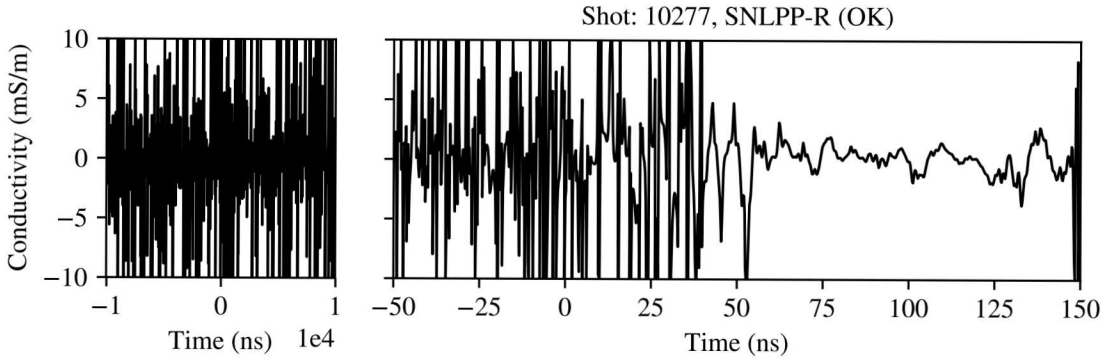
Shot: 10277, SNLPP-R (OK)
Conductivity (mS/m)
10
5
0
−5
−10
−1
0
1
Time (ns)
1e4
−50
−25
0
25
50
75
100
125
150
Time (ns)

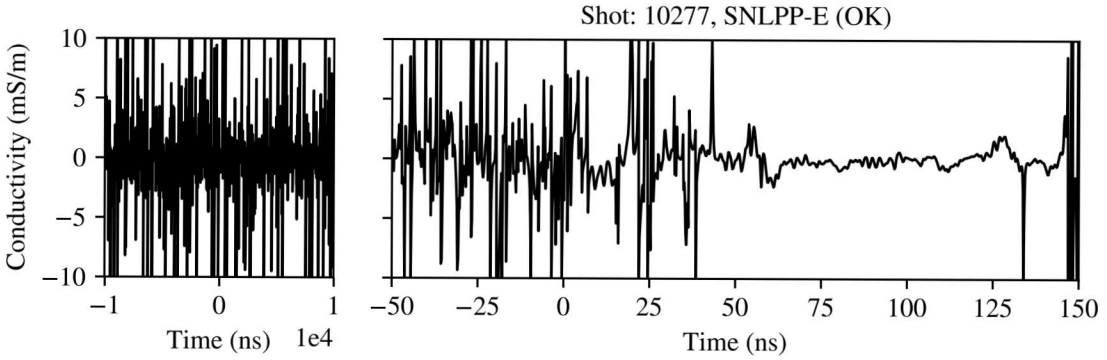
Shot: 10277, SNLPP-E (OK)
Conductivity (mS/m)
10
5
0
−5
−10
−1
0
1
Time (ns)
1e4
−50
−25
0
25
50
75
100
125
150
Time (ns)

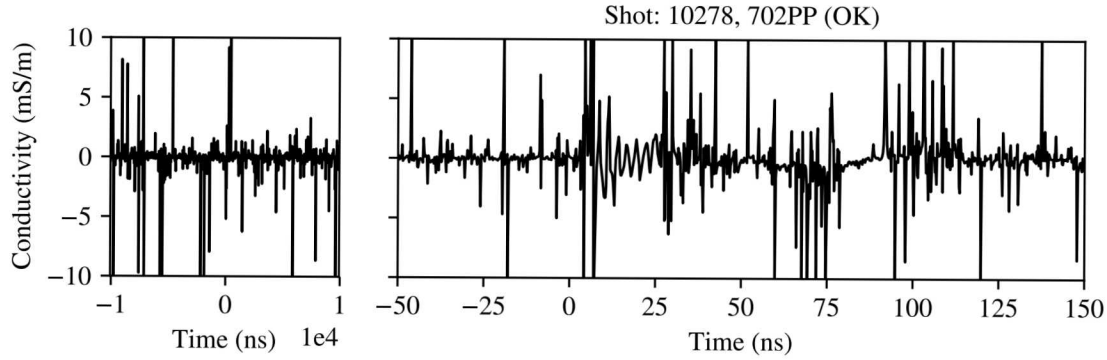
Shot: 10278, 702PP (OK)
Conductivity (mS/m)
10
5
0
−5
−10
−1
0
1
Time (ns)
1e4
−50
−25
0
25
50
75
100
125
150
Time (ns)

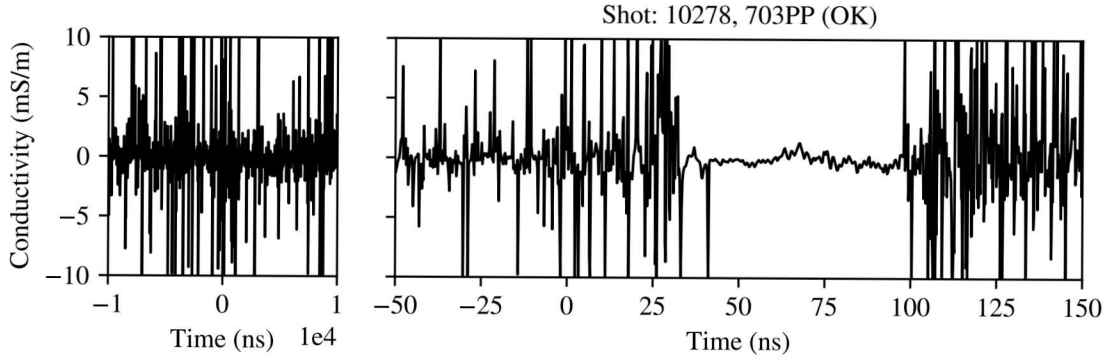
Shot: 10278, 703PP (OK)
Conductivity (mS/m)
10
5
0
−5
−10
−1
0
1
Time (ns)
1e4
−50
−25
0
25
50
75
100
125
150
Time (ns)

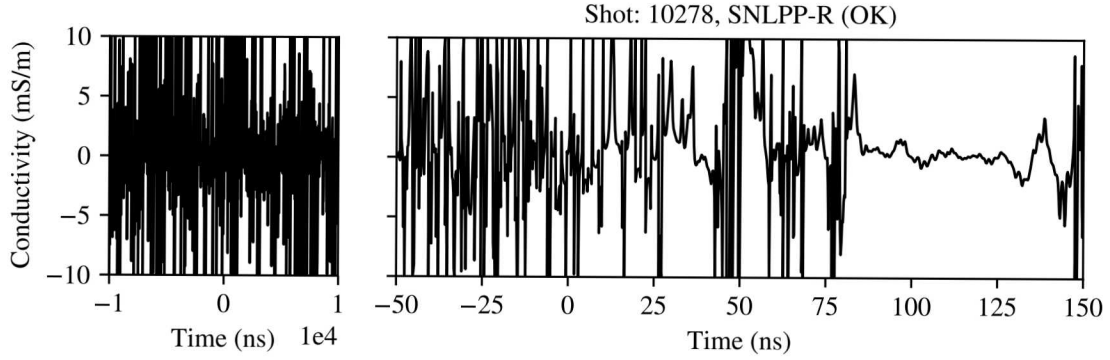
Shot: 10278, SNLPP-R (OK)
Conductivity (mS/m)
10
5
0
−5
−10
−1
0
1
Time (ns)
1e4
−50
−25
0
25
50
75
100
125
150
Time (ns)

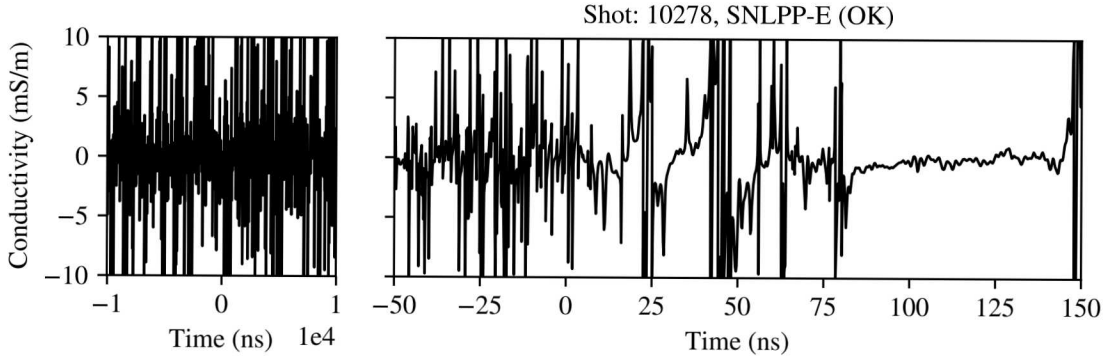
Shot: 10278, SNLPP-E (OK)
Conductivity (mS/m)
10
5
0
−5
−10
−1
0
1
Time (ns)
1e4
−50
−25
0
25
50
75
100
125
150
Time (ns)

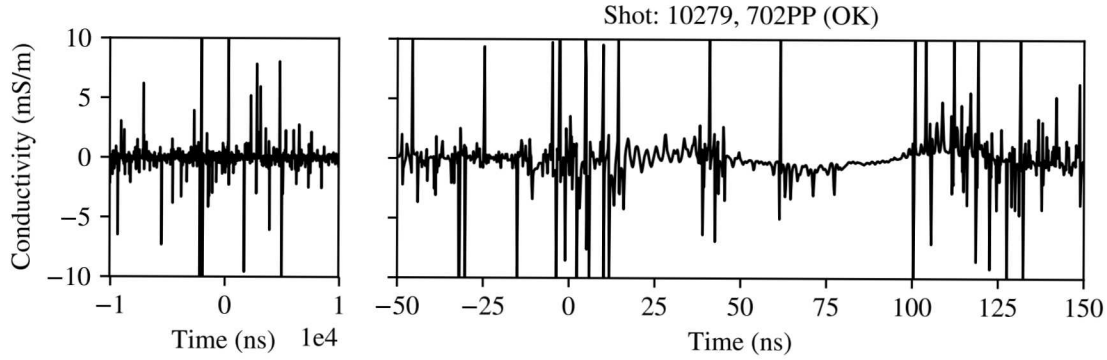
Shot: 10279, 702PP (OK)
Conductivity (mS/m)
10
5
0
−5
−10
−1
0
1
Time (ns)
1e4
−50
−25
0
25
50
75
100
125
150
Time (ns)

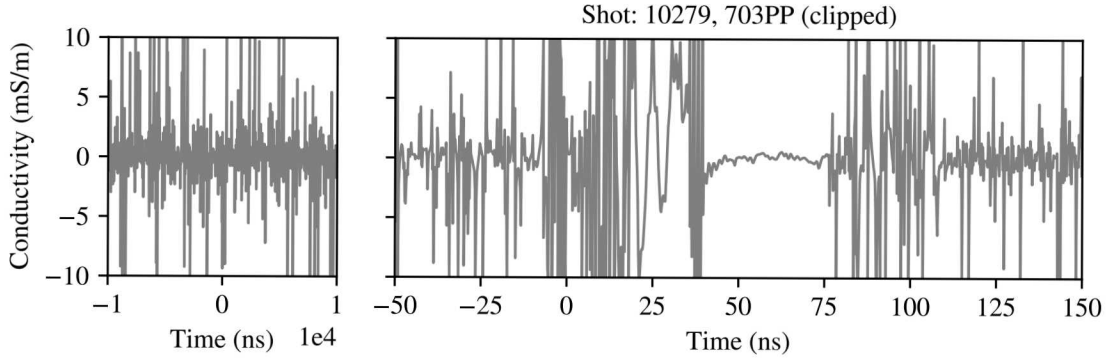
Shot: 10279, 703PP (clipped)
Conductivity (mS/m)
10
5
0
−5
−10
−1
0
1
Time (ns)
1e4
−50
−25
0
25
50
75
100
125
150
Time (ns)

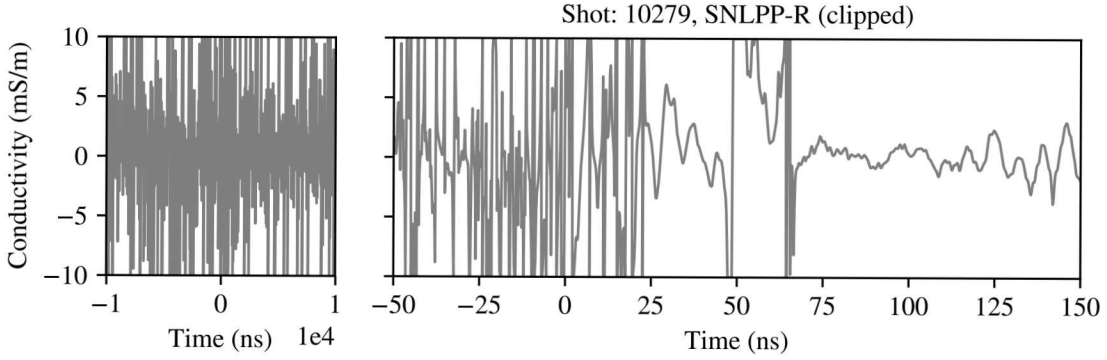
Shot: 10279, SNLPP-R (clipped)
Conductivity (mS/m)
10
5
0
−5
−10
−1
0
1
Time (ns)
1e4
−50
−25
0
25
50
75
100
125
150
Time (ns)

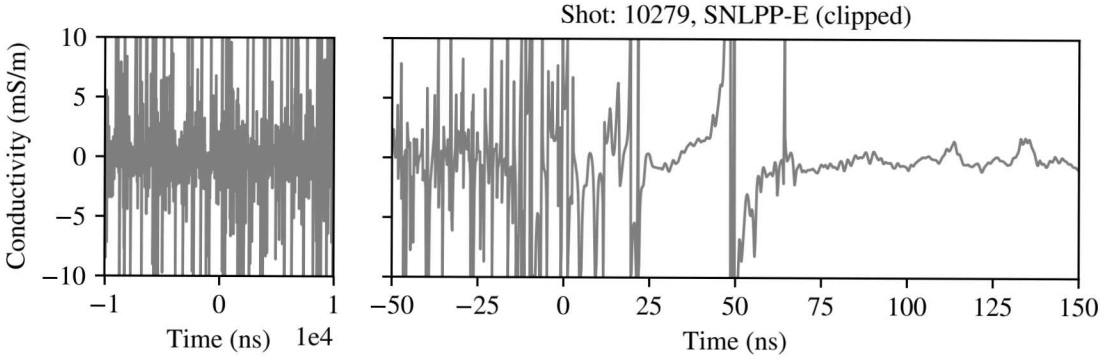
Shot: 10279, SNLPP-E (clipped)
Conductivity (mS/m)
10
5
0
−5
−10
−1
0
1
Time (ns)
1e4
−50
−25
0
25
50
75
100
125
150
Time (ns)

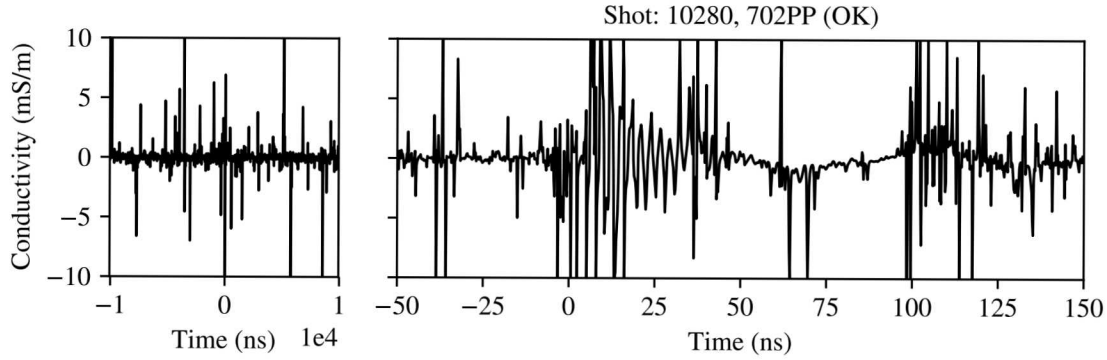
Shot: 10280, 702PP (OK)
Conductivity (mS/m)
10
5
0
−5
−10
−1
0
1
Time (ns)
1e4
−50
−25
0
25
50
75
100
125
150
Time (ns)

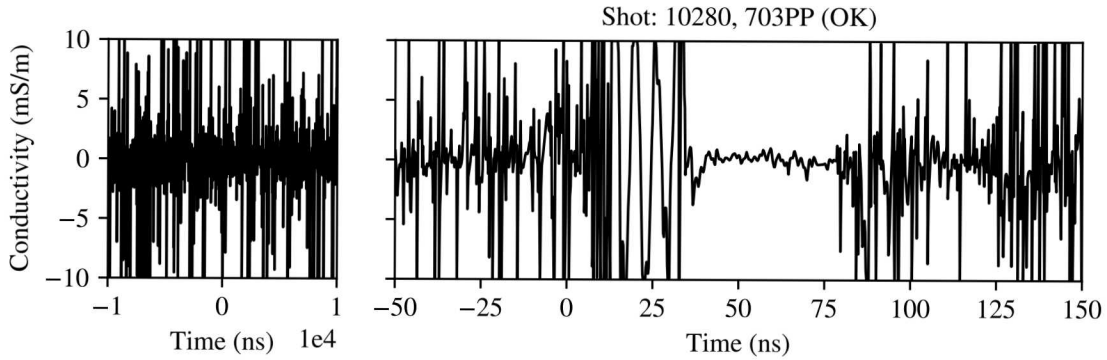
Shot: 10280, 703PP (OK)
Conductivity (mS/m)
10
5
0
−5
−10
−1
0
1
Time (ns)
1e4
−50
−25
0
25
50
75
100
125
150
Time (ns)

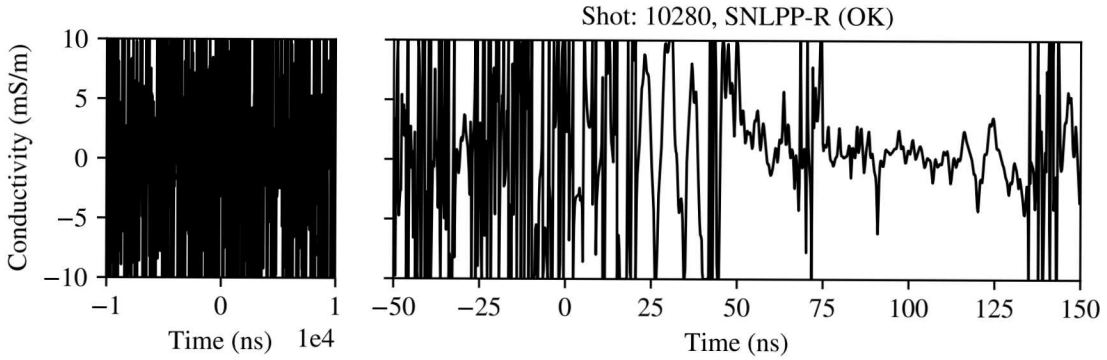
Shot: 10280, SNLPP-R (OK)
Conductivity (mS/m)
10
5
0
−5
−10
−1
0
1
Time (ns)
1e4
−50
−25
0
25
50
75
100
125
150
Time (ns)

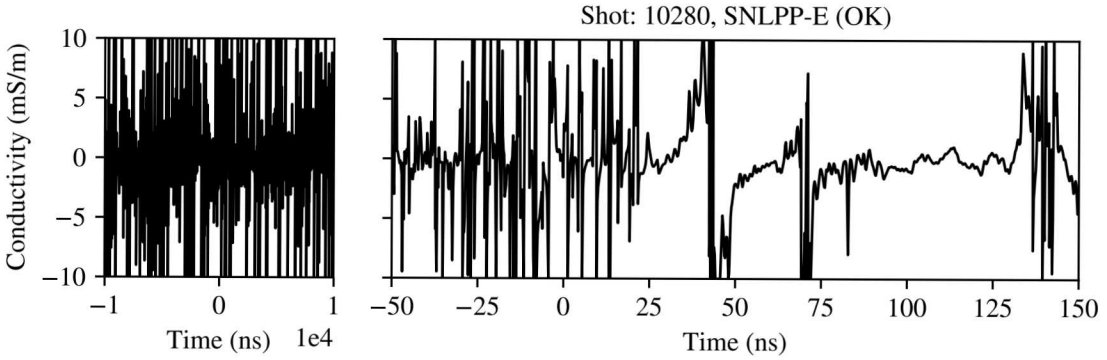
Shot: 10280, SNLPP-E (OK)
Conductivity (mS/m)
10
5
0
−5
−10
−1
0
1
Time (ns)
1e4
−50
−25
0
25
50
75
100
125
150
Time (ns)

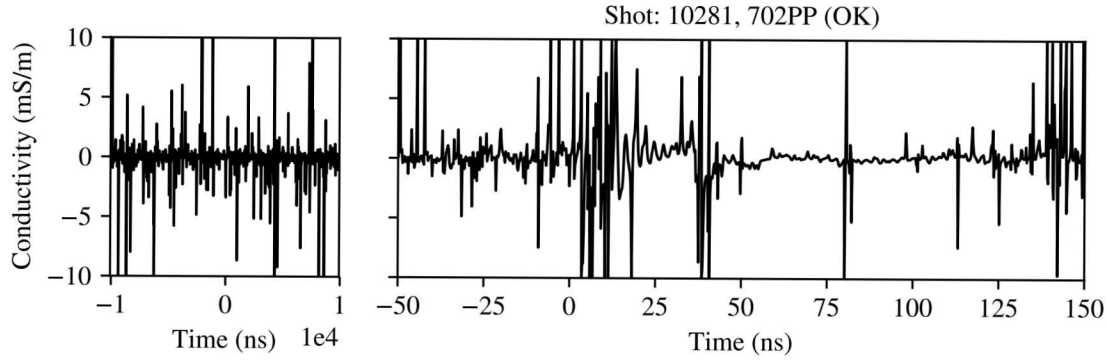
Shot: 10281, 702PP (OK)
Conductivity (mS/m)
10
5
0
−5
−10
−1
0
1
Time (ns)
1e4
−50
−25
0
25
50
75
100
125
150
Time (ns)

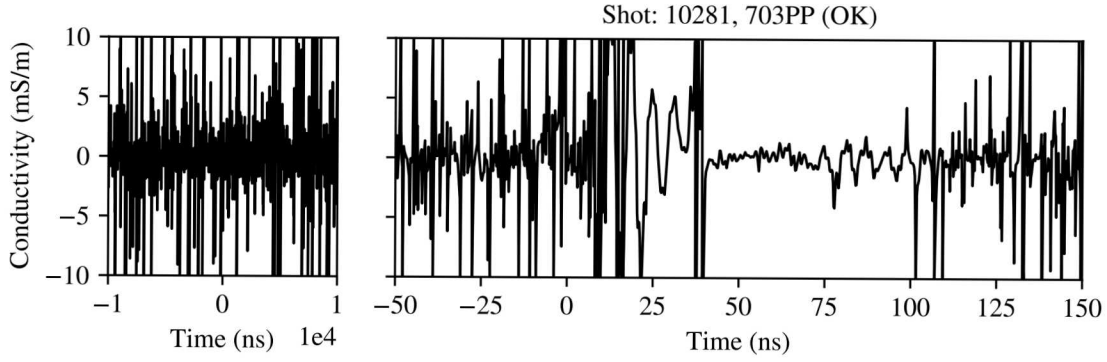
Shot: 10281, 703PP (OK)
Conductivity (mS/m)
10
5
0
−5
−10
−1
0
1
Time (ns)
1e4
−50
−25
0
25
50
75
100
125
150
Time (ns)

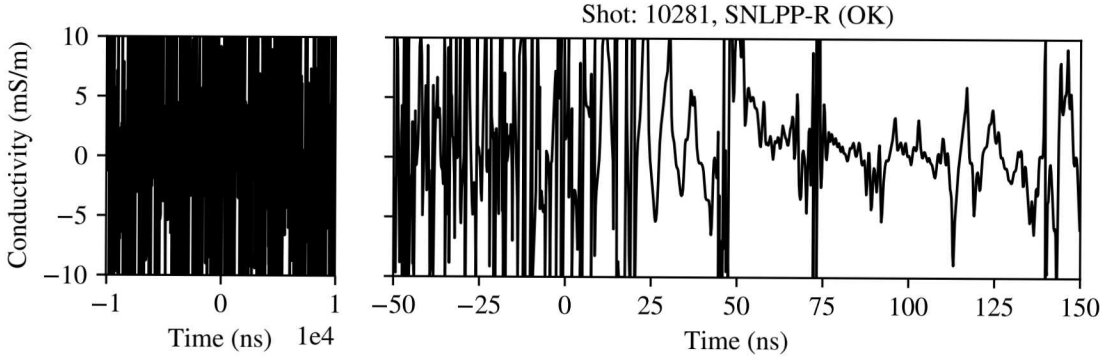
Shot: 10281, SNLPP-R (OK)
Conductivity (mS/m)
10
5
0
−5
−10
−1
0
1
Time (ns)
1e4
−50
−25
0
25
50
75
100
125
150
Time (ns)

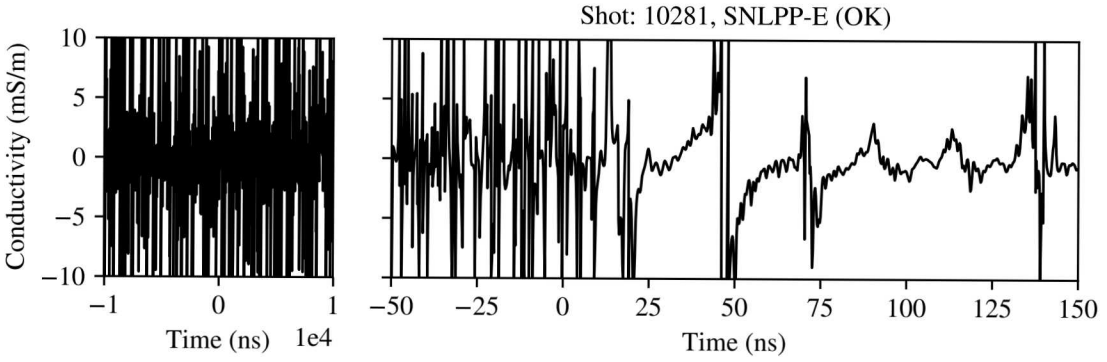
Shot: 10281, SNLPP-E (OK)
Conductivity (mS/m)
10
5
0
−5
−10
−1
0
1
Time (ns)
1e4
−50
−25
0
25
50
75
100
125
150
Time (ns)

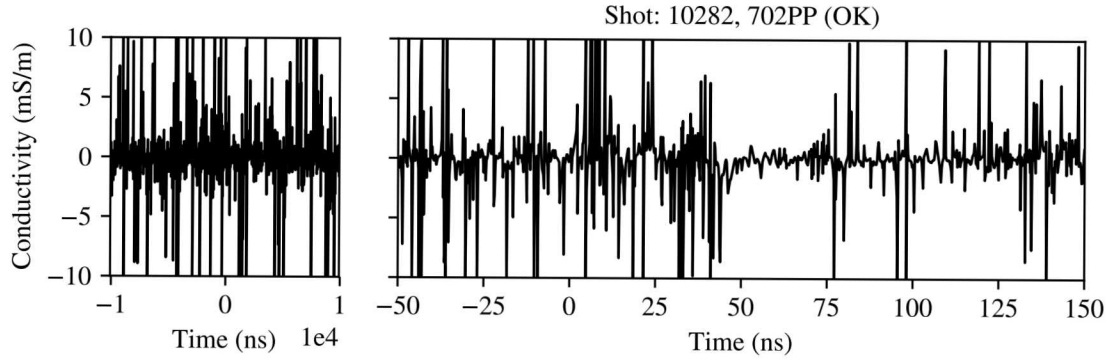
Shot: 10282, 702PP (OK)
Conductivity (mS/m)
10
5
0
−5
−10
−1
0
1
Time (ns)
1e4
−50
−25
0
25
50
75
100
125
150
Time (ns)

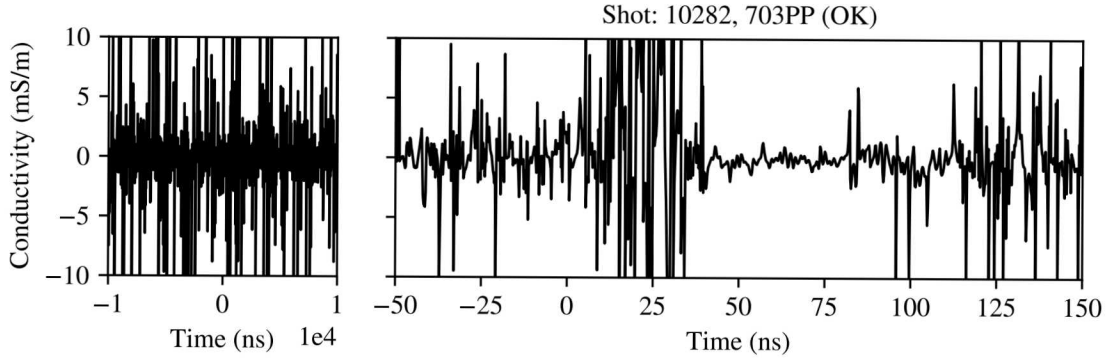
Shot: 10282, 703PP (OK)
Conductivity (mS/m)
10
5
0
−5
−10
−1
0
1
Time (ns)
1e4
−50
−25
0
25
50
75
100
125
150
Time (ns)

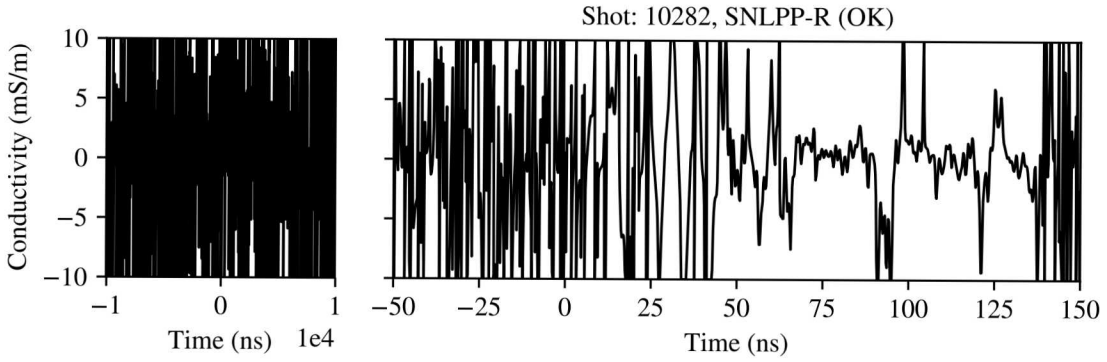
Shot: 10282, SNLPP-R (OK)
Conductivity (mS/m)
10
5
0
−5
−10
−1
0
1
Time (ns)
1e4
−50
−25
0
25
50
75
100
125
150
Time (ns)

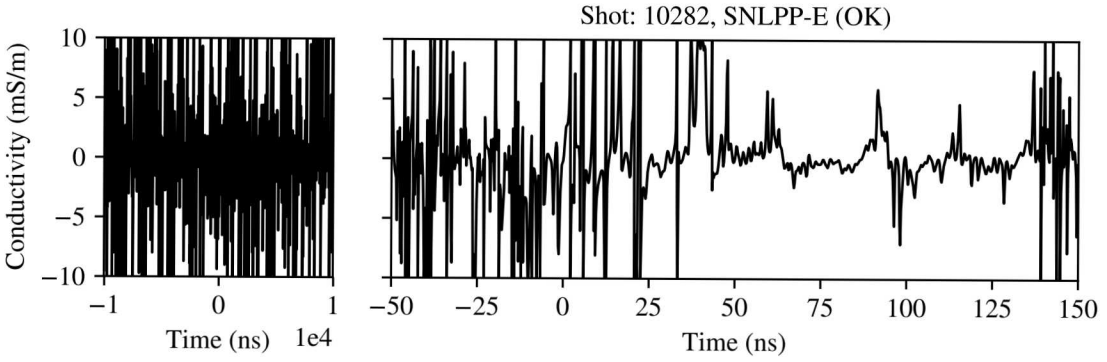
Shot: 10282, SNLPP-E (OK)
Conductivity (mS/m)
10
5
0
−5
−10
−1
0
1
Time (ns)
1e4
−50
−25
0
25
50
75
100
125
150
Time (ns)

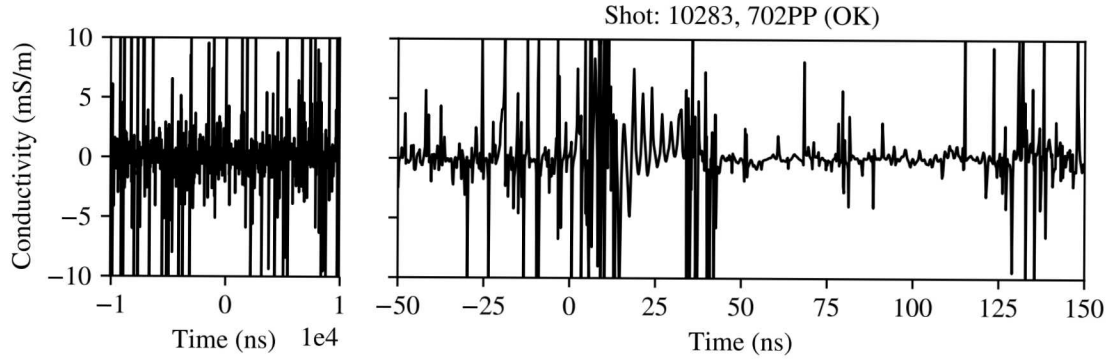
Shot: 10283, 702PP (OK)
Conductivity (mS/m)
10
5
0
−5
−10
−1
0
1
Time (ns)
1e4
−50
−25
0
25
50
75
100
125
150
Time (ns)

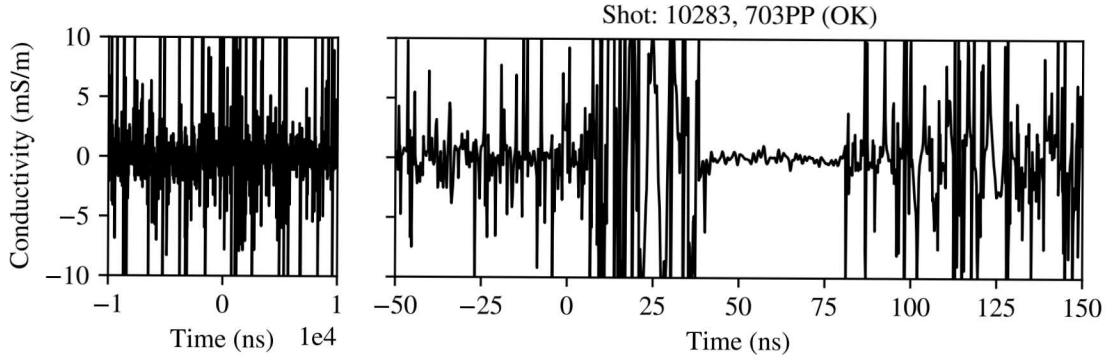
Shot: 10283, 703PP (OK)
Conductivity (mS/m)
10
5
0
−5
−10
−1
0
1
Time (ns)
1e4
−50
−25
0
25
50
75
100
125
150
Time (ns)

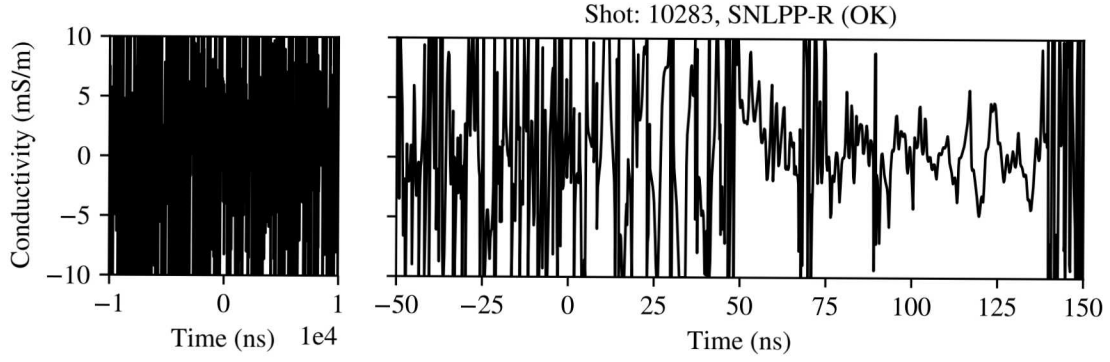
Shot: 10283, SNLPP-R (OK)
Conductivity (mS/m)
10
5
0
−5
−10
−1
0
1
Time (ns)
1e4
−50
−25
0
25
50
75
100
125
150
Time (ns)

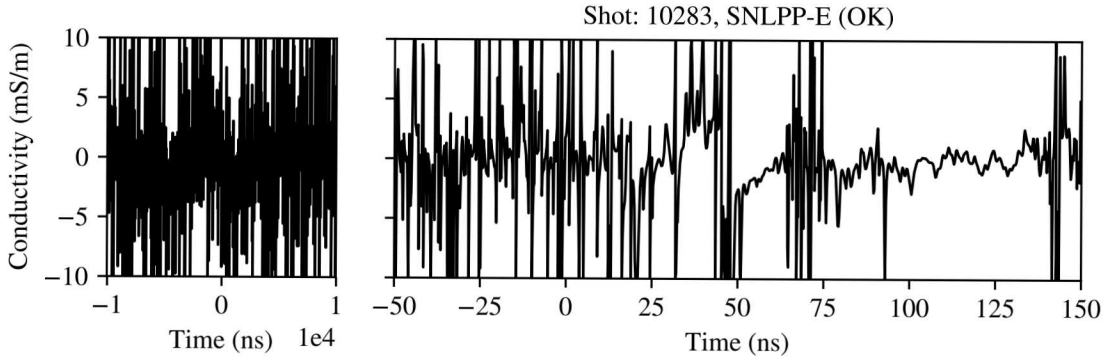
Shot: 10283, SNLPP-E (OK)
Conductivity (mS/m)
10
5
0
−5
−10
−1
0
1
Time (ns)
1e4
−50
−25
0
25
50
75
100
125
150
Time (ns)

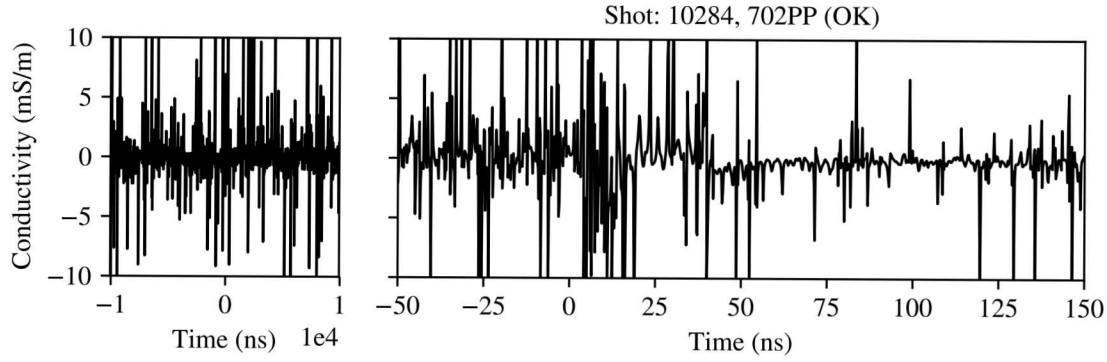
Shot: 10284, 702PP (OK)
Conductivity (mS/m)
10
5
0
−5
−10
−1
0
1
Time (ns)
1e4
−50
−25
0
25
50
75
100
125
150
Time (ns)

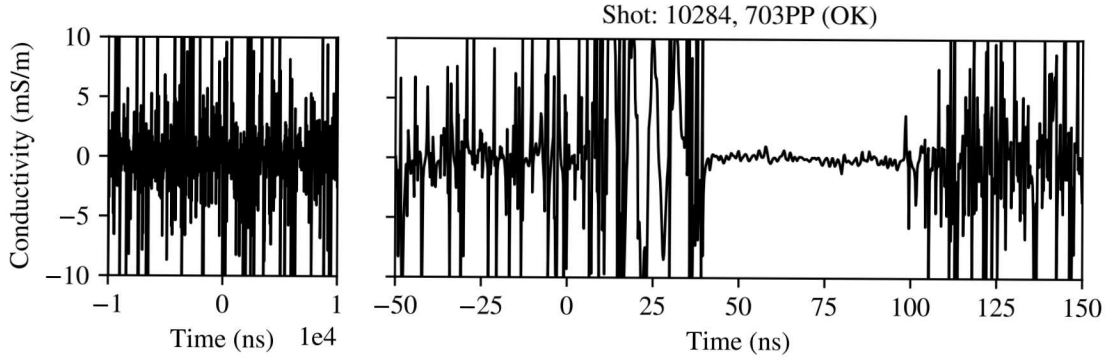
Shot: 10284, 703PP (OK)
Conductivity (mS/m)
10
5
0
−5
−10
−1
0
1
Time (ns)
1e4
−50
−25
0
25
50
75
100
125
150
Time (ns)

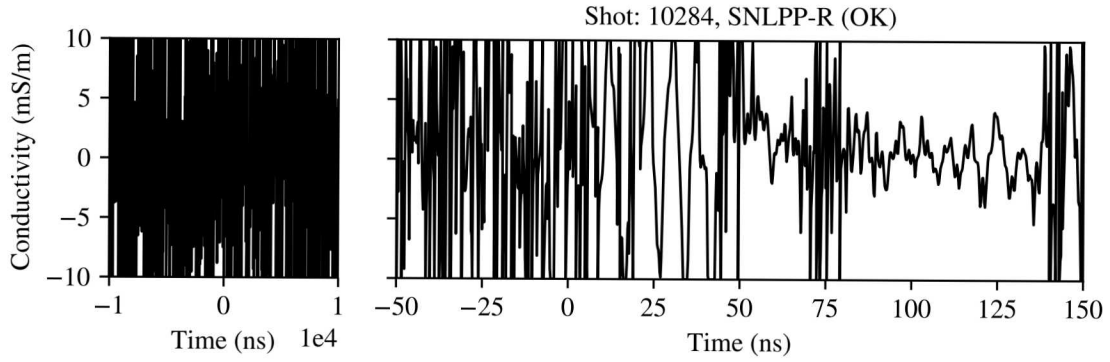
Shot: 10284, SNLPP-R (OK)
Conductivity (mS/m)
10
5
0
−5
−10
−1
0
1
Time (ns)
1e4
−50
−25
0
25
50
75
100
125
150
Time (ns)

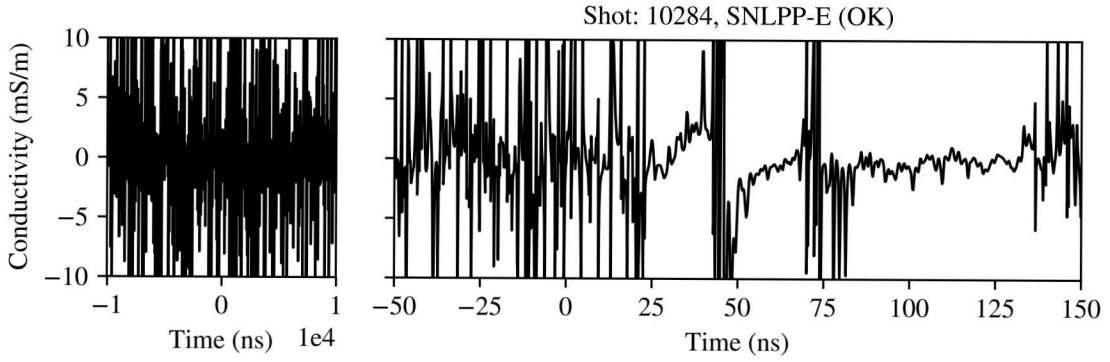
Shot: 10284, SNLPP-E (OK)
Conductivity (mS/m)
10
5
0
−5
−10
−1
0
1
Time (ns)
1e4
−50
−25
0
25
50
75
100
125
150
Time (ns)

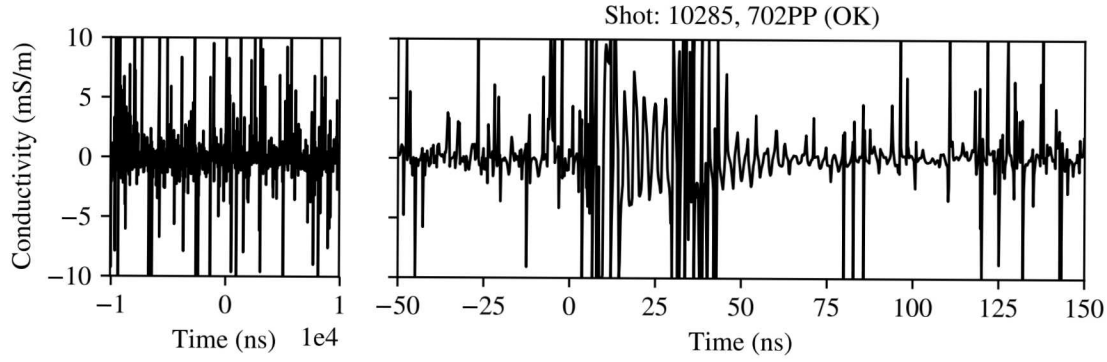
Shot: 10285, 702PP (OK)
Conductivity (mS/m)
10
5
0
−5
−10
−1
0
1
Time (ns)
1e4
−50
−25
0
25
50
75
100
125
150
Time (ns)

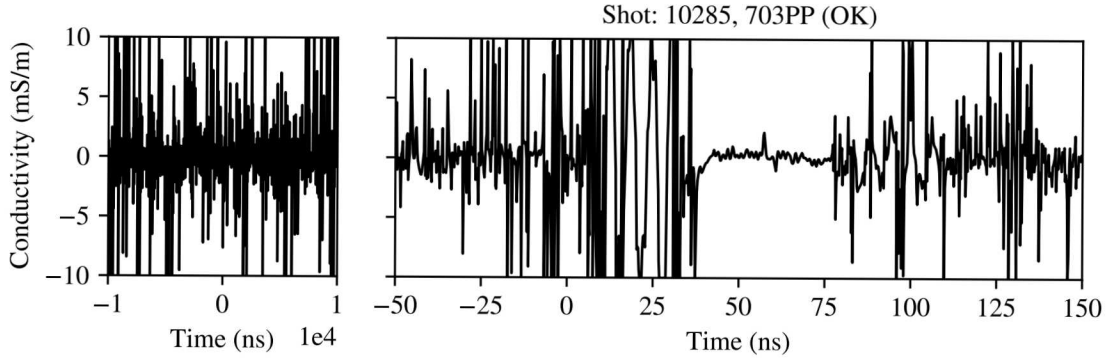
Shot: 10285, 703PP (OK)
Conductivity (mS/m)
10
5
0
−5
−10
−1
0
1
Time (ns)
1e4
−50
−25
0
25
50
75
100
125
150
Time (ns)

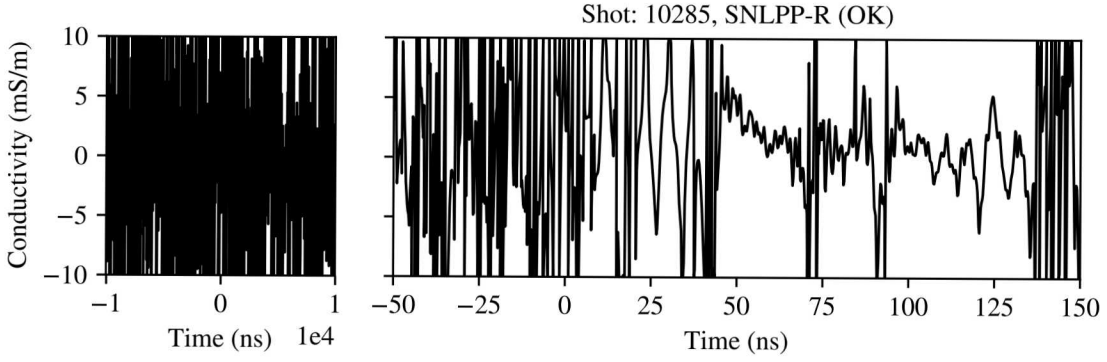
Shot: 10285, SNLPP-R (OK)
Conductivity (mS/m)
10
5
0
−5
−10
−1
0
1
Time (ns)
1e4
−50
−25
0
25
50
75
100
125
150
Time (ns)

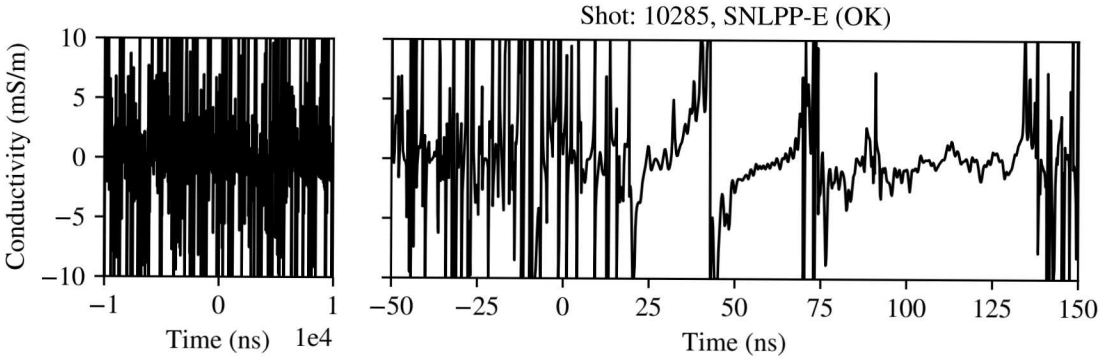
Shot: 10285, SNLPP-E (OK)
Conductivity (mS/m)
10
5
0
−5
−10
−1
0
1
Time (ns)
1e4
−50
−25
0
25
50
75
100
125
150
Time (ns)

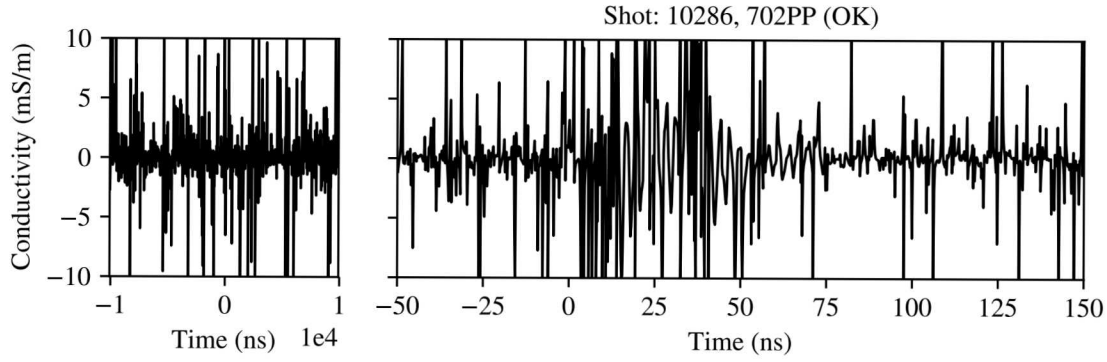
Shot: 10286, 702PP (OK)
Conductivity (mS/m)
10
5
0
−5
−10
−1
0
1
Time (ns)
1e4
−50
−25
0
25
50
75
100
125
150
Time (ns)

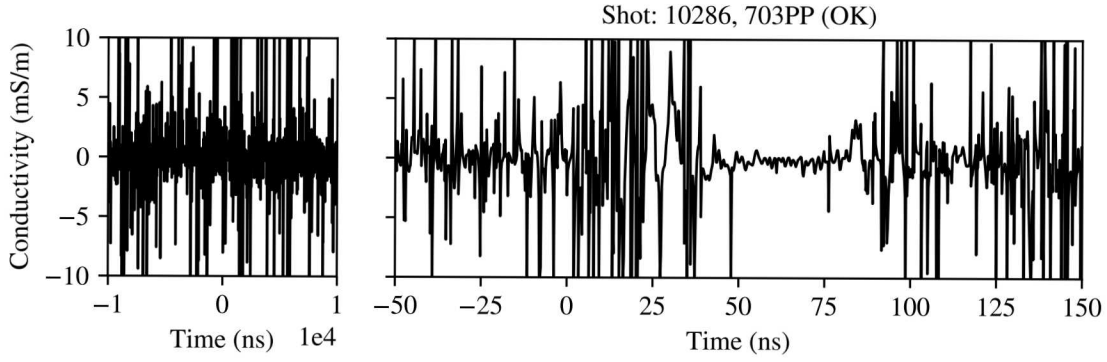
Shot: 10286, 703PP (OK)
Conductivity (mS/m)
10
5
0
−5
−10
−1
0
1
Time (ns)
1e4
−50
−25
0
25
50
75
100
125
150
Time (ns)

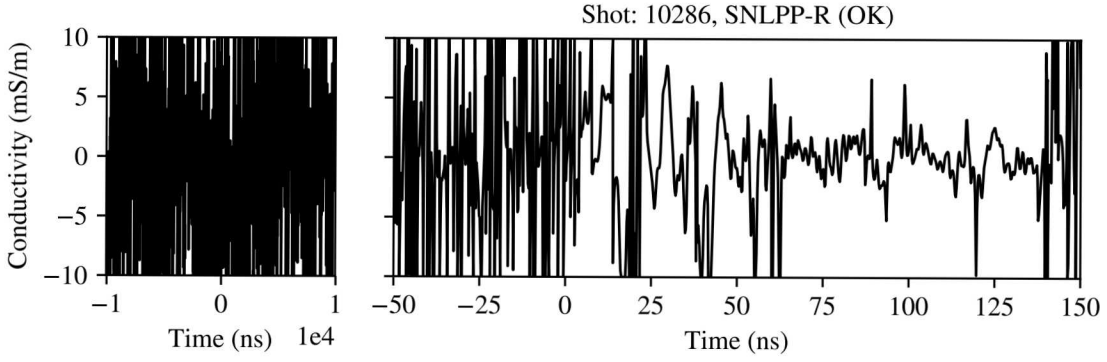
Shot: 10286, SNLPP-R (OK)
Conductivity (mS/m)
10
5
0
−5
−10
−1
0
1
Time (ns)
1e4
−50
−25
0
25
50
75
100
125
150
Time (ns)

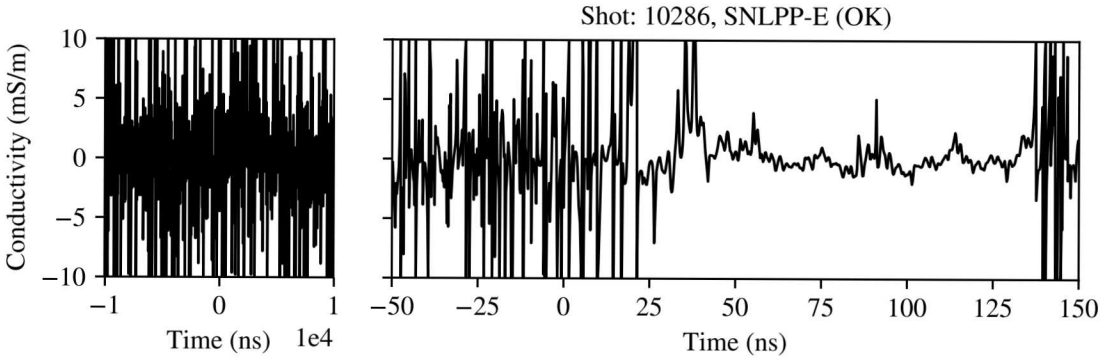
Shot: 10286, SNLPP-E (OK)
Conductivity (mS/m)
10
5
0
−5
−10
−1
0
1
Time (ns)
1e4
−50
−25
0
25
50
75
100
125
150
Time (ns)

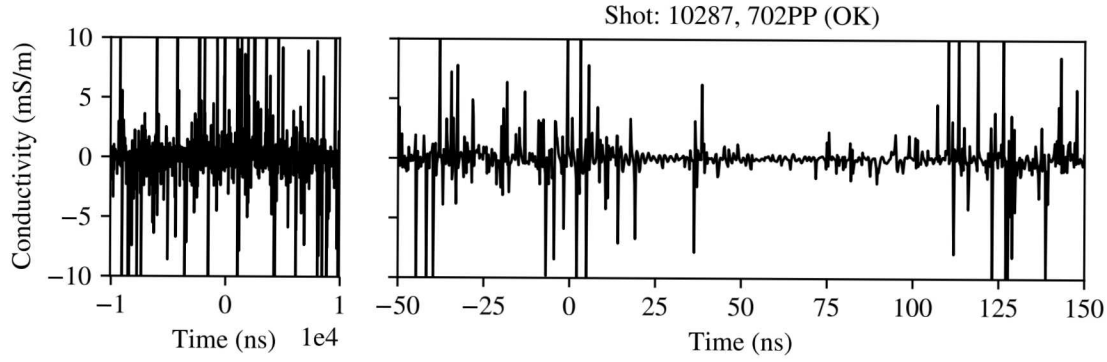
Shot: 10287, 702PP (OK)
Conductivity (mS/m)
10
5
0
−5
−10
−1
0
1
Time (ns)
1e4
−50
−25
0
25
50
75
100
125
150
Time (ns)

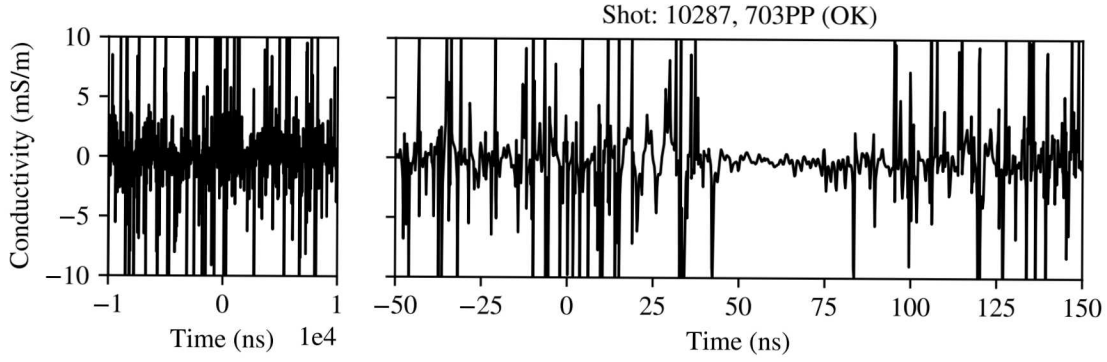
Shot: 10287, 703PP (OK)
Conductivity (mS/m)
10
5
0
−5
−10
−1
0
1
Time (ns)
1e4
−50
−25
0
25
50
75
100
125
150
Time (ns)

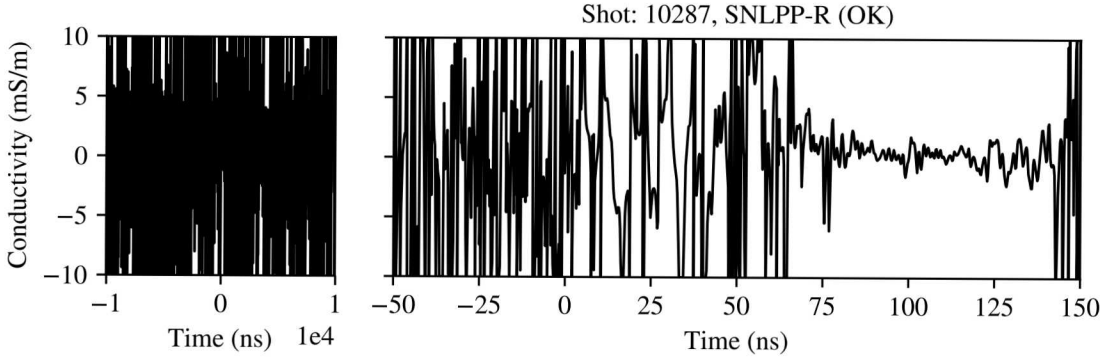
Shot: 10287, SNLPP-R (OK)
Conductivity (mS/m)
10
5
0
−5
−10
−1
0
1
Time (ns)
1e4
−50
−25
0
25
50
75
100
125
150
Time (ns)

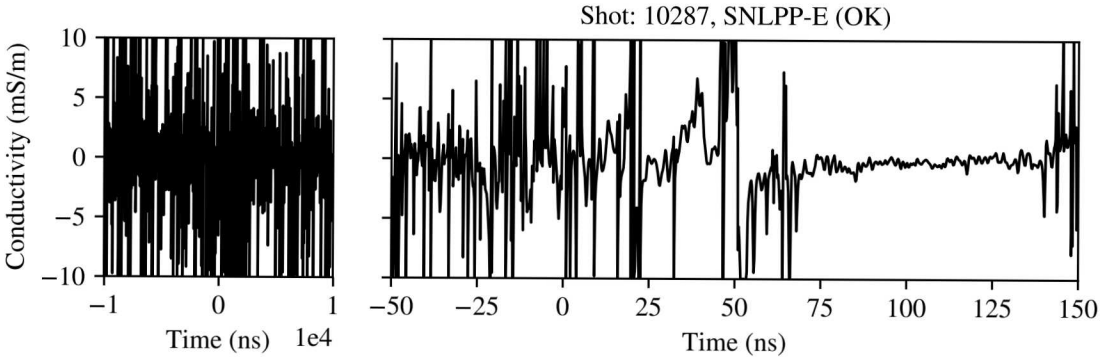
Shot: 10287, SNLPP-E (OK)
Conductivity (mS/m)
10
5
0
−5
−10
−1
0
1
Time (ns)
1e4
−50
−25
0
25
50
75
100
125
150
Time (ns)

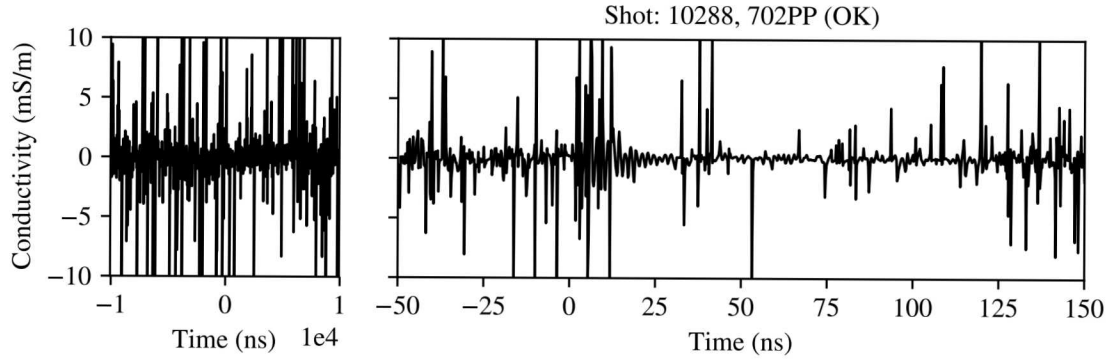
Shot: 10288, 702PP (OK)
Conductivity (mS/m)
10
5
0
−5
−10
−1
0
1
Time (ns)
1e4
−50
−25
0
25
50
75
100
125
150
Time (ns)

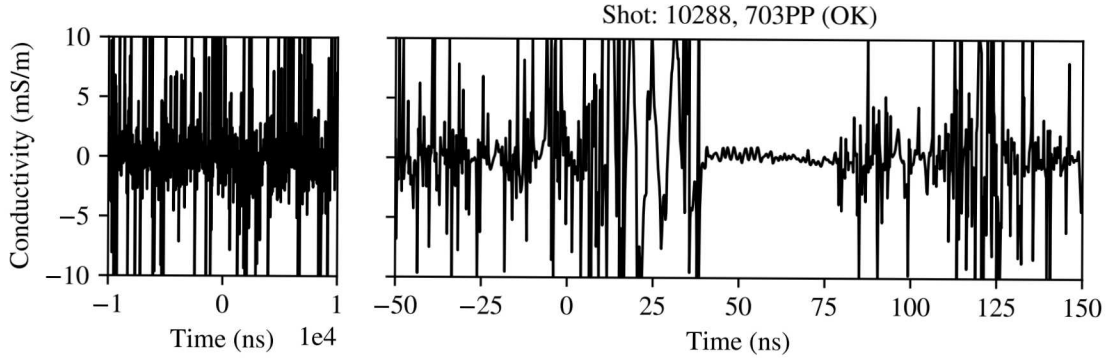
Shot: 10288, 703PP (OK)
Conductivity (mS/m)
10
5
0
−5
−10
−1
0
1
Time (ns)
1e4
−50
−25
0
25
50
75
100
125
150
Time (ns)

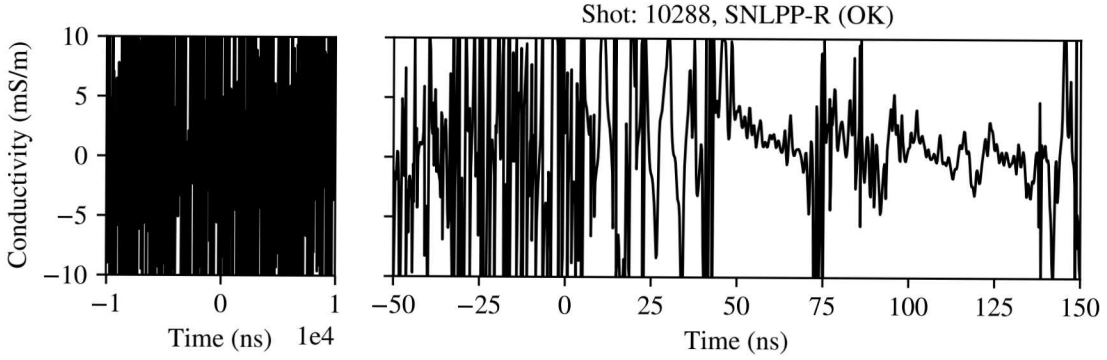
Shot: 10288, SNLPP-R (OK)
Conductivity (mS/m)
10
5
0
−5
−10
−1
0
1
Time (ns)
1e4
−50
−25
0
25
50
75
100
125
150
Time (ns)

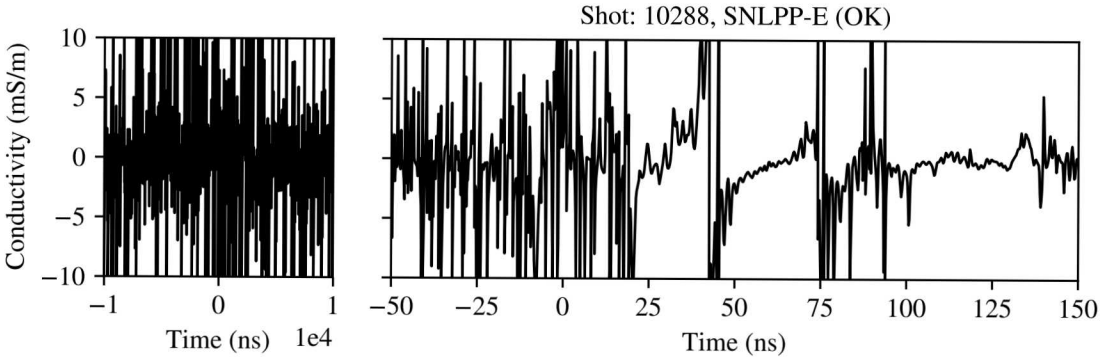
Shot: 10288, SNLPP-E (OK)
Conductivity (mS/m)
10
5
0
−5
−10
−1
0
1
Time (ns)
1e4
−50
−25
0
25
50
75
100
125
150
Time (ns)

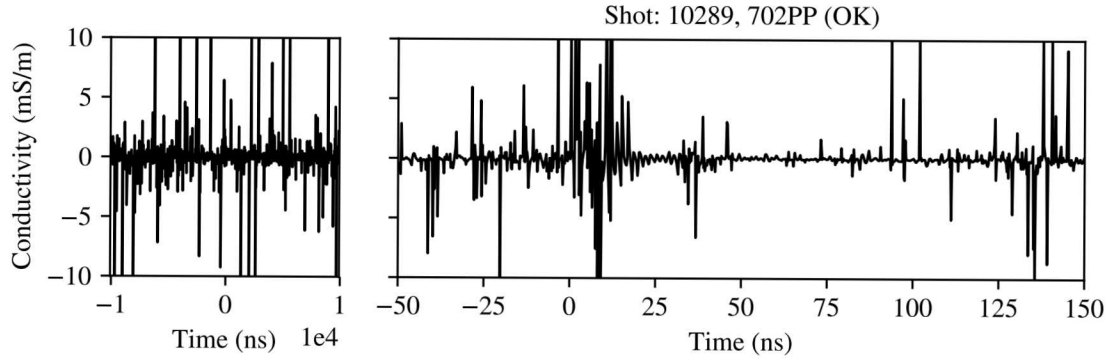
Shot: 10289, 702PP (OK)
Conductivity (mS/m)
10
5
0
−5
−10
−1
0
1
Time (ns)
1e4
−50
−25
0
25
50
75
100
125
150
Time (ns)

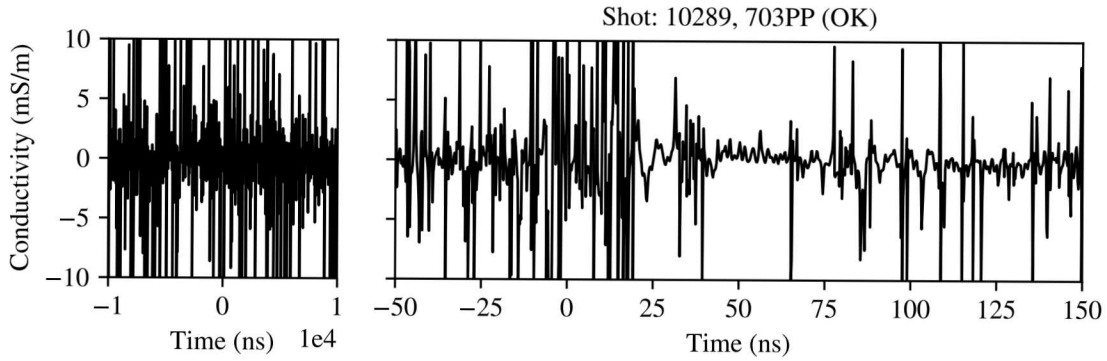
Shot: 10289, 703PP (OK)
Conductivity (mS/m)
10
5
0
−5
−10
−1
0
1
Time (ns)
1e4
−50
−25
0
25
50
75
100
125
150
Time (ns)

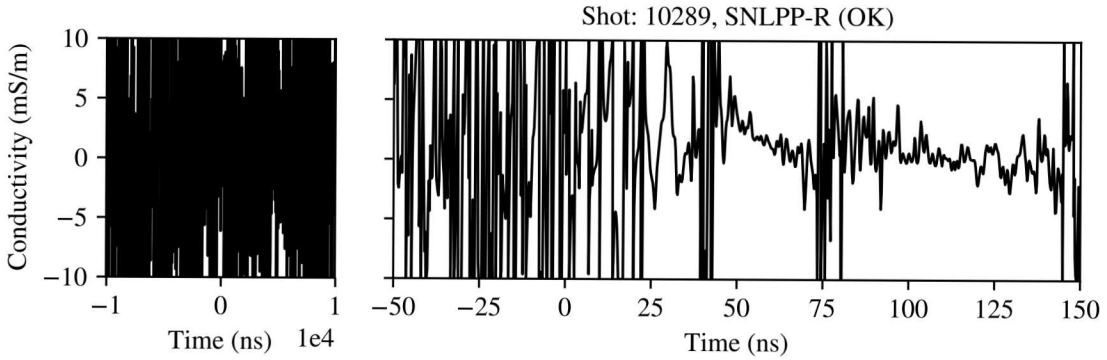
Shot: 10289, SNLPP-R (OK)
Conductivity (mS/m)
10
5
0
−5
−10
−1
0
1
Time (ns)
1e4
−50
−25
0
25
50
75
100
125
150
Time (ns)

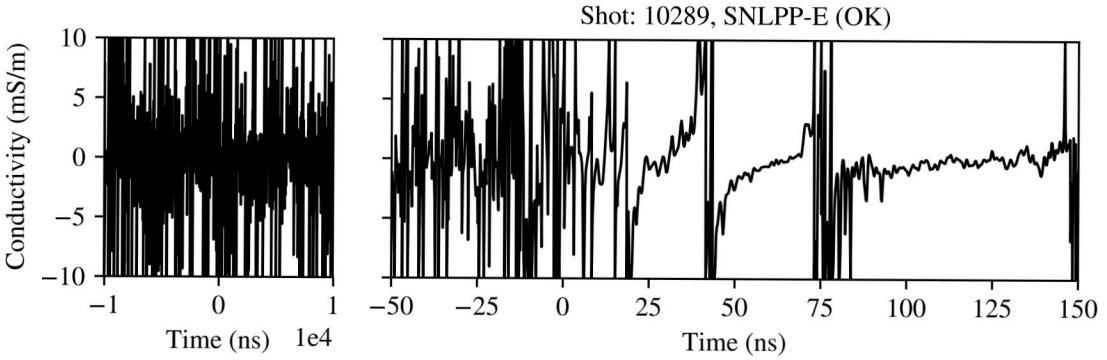
Shot: 10289, SNLPP-E (OK)
Conductivity (mS/m)
10
5
0
−5
−10
−1
0
1
Time (ns)
1e4
−50
−25
0
25
50
75
100
125
150
Time (ns)

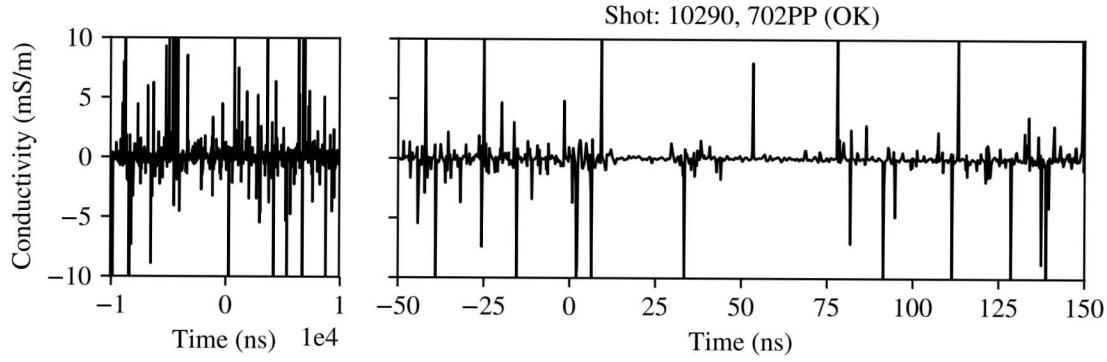
Shot: 10290, 702PP (OK)
Conductivity (mS/m)
10
5
0
−5
−10
−1
0
1
Time (ns)
1e4
−50
−25
0
25
50
75
100
125
150
Time (ns)

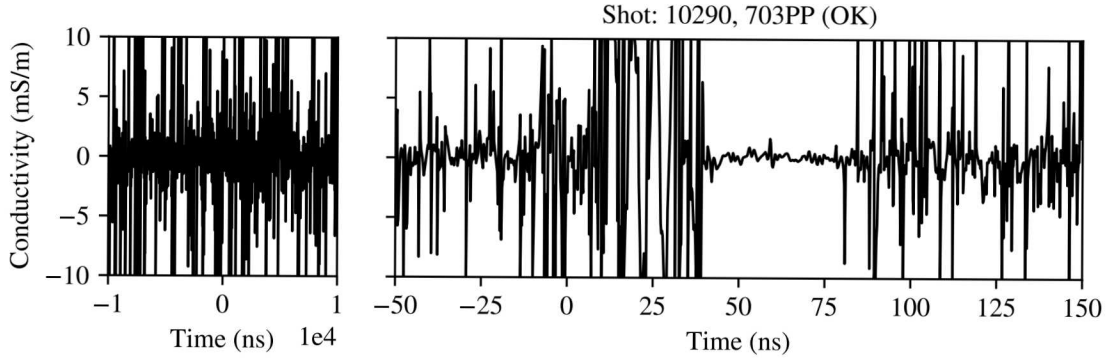
Shot: 10290, 703PP (OK)
Conductivity (mS/m)
10
5
0
−5
−10
−1
0
1
Time (ns)
1e4
−50
−25
0
25
50
75
100
125
150
Time (ns)

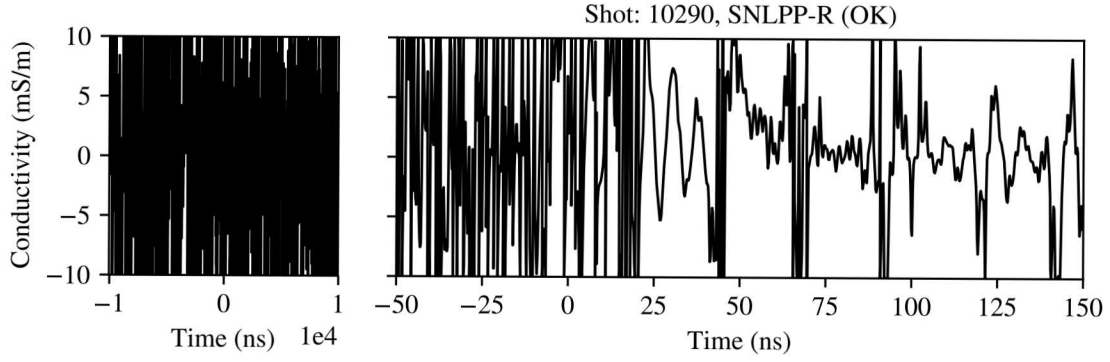
Shot: 10290, SNLPP-R (OK)
Conductivity (mS/m)
10
5
0
−5
−10
−1
0
1
Time (ns)
1e4
−50
−25
0
25
50
75
100
125
150
Time (ns)

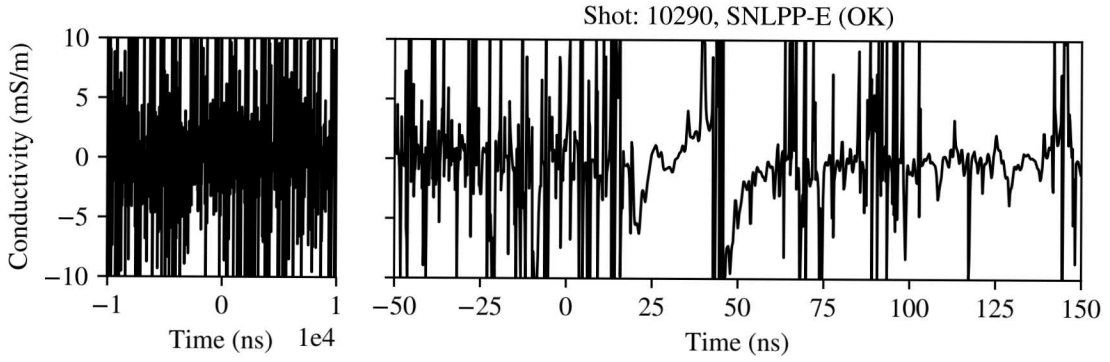
Shot: 10290, SNLPP-E (OK)
Conductivity (mS/m)
10
5
0
−5
−10
−1
0
1
Time (ns)
1e4
−50
−25
0
25
50
75
100
125
150
Time (ns)

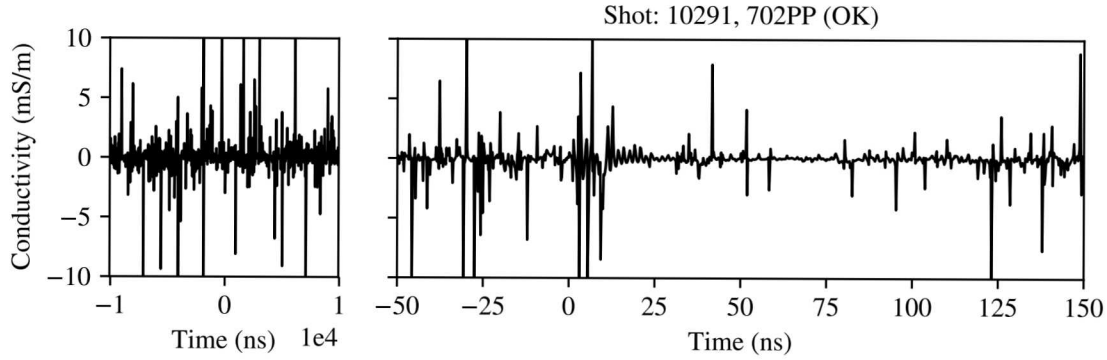
Shot: 10291, 702PP (OK)
Conductivity (mS/m)
10
5
0
−5
−10
−1
0
1
Time (ns)
1e4
−50
−25
0
25
50
75
100
125
150
Time (ns)

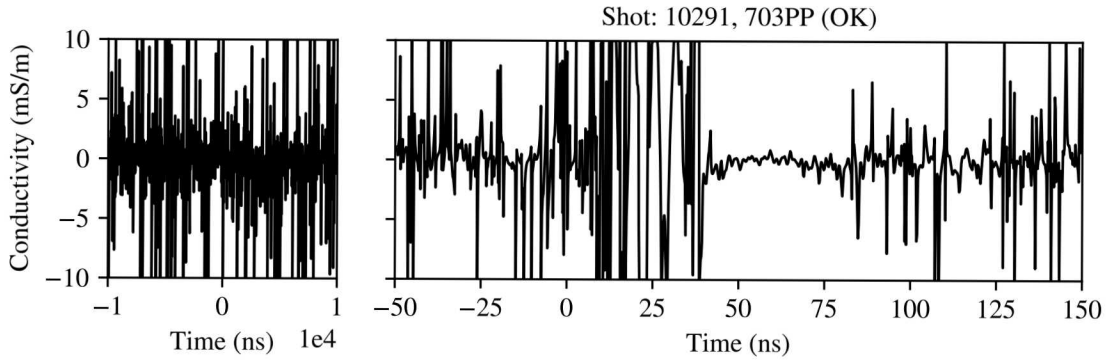
Shot: 10291, 703PP (OK)
Conductivity (mS/m)
10
5
0
−5
−10
−1
0
1
Time (ns)
1e4
−50
−25
0
25
50
75
100
125
150
Time (ns)

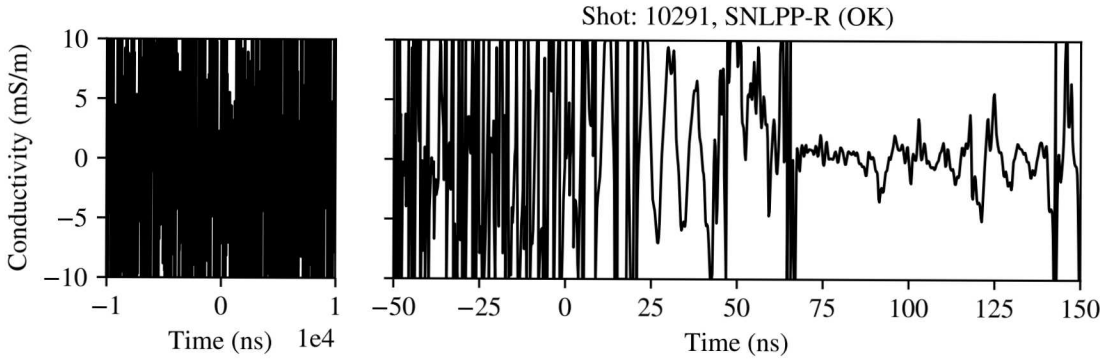
Shot: 10291, SNLPP-R (OK)
Conductivity (mS/m)
10
5
0
−5
−10
−1
0
1
Time (ns)
1e4
−50
−25
0
25
50
75
100
125
150
Time (ns)

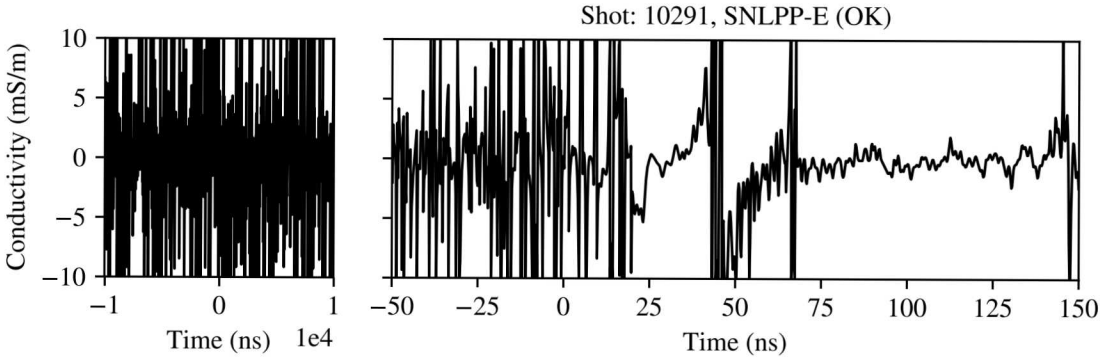
Shot: 10291, SNLPP-E (OK)
Conductivity (mS/m)
10
5
0
−5
−10
−1
0
1
Time (ns)
1e4
−50
−25
0
25
50
75
100
125
150
Time (ns)

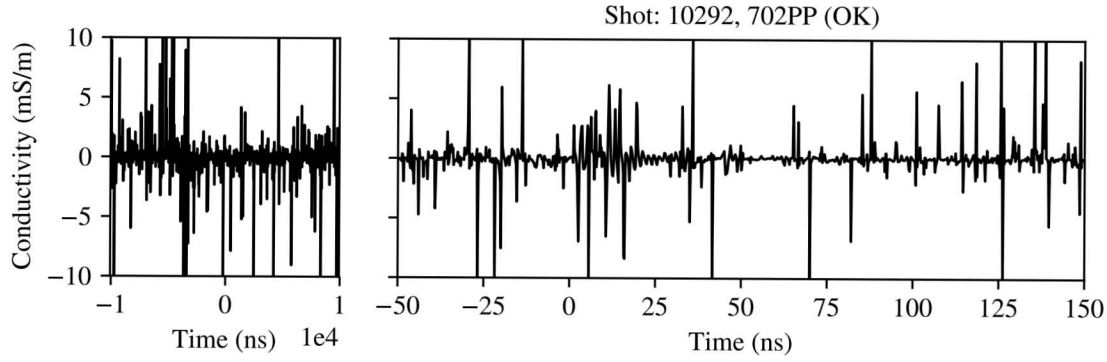
Shot: 10292, 702PP (OK)
Conductivity (mS/m)
10
5
0
−5
−10
−1
0
1
Time (ns)
1e4
−50
−25
0
25
50
75
100
125
150
Time (ns)

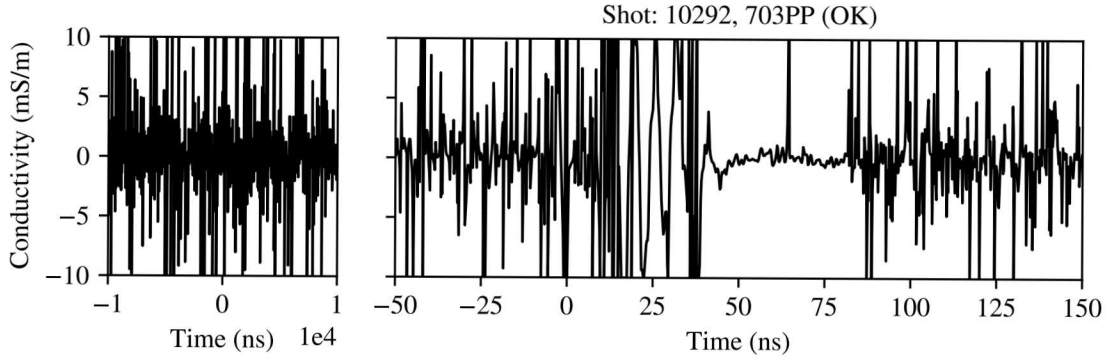
Shot: 10292, 703PP (OK)
Conductivity (mS/m)
10
5
0
−5
−10
−1
0
1
Time (ns)
1e4
−50
−25
0
25
50
75
100
125
150
Time (ns)

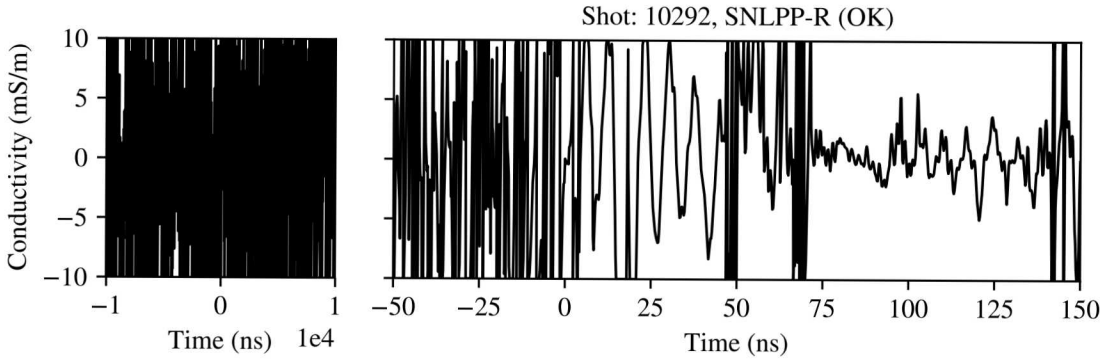
Shot: 10292, SNLPP-R (OK)
Conductivity (mS/m)
10
5
0
−5
−10
−1
0
1
Time (ns)
1e4
−50
−25
0
25
50
75
100
125
150
Time (ns)

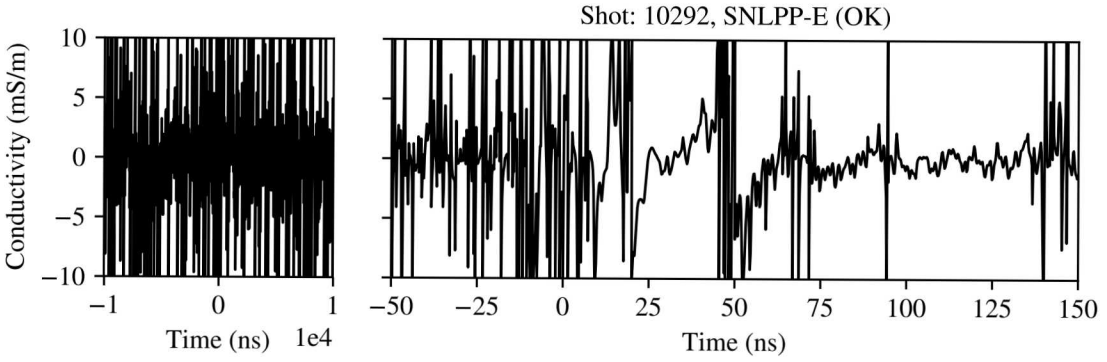
Shot: 10292, SNLPP-E (OK)
Conductivity (mS/m)
10
5
0
−5
−10
−1
0
1
Time (ns)
1e4
−50
−25
0
25
50
75
100
125
150
Time (ns)

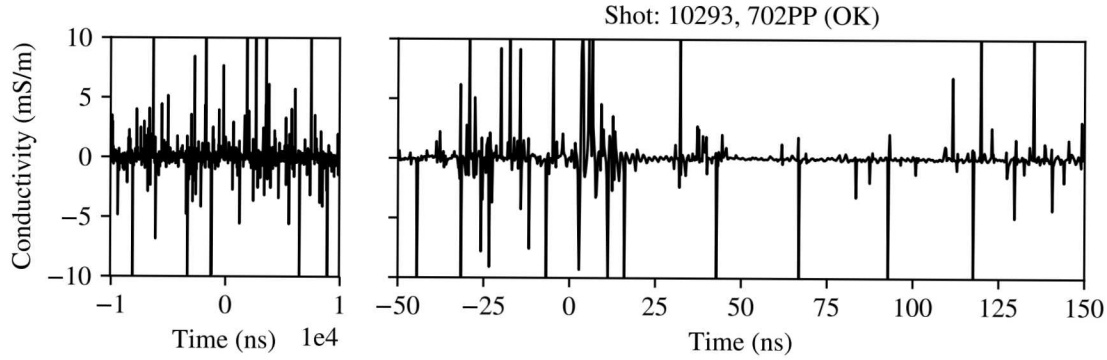
Shot: 10293, 702PP (OK)
Conductivity (mS/m)
10
5
0
−5
−10
−1
0
1
Time (ns)
1e4
−50
−25
0
25
50
75
100
125
150
Time (ns)

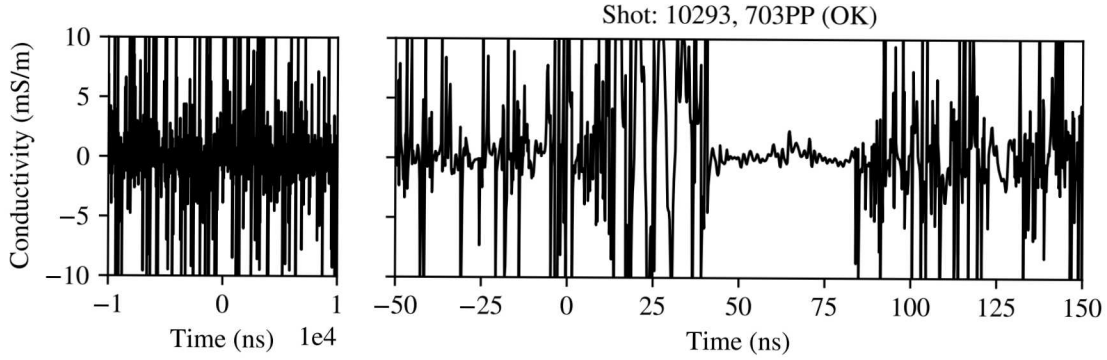
Shot: 10293, 703PP (OK)
Conductivity (mS/m)
10
5
0
−5
−10
−1
0
1
Time (ns)
1e4
−50
−25
0
25
50
75
100
125
150
Time (ns)

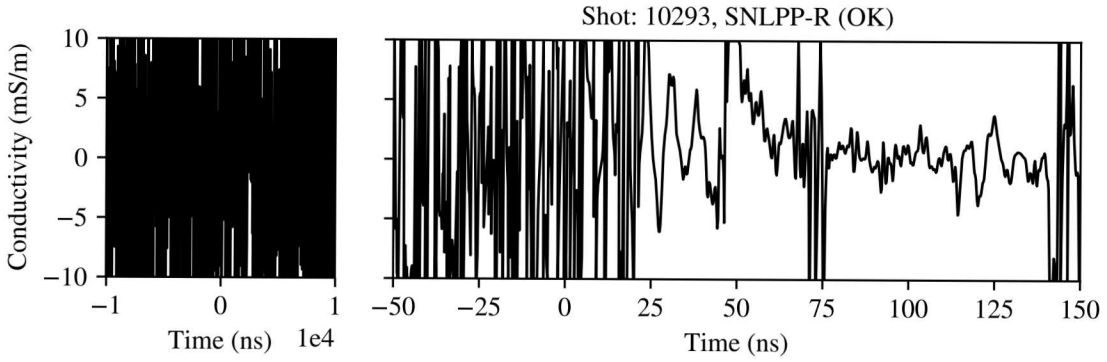
Shot: 10293, SNLPP-R (OK)
Conductivity (mS/m)
10
5
0
−5
−10
−1
0
1
Time (ns)
1e4
−50
−25
0
25
50
75
100
125
150
Time (ns)

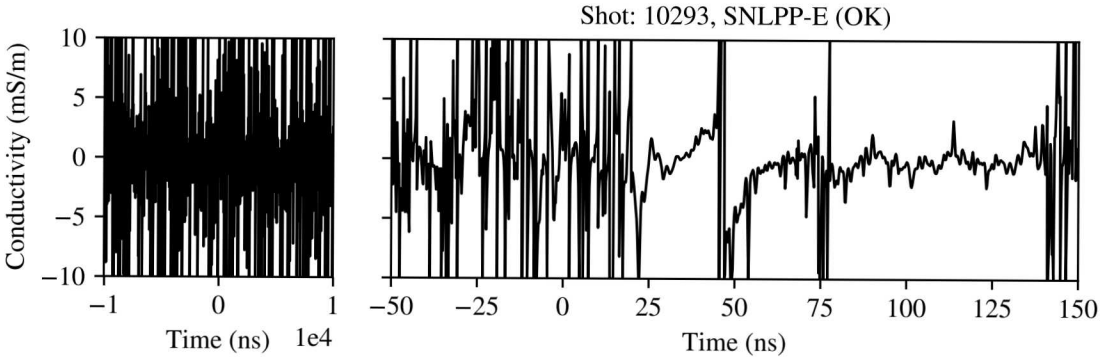
Shot: 10293, SNLPP-E (OK)
Conductivity (mS/m)
10
5
0
−5
−10
−1
0
1
Time (ns)
1e4
−50
−25
0
25
50
75
100
125
150
Time (ns)

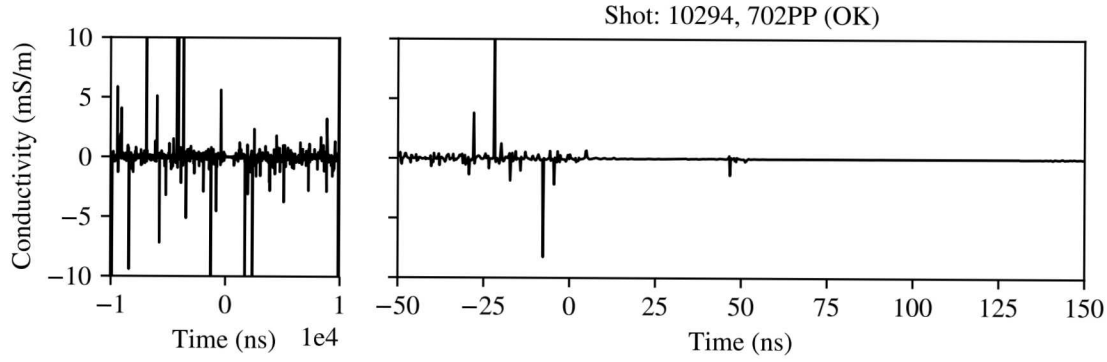
Shot: 10294, 702PP (OK)
Conductivity (mS/m)
10
5
0
−5
−10
−1
0
1
Time (ns)
1e4
−50
−25
0
25
50
75
100
125
150
Time (ns)

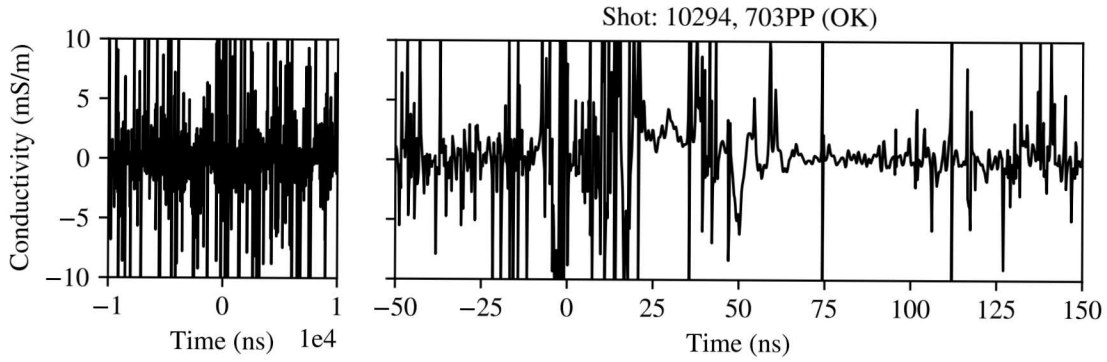
Shot: 10294, 703PP (OK)
Conductivity (mS/m)
10
5
0
−5
−10
−1
0
1
Time (ns)
1e4
−50
−25
0
25
50
75
100
125
150
Time (ns)

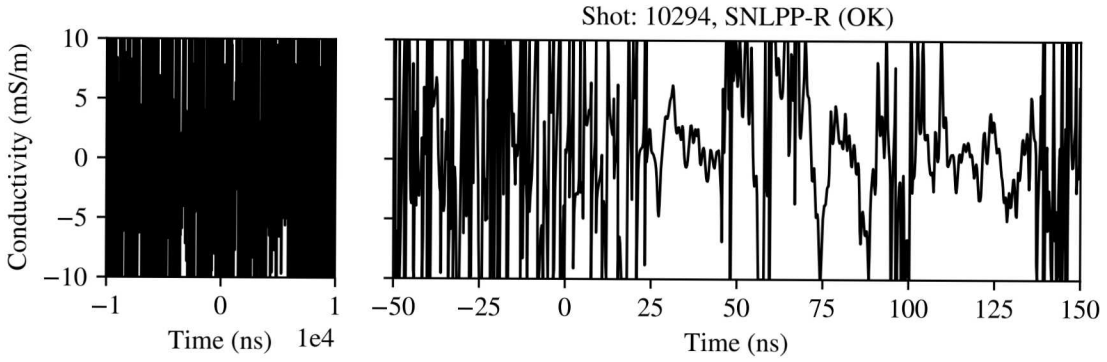
Shot: 10294, SNLPP-R (OK)
Conductivity (mS/m)
10
5
0
−5
−10
−1
0
1
Time (ns)
1e4
−50
−25
0
25
50
75
100
125
150
Time (ns)

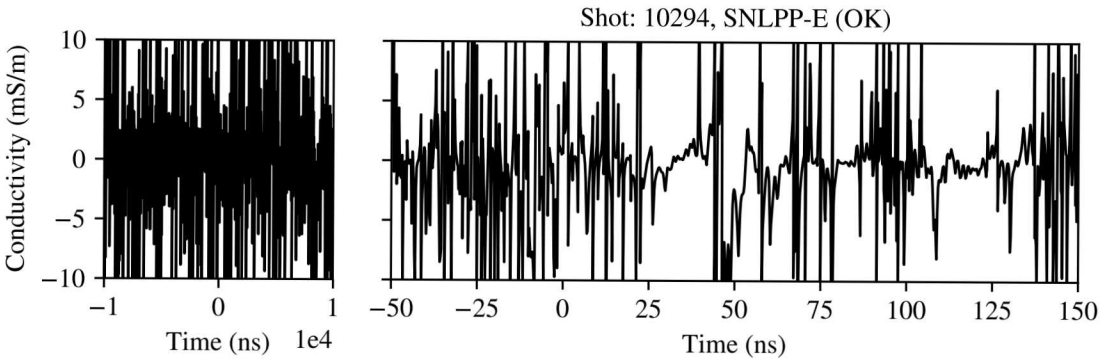
Shot: 10294, SNLPP-E (OK)
Conductivity (mS/m)
10
5
0
−5
−10
−1
0
1
Time (ns)
1e4
−50
−25
0
25
50
75
100
125
150
Time (ns)

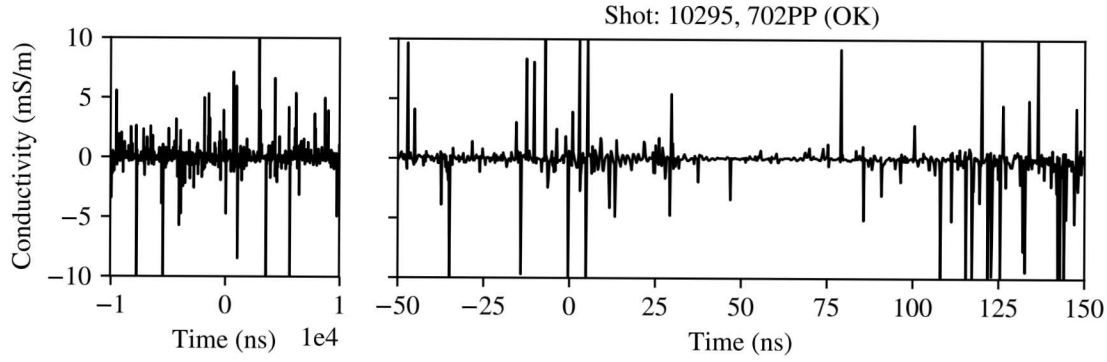
Shot: 10295, 702PP (OK)
Conductivity (mS/m)
10
5
0
−5
−10
−1
0
1
Time (ns)
1e4
−50
−25
0
25
50
75
100
125
150
Time (ns)

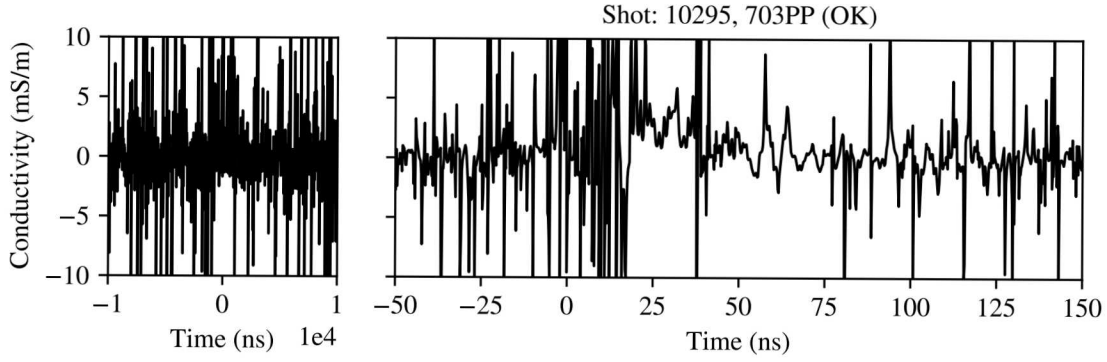
Shot: 10295, 703PP (OK)
Conductivity (mS/m)
10
5
0
−5
−10
−1
0
1
Time (ns)
1e4
−50
−25
0
25
50
75
100
125
150
Time (ns)

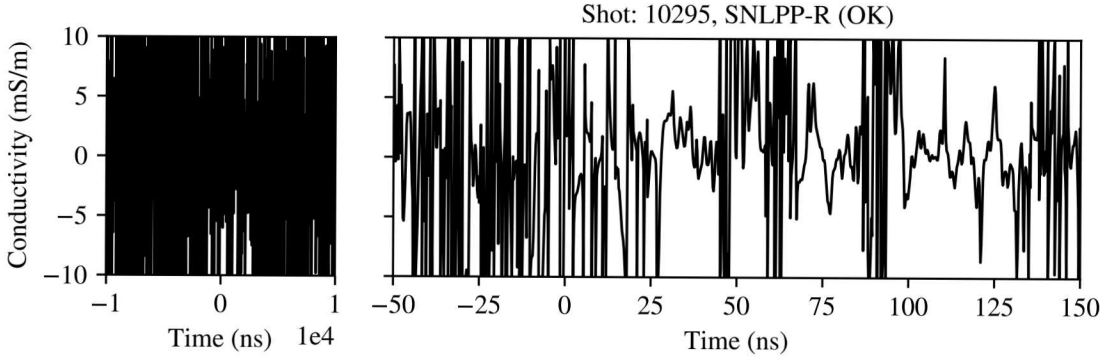
Shot: 10295, SNLPP-R (OK)
Conductivity (mS/m)
10
5
0
−5
−10
−1
0
1
Time (ns)
1e4
−50
−25
0
25
50
75
100
125
150
Time (ns)

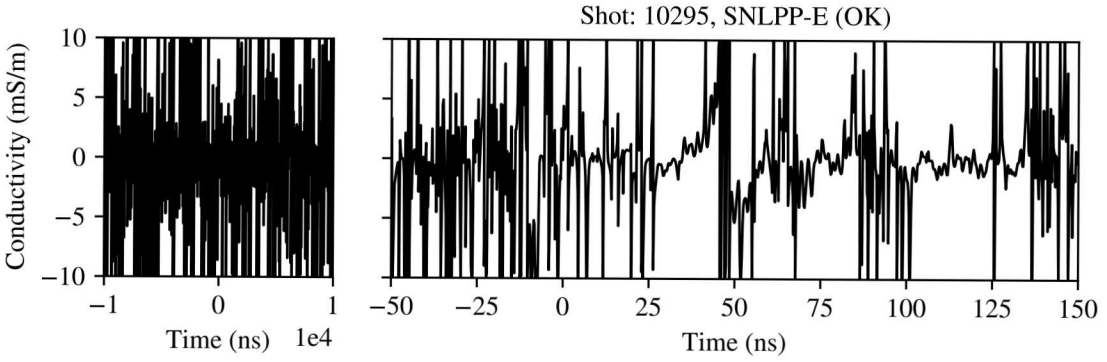
Shot: 10295, SNLPP-E (OK)
Conductivity (mS/m)
10
5
0
−5
−10
−1
0
1
Time (ns)
1e4
−50
−25
0
25
50
75
100
125
150
Time (ns)

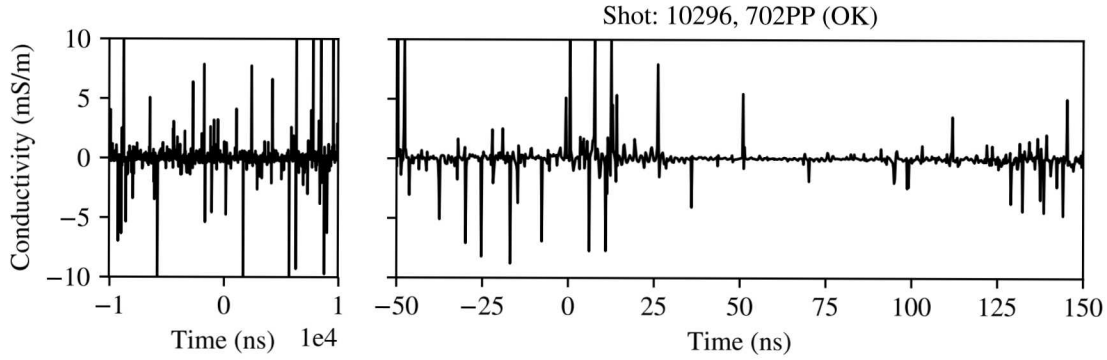
Shot: 10296, 702PP (OK)
Conductivity (mS/m)
10
5
0
−5
−10
−1
0
1
Time (ns)
1e4
−50
−25
0
25
50
75
100
125
150
Time (ns)

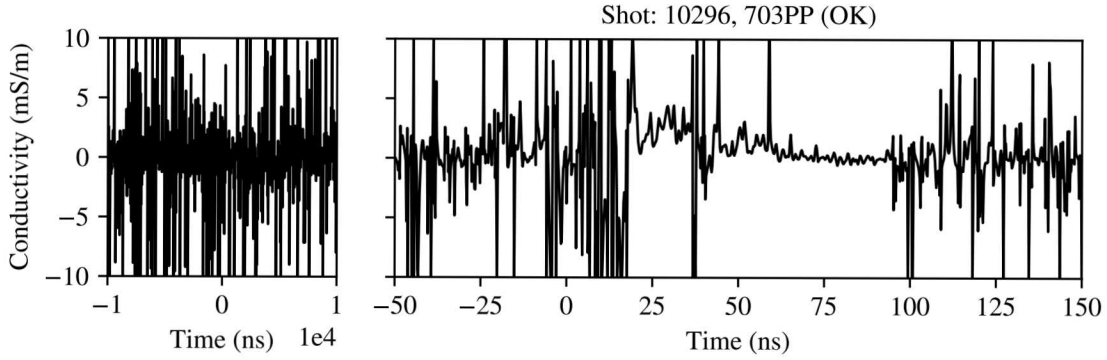
Shot: 10296, 703PP (OK)
Conductivity (mS/m)
10
5
0
−5
−10
−1
0
1
Time (ns)
1e4
−50
−25
0
25
50
75
100
125
150
Time (ns)

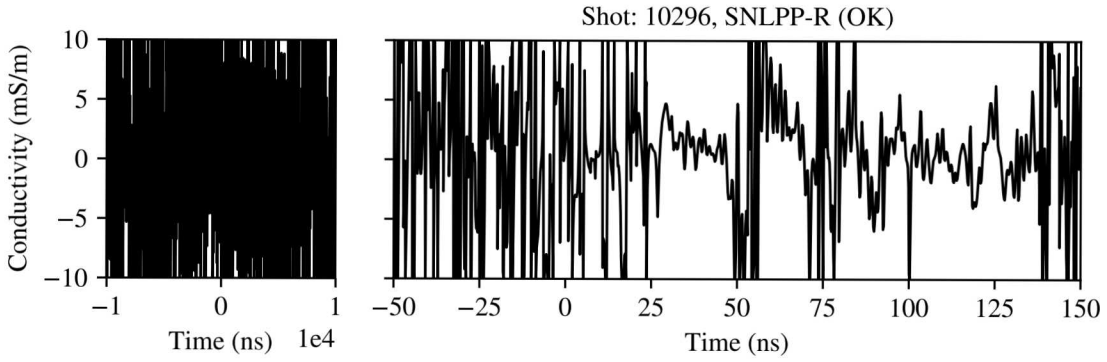
Shot: 10296, SNLPP-R (OK)
Conductivity (mS/m)
10
5
0
−5
−10
−1
0
1
Time (ns)
1e4
−50
−25
0
25
50
75
100
125
150
Time (ns)

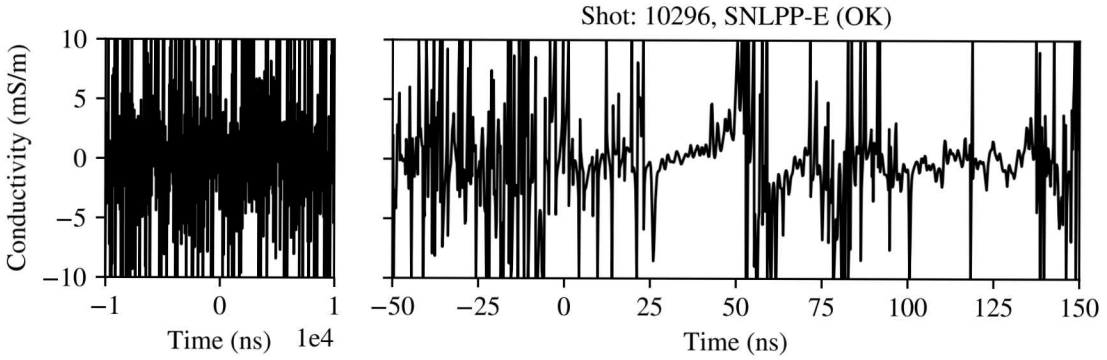
Shot: 10296, SNLPP-E (OK)
Conductivity (mS/m)
10
5
0
−5
−10
−1
0
1
Time (ns)
1e4
−50
−25
0
25
50
75
100
125
150
Time (ns)

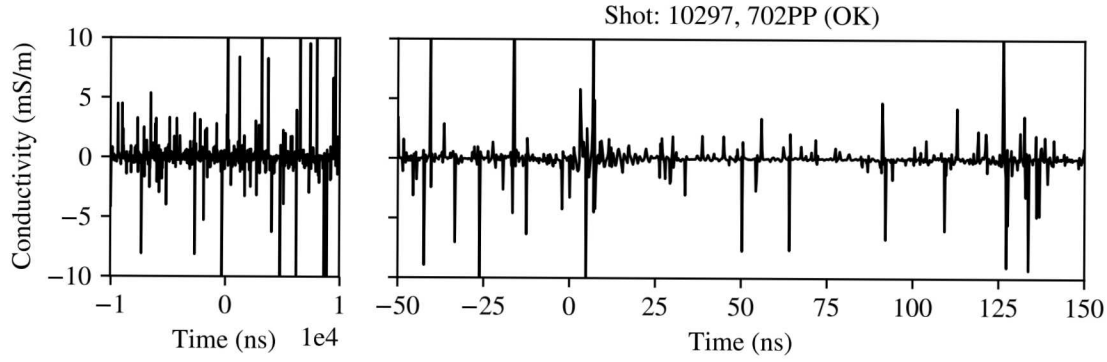
Shot: 10297, 702PP (OK)
Conductivity (mS/m)
10
5
0
−5
−10
−1
0
1
Time (ns)
1e4
−50
−25
0
25
50
75
100
125
150
Time (ns)

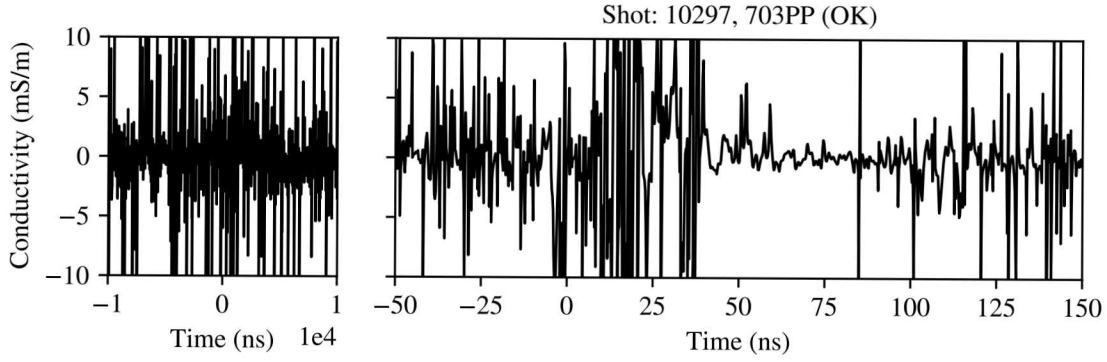
Shot: 10297, 703PP (OK)
Conductivity (mS/m)
10
5
0
−5
−10
−1
0
1
Time (ns)
1e4
−50
−25
0
25
50
75
100
125
150
Time (ns)

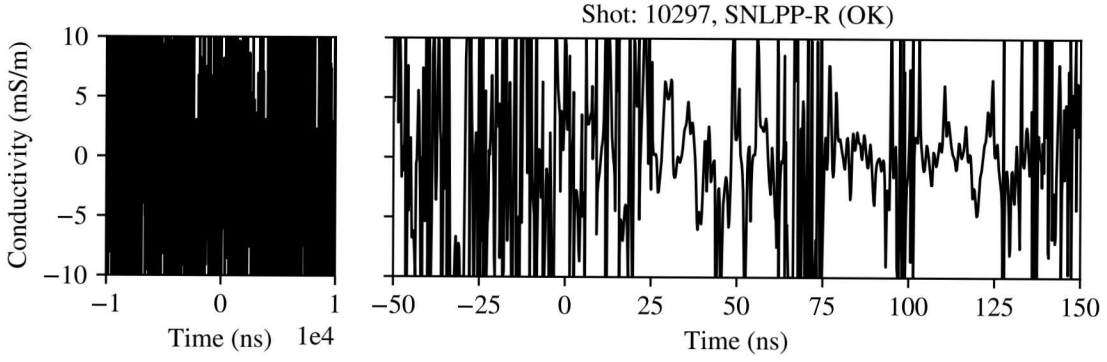
Shot: 10297, SNLPP-R (OK)
Conductivity (mS/m)
10
5
0
−5
−10
−1
0
1
Time (ns)
1e4
−50
−25
0
25
50
75
100
125
150
Time (ns)

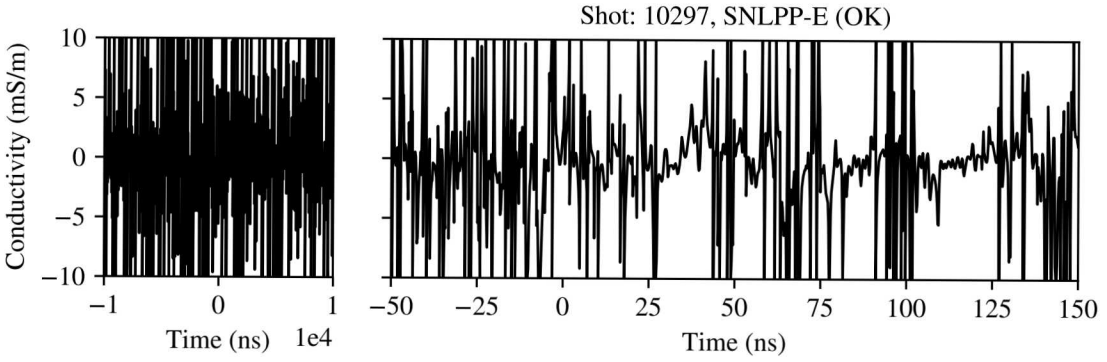
Shot: 10297, SNLPP-E (OK)
Conductivity (mS/m)
10
5
0
−5
−10
−1
0
1
Time (ns)
1e4
−50
−25
0
25
50
75
100
125
150
Time (ns)

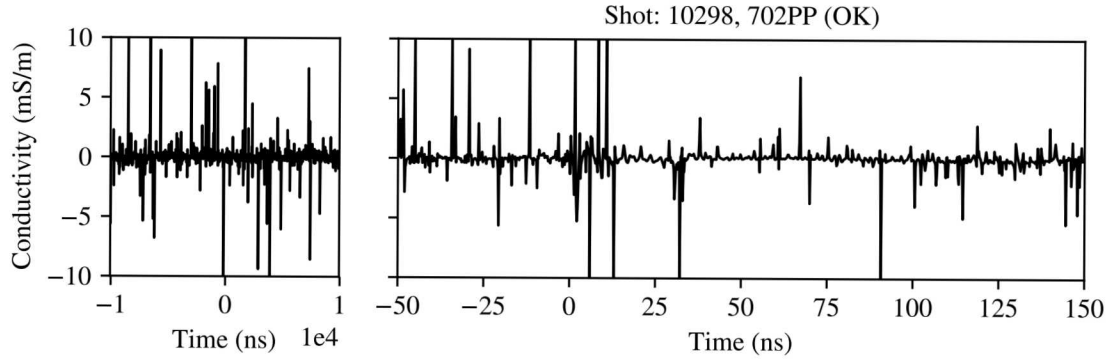
Shot: 10298, 702PP (OK)
Conductivity (mS/m)
10
5
0
−5
−10
−1
0
1
Time (ns)
1e4
−50
−25
0
25
50
75
100
125
150
Time (ns)

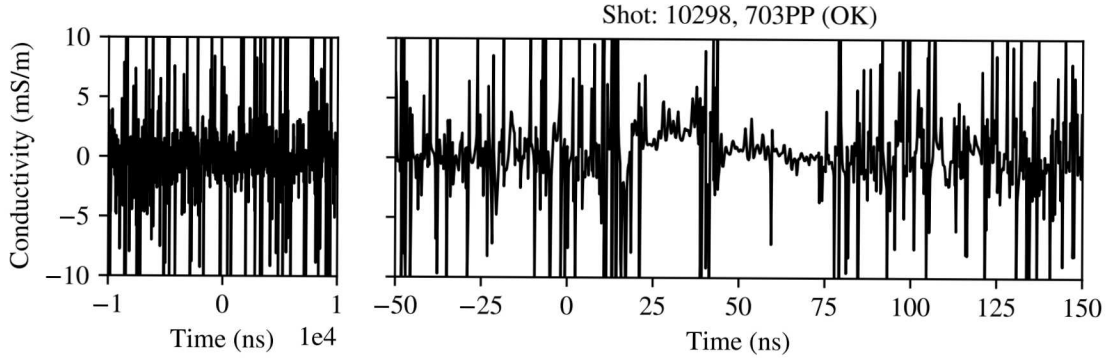
Shot: 10298, 703PP (OK)
Conductivity (mS/m)
10
5
0
−5
−10
−1
0
1
Time (ns)
1e4
−50
−25
0
25
50
75
100
125
150
Time (ns)

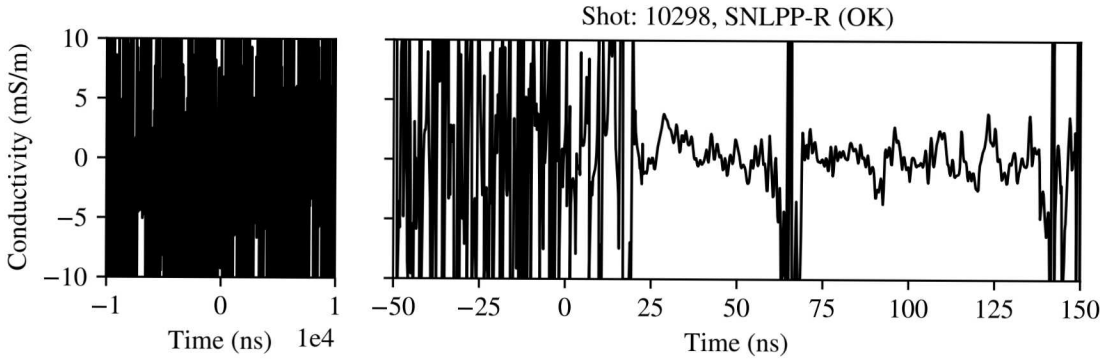
Shot: 10298, SNLPP-R (OK)
Conductivity (mS/m)
10
5
0
−5
−10
−1
0
1
Time (ns)
1e4
−50
−25
0
25
50
75
100
125
150
Time (ns)

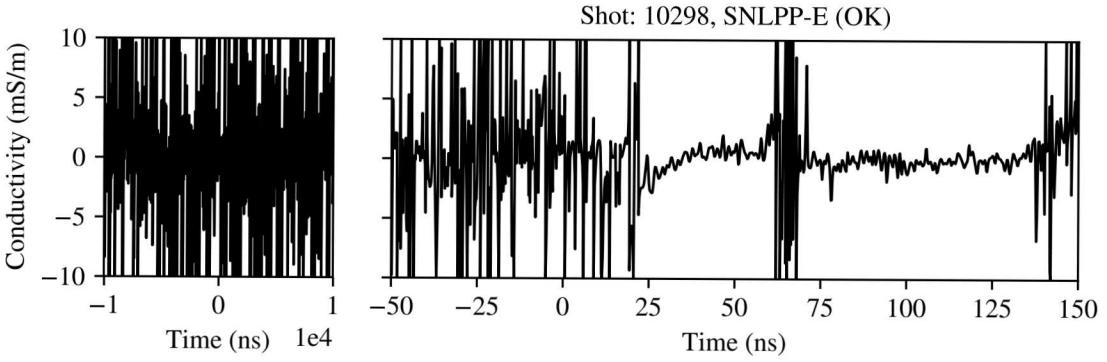
Shot: 10298, SNLPP-E (OK)
Conductivity (mS/m)
10
5
0
−5
−10
−1
0
1
Time (ns)
1e4
−50
−25
0
25
50
75
100
125
150
Time (ns)

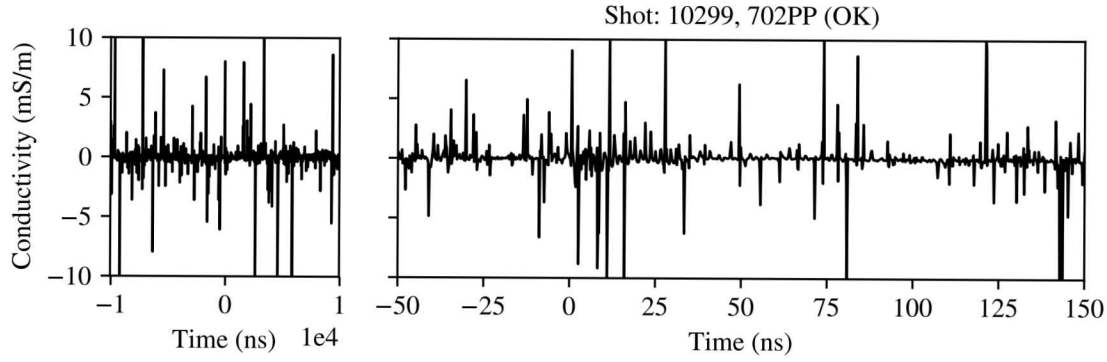
Shot: 10299, 702PP (OK)
Conductivity (mS/m)
10
5
0
−5
−10
−1
0
1
Time (ns)
1e4
−50
−25
0
25
50
75
100
125
150
Time (ns)

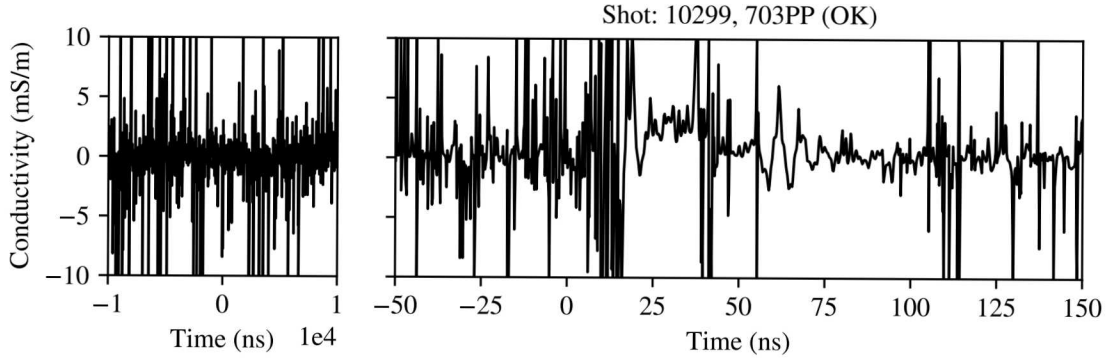
Shot: 10299, 703PP (OK)
Conductivity (mS/m)
10
5
0
−5
−10
−1
0
1
Time (ns)
1e4
−50
−25
0
25
50
75
100
125
150
Time (ns)

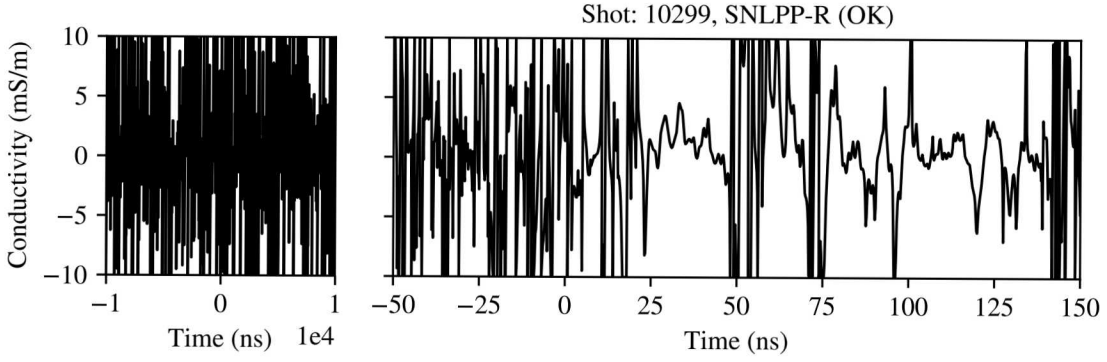
Shot: 10299, SNLPP-R (OK)
Conductivity (mS/m)
10
5
0
−5
−10
−1
0
1
Time (ns)
1e4
−50
−25
0
25
50
75
100
125
150
Time (ns)

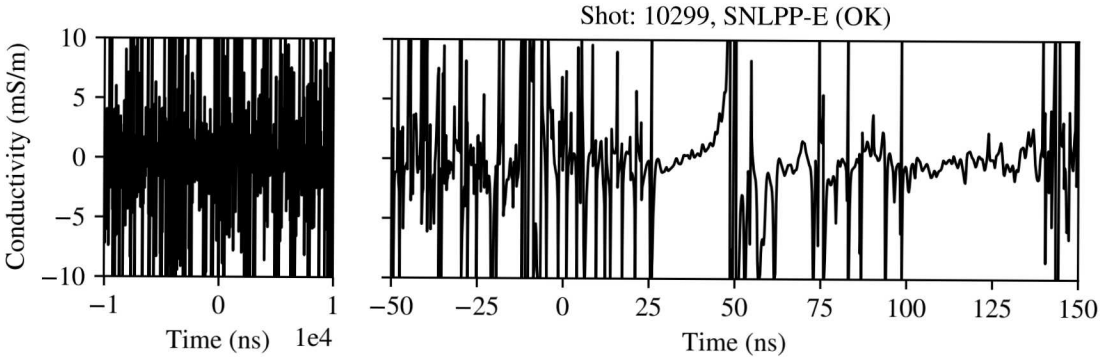
Shot: 10299, SNLPP-E (OK)
Conductivity (mS/m)
10
5
0
−5
−10
−1
0
1
Time (ns)
1e4
−50
−25
0
25
50
75
100
125
150
Time (ns)

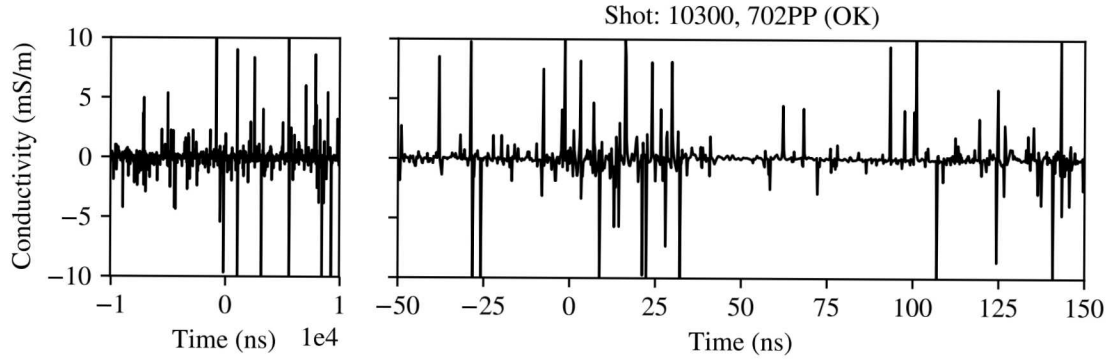
Shot: 10300, 702PP (OK)
Conductivity (mS/m)
10
5
0
−5
−10
−1
0
1
Time (ns)
1e4
−50
−25
0
25
50
75
100
125
150
Time (ns)

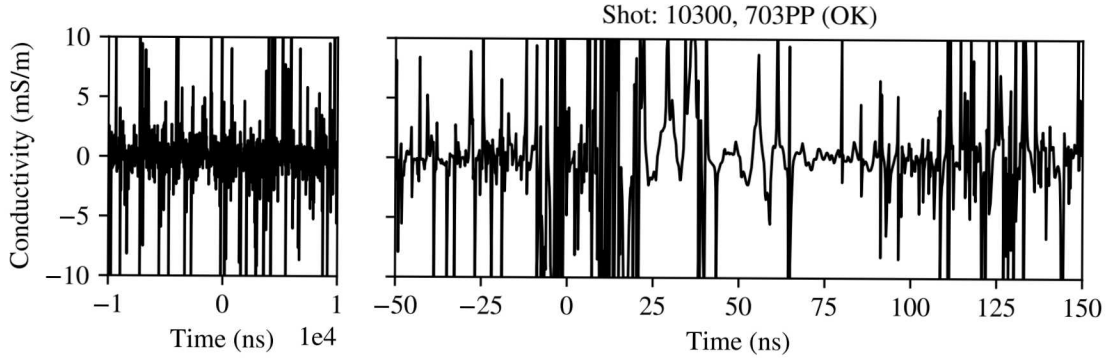
Shot: 10300, 703PP (OK)
Conductivity (mS/m)
10
5
0
−5
−10
−1
0
1
Time (ns)
1e4
−50
−25
0
25
50
75
100
125
150
Time (ns)

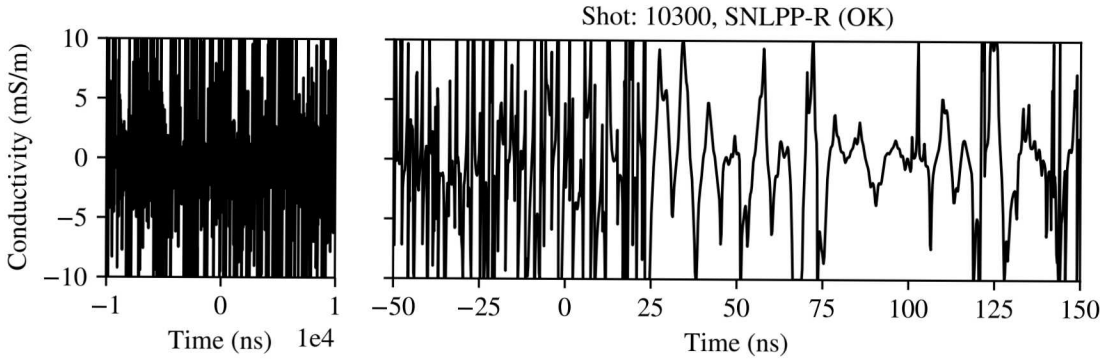
Shot: 10300, SNLPP-R (OK)
Conductivity (mS/m)
10
5
0
−5
−10
−1
0
1
Time (ns)
1e4
−50
−25
0
25
50
75
100
125
150
Time (ns)

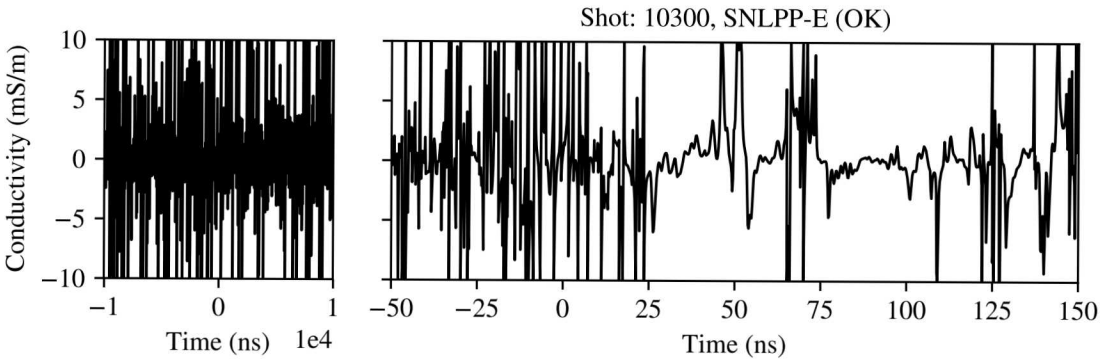
Shot: 10300, SNLPP-E (OK)
Conductivity (mS/m)
10
5
0
−5
−10
−1
0
1
Time (ns)
1e4
−50
−25
0
25
50
75
100
125
150
Time (ns)

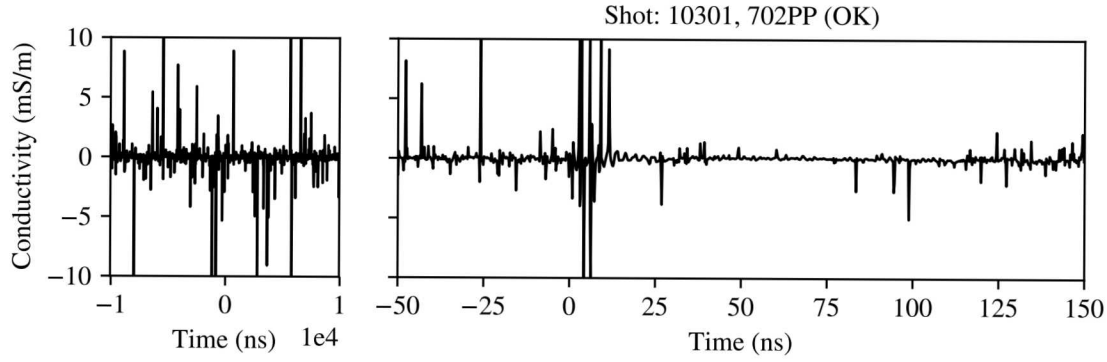
Shot: 10301, 702PP (OK)
Conductivity (mS/m)
10
5
0
−5
−10
−1
0
1
Time (ns)
1e4
−50
−25
0
25
50
75
100
125
150
Time (ns)

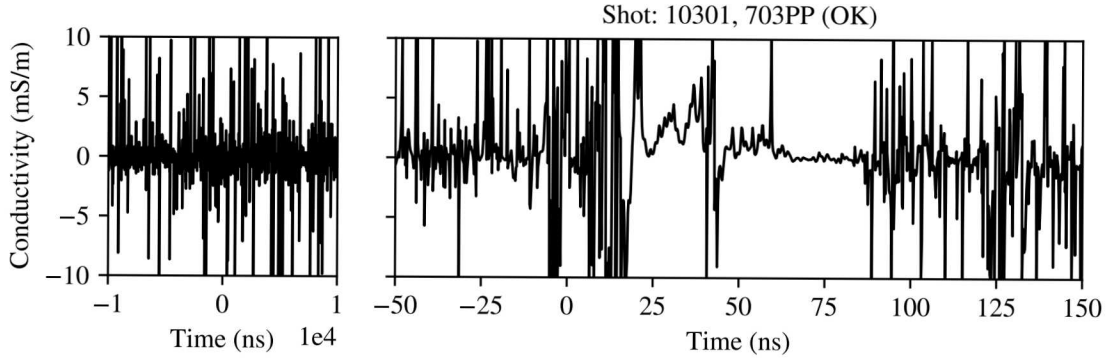
Shot: 10301, 703PP (OK)
Conductivity (mS/m)
10
5
0
−5
−10
−1
0
1
Time (ns)
1e4
−50
−25
0
25
50
75
100
125
150
Time (ns)

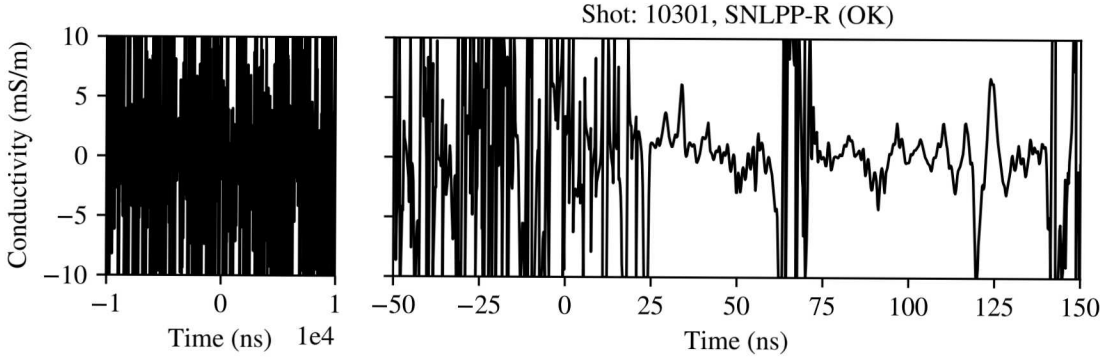
Shot: 10301, SNLPP-R (OK)
Conductivity (mS/m)
10
5
0
−5
−10
−1
0
1
Time (ns)
1e4
−50
−25
0
25
50
75
100
125
150
Time (ns)

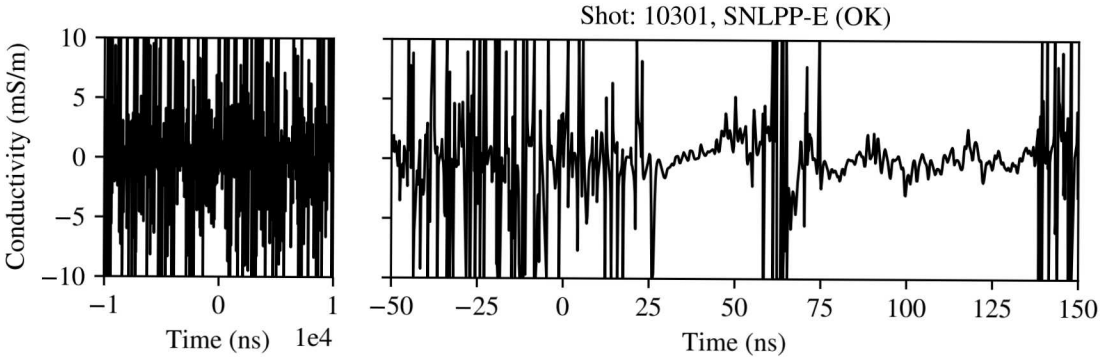
Shot: 10301, SNLPP-E (OK)
Conductivity (mS/m)
10
5
0
−5
−10
−1
0
1
Time (ns)
1e4
−50
−25
0
25
50
75
100
125
150
Time (ns)

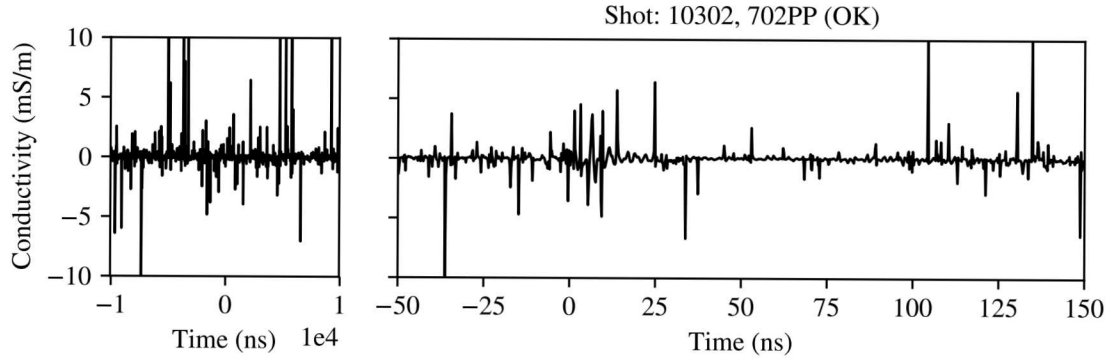
Shot: 10302, 702PP (OK)
Conductivity (mS/m)
10
5
0
−5
−10
−1
0
1
Time (ns)
1e4
−50
−25
0
25
50
75
100
125
150
Time (ns)

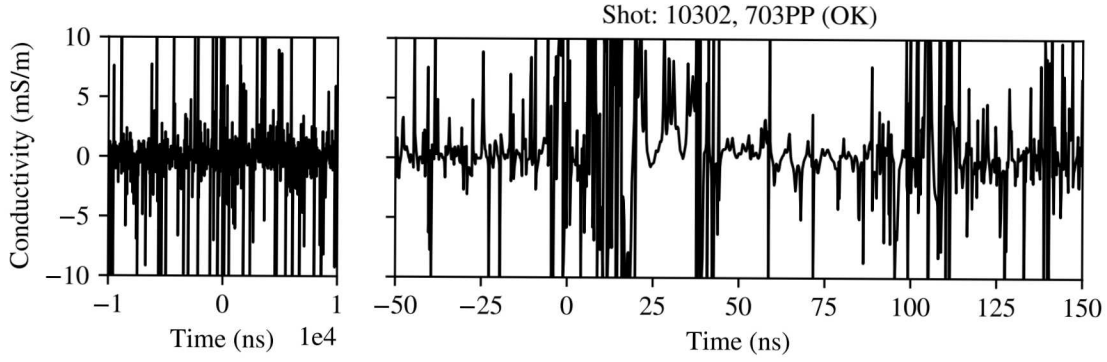
Shot: 10302, 703PP (OK)
Conductivity (mS/m)
10
5
0
−5
−10
−1
0
1
Time (ns)
1e4
−50
−25
0
25
50
75
100
125
150
Time (ns)

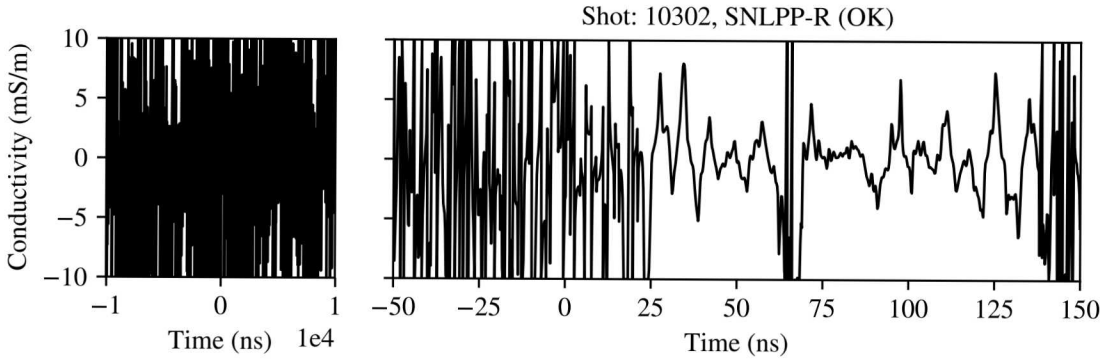
Shot: 10302, SNLPP-R (OK)
Conductivity (mS/m)
10
5
0
−5
−10
−1
0
1
Time (ns)
1e4
−50
−25
0
25
50
75
100
125
150
Time (ns)

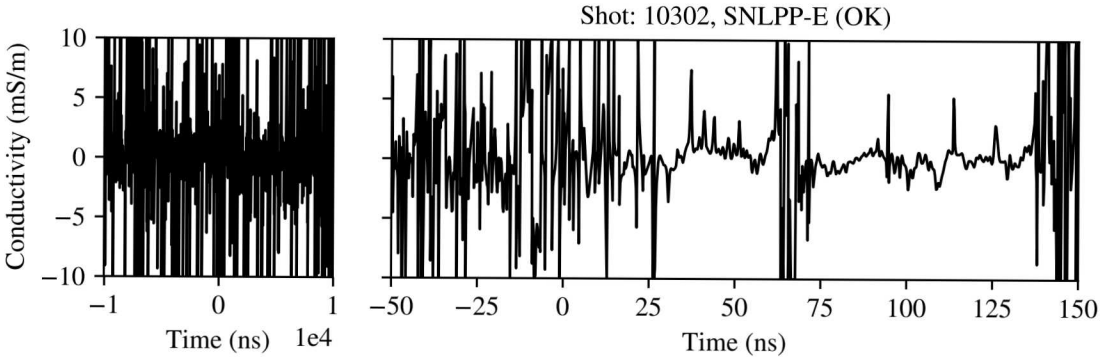
Shot: 10302, SNLPP-E (OK)
Conductivity (mS/m)
10
5
0
−5
−10
−1
0
1
Time (ns)
1e4
−50
−25
0
25
50
75
100
125
150
Time (ns)

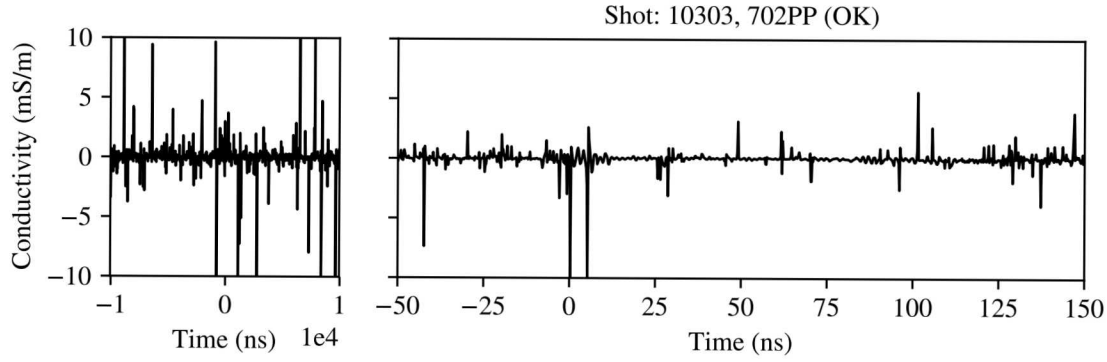
Shot: 10303, 702PP (OK)
Conductivity (mS/m)
10
5
0
−5
−10
−1
0
1
Time (ns)
1e4
−50
−25
0
25
50
75
100
125
150
Time (ns)

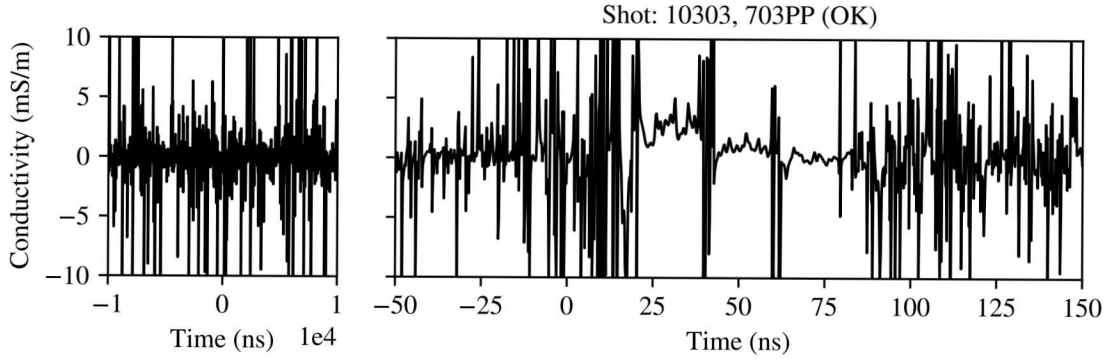
Shot: 10303, 703PP (OK)
Conductivity (mS/m)
10
5
0
−5
−10
−1
0
1
Time (ns)
1e4
−50
−25
0
25
50
75
100
125
150
Time (ns)

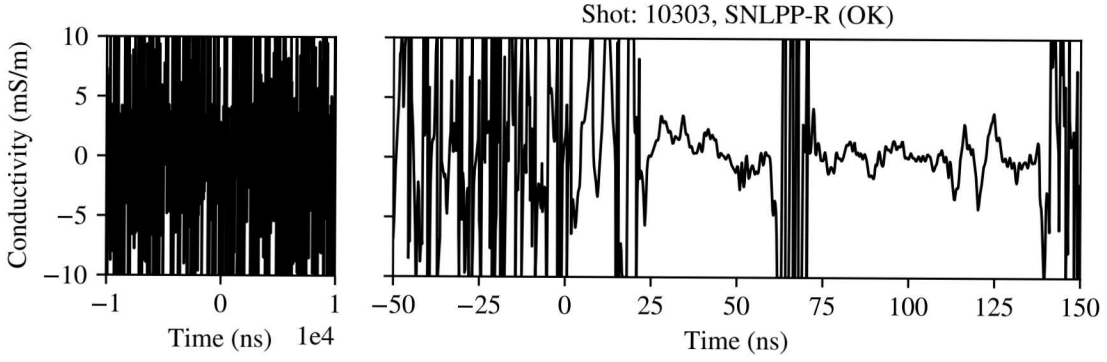
Shot: 10303, SNLPP-R (OK)
Conductivity (mS/m)
10
5
0
−5
−10
−1
0
1
Time (ns)
1e4
−50
−25
0
25
50
75
100
125
150
Time (ns)

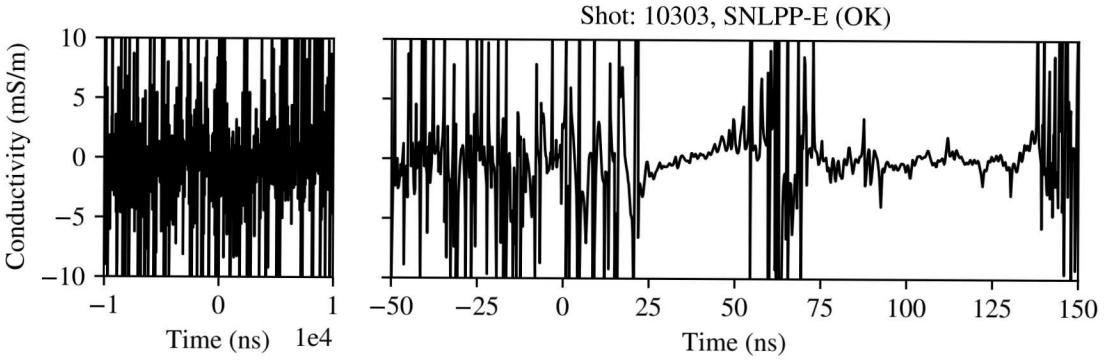
Shot: 10303, SNLPP-E (OK)
Conductivity (mS/m)
10
5
0
−5
−10
−1
0
1
Time (ns)
1e4
−50
−25
0
25
50
75
100
125
150
Time (ns)

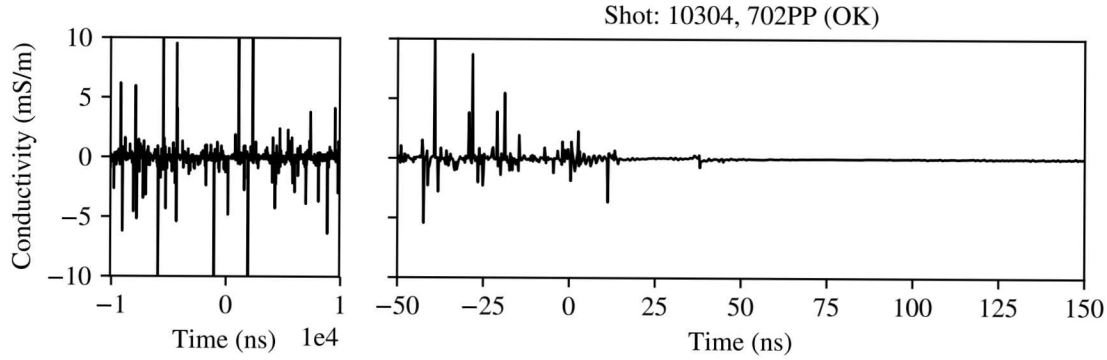
Shot: 10304, 702PP (OK)
Conductivity (mS/m)
10
5
0
−5
−10
−1
0
1
Time (ns)
1e4
−50
−25
0
25
50
75
100
125
150
Time (ns)

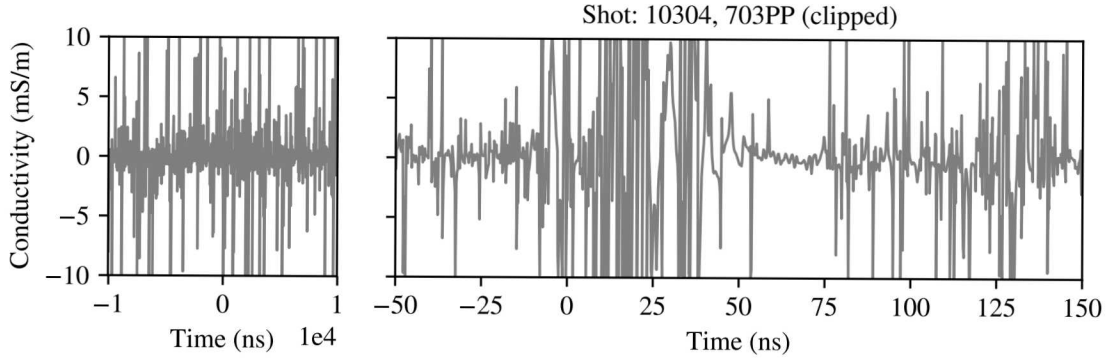
Shot: 10304, 703PP (clipped)
Conductivity (mS/m)
10
5
0
−5
−10
−1
0
1
Time (ns)
1e4
−50
−25
0
25
50
75
100
125
150
Time (ns)

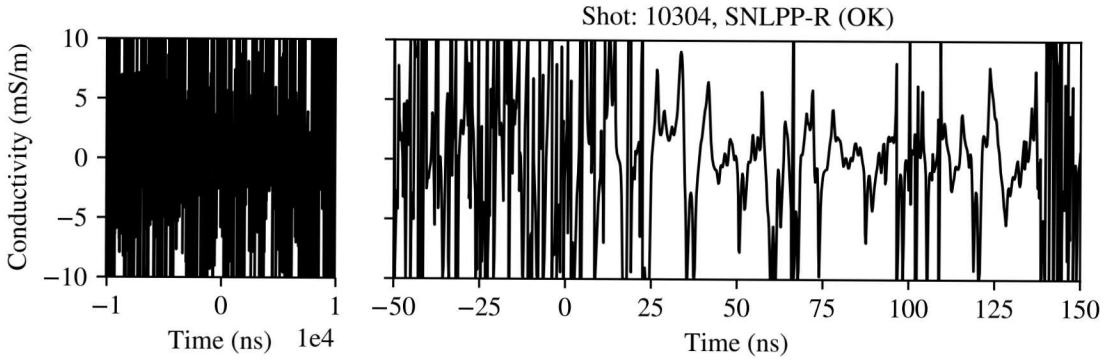
Shot: 10304, SNLPP-R (OK)
Conductivity (mS/m)
10
5
0
−5
−10
−1
0
1
Time (ns)
1e4
−50
−25
0
25
50
75
100
125
150
Time (ns)

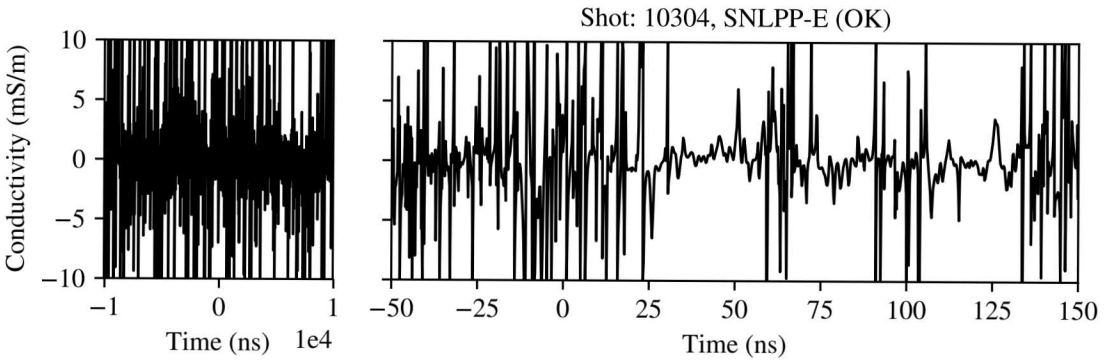
Shot: 10304, SNLPP-E (OK)
Conductivity (mS/m)
10
5
0
−5
−10
−1
0
1
Time (ns)
1e4
−50
−25
0
25
50
75
100
125
150
Time (ns)

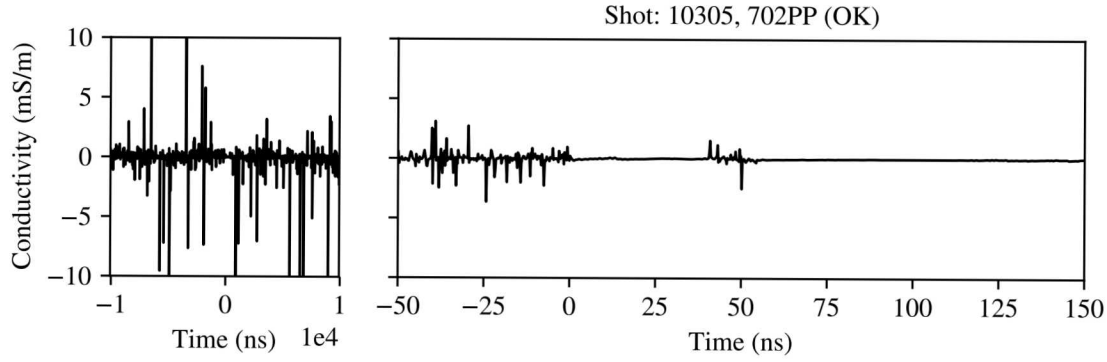
Shot: 10305, 702PP (OK)
Conductivity (mS/m)
10
5
0
−5
−10
−1
0
1
Time (ns)
1e4
−50
−25
0
25
50
75
100
125
150
Time (ns)

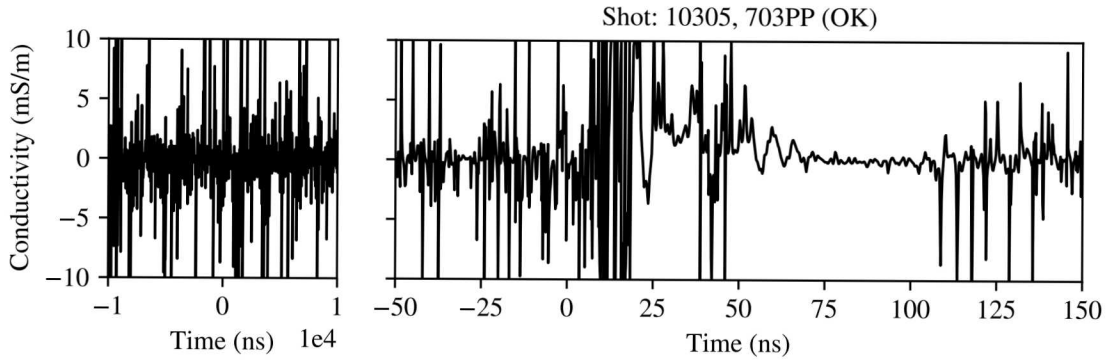
Shot: 10305, 703PP (OK)
Conductivity (mS/m)
10
5
0
−5
−10
−1
0
1
Time (ns)
1e4
−50
−25
0
25
50
75
100
125
150
Time (ns)

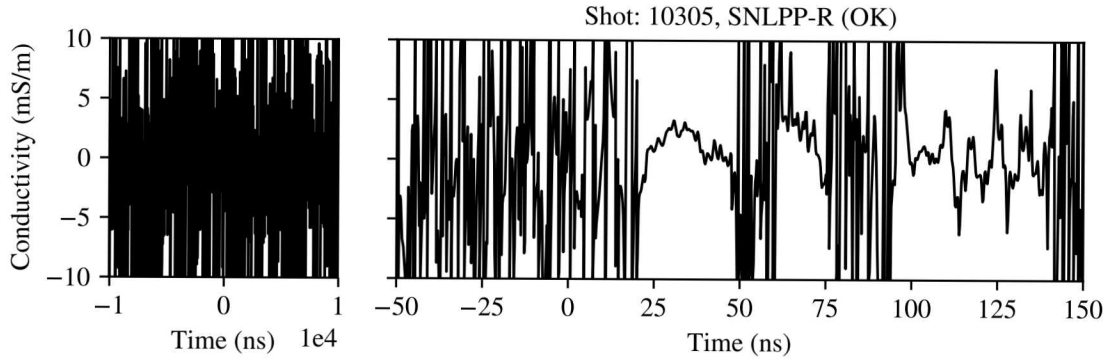
Shot: 10305, SNLPP-R (OK)
Conductivity (mS/m)
10
5
0
−5
−10
−1
0
1
Time (ns)
1e4
−50
−25
0
25
50
75
100
125
150
Time (ns)

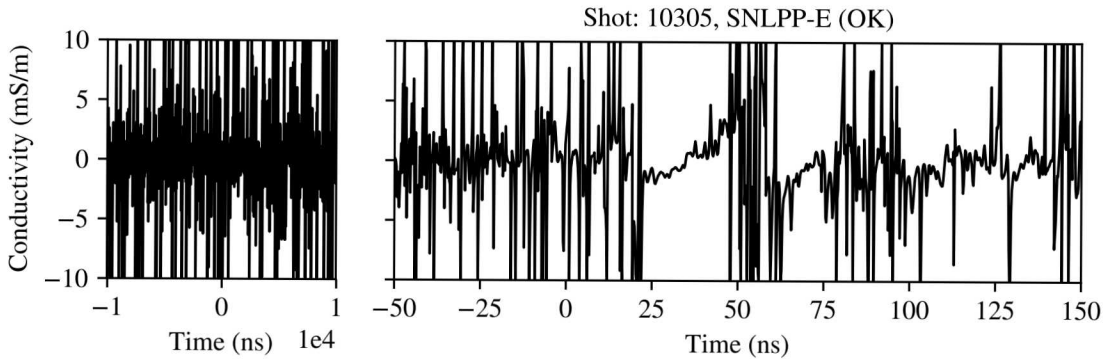
Shot: 10305, SNLPP-E (OK)
Conductivity (mS/m)
10
5
0
−5
−10
−1
0
1
Time (ns)
1e4
−50
−25
0
25
50
75
100
125
150
Time (ns)

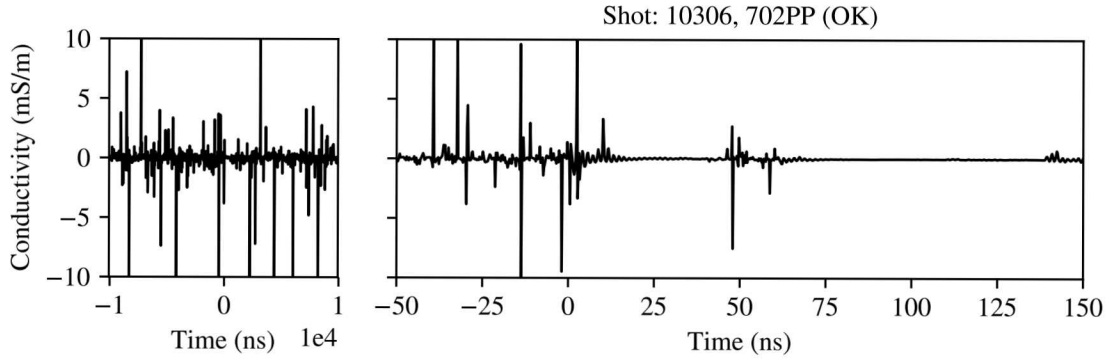
Shot: 10306, 702PP (OK)
Conductivity (mS/m)
10
5
0
−5
−10
−1
0
1
Time (ns)
1e4
−50
−25
0
25
50
75
100
125
150
Time (ns)

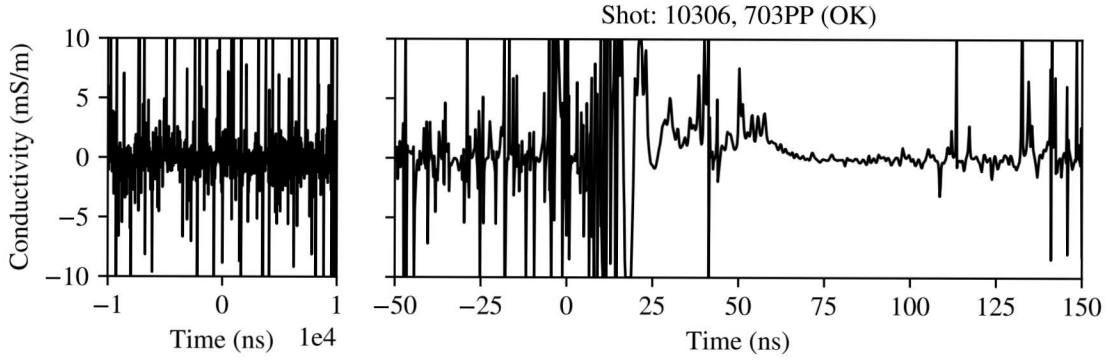
Shot: 10306, 703PP (OK)
Conductivity (mS/m)
10
5
0
−5
−10
−1
0
1
Time (ns)
1e4
−50
−25
0
25
50
75
100
125
150
Time (ns)

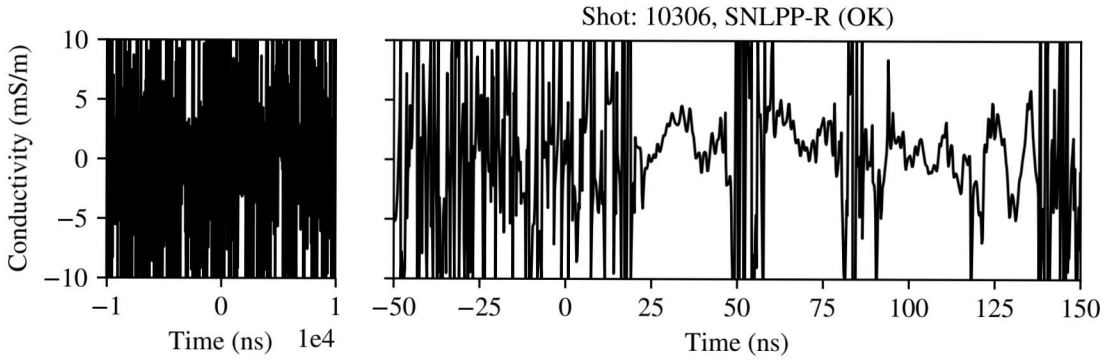
Shot: 10306, SNLPP-R (OK)
Conductivity (mS/m)
10
5
0
−5
−10
−1
0
1
Time (ns)
1e4
−50
−25
0
25
50
75
100
125
150
Time (ns)

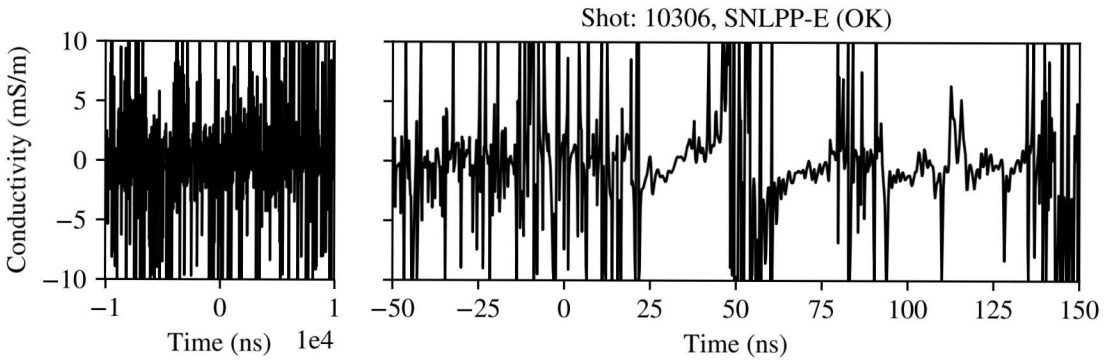
Shot: 10306, SNLPP-E (OK)
Conductivity (mS/m)
10
5
0
−5
−10
−1
0
1
Time (ns)
1e4
−50
−25
0
25
50
75
100
125
150
Time (ns)

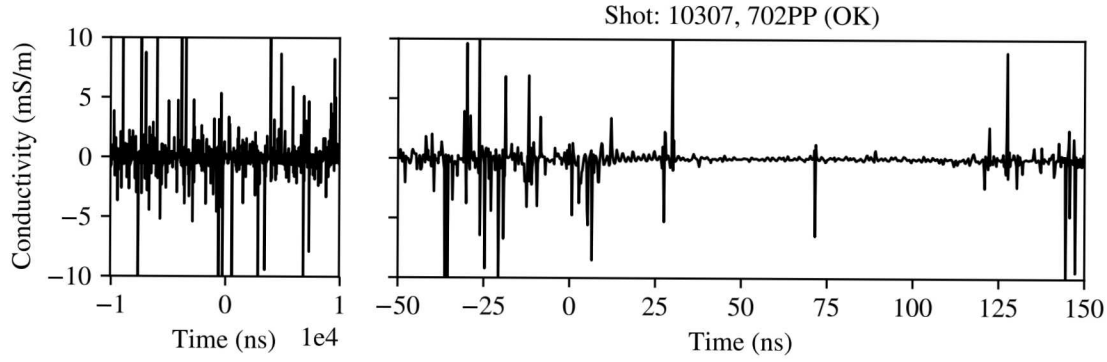
Shot: 10307, 702PP (OK)
Conductivity (mS/m)
10
5
0
−5
−10
−1
0
1
Time (ns)
1e4
−50
−25
0
25
50
75
100
125
150
Time (ns)

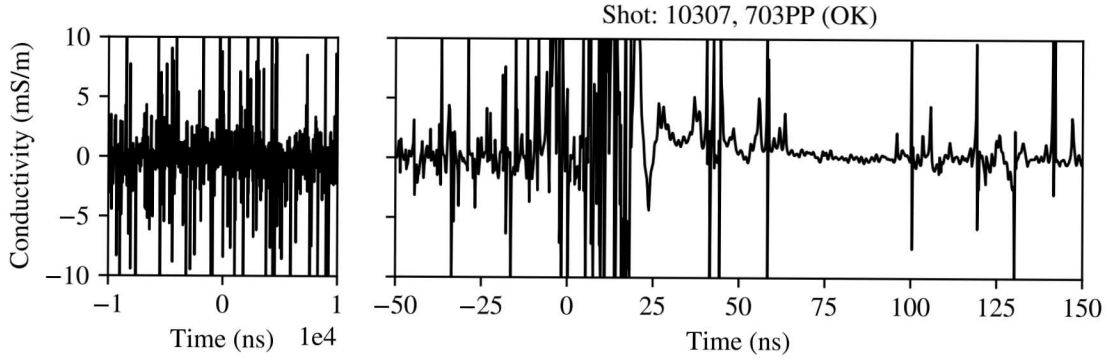
Shot: 10307, 703PP (OK)
Conductivity (mS/m)
10
5
0
−5
−10
−1
0
1
Time (ns)
1e4
−50
−25
0
25
50
75
100
125
150
Time (ns)

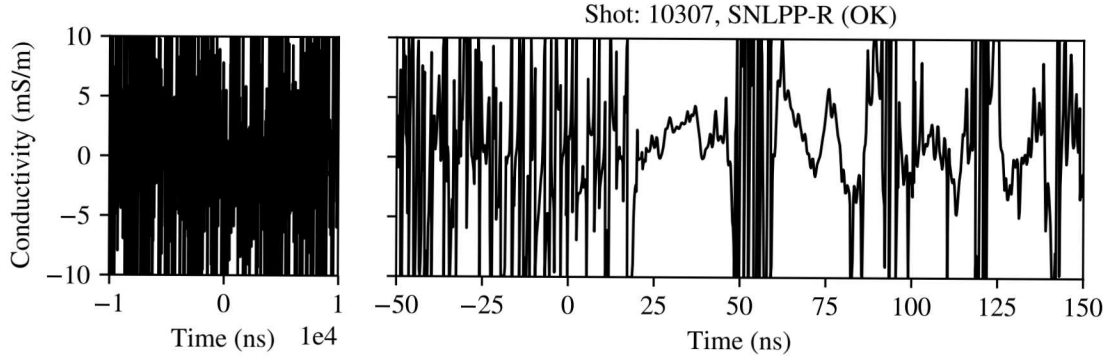
Shot: 10307, SNLPP-R (OK)
Conductivity (mS/m)
10
5
0
−5
−10
−1
0
1
Time (ns)
1e4
−50
−25
0
25
50
75
100
125
150
Time (ns)

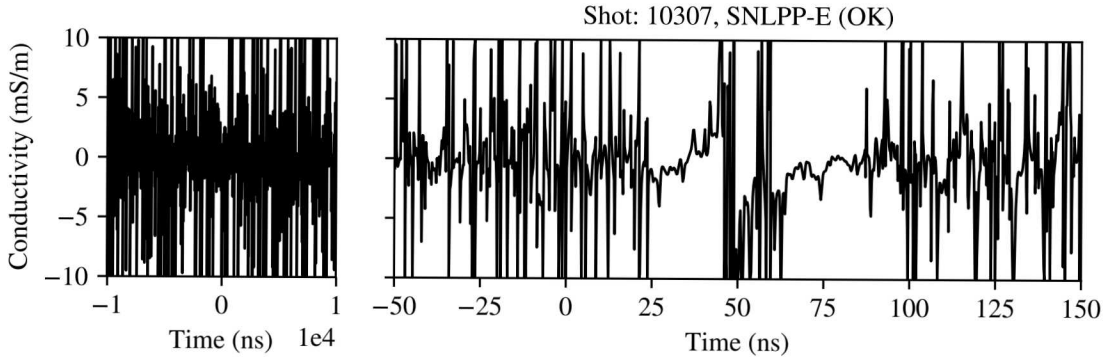
Shot: 10307, SNLPP-E (OK)
Conductivity (mS/m)
10
5
0
−5
−10
−1
0
1
Time (ns)
1e4
−50
−25
0
25
50
75
100
125
150
Time (ns)

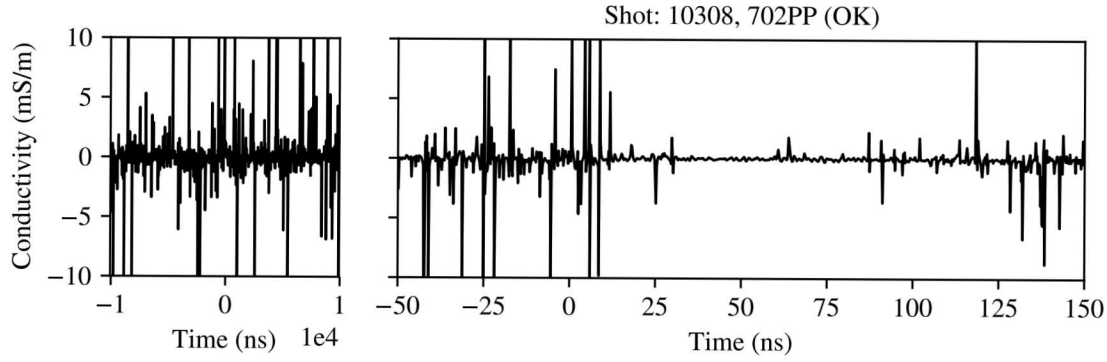
Shot: 10308, 702PP (OK)
Conductivity (mS/m)
10
5
0
−5
−10
−1
0
1
Time (ns)
1e4
−50
−25
0
25
50
75
100
125
150
Time (ns)

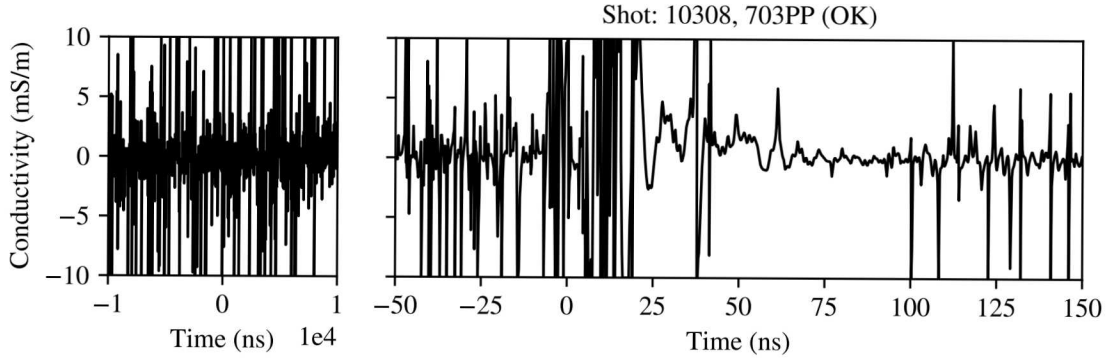
Shot: 10308, 703PP (OK)
Conductivity (mS/m)
10
5
0
−5
−10
−1
0
1
Time (ns)
1e4
−50
−25
0
25
50
75
100
125
150
Time (ns)

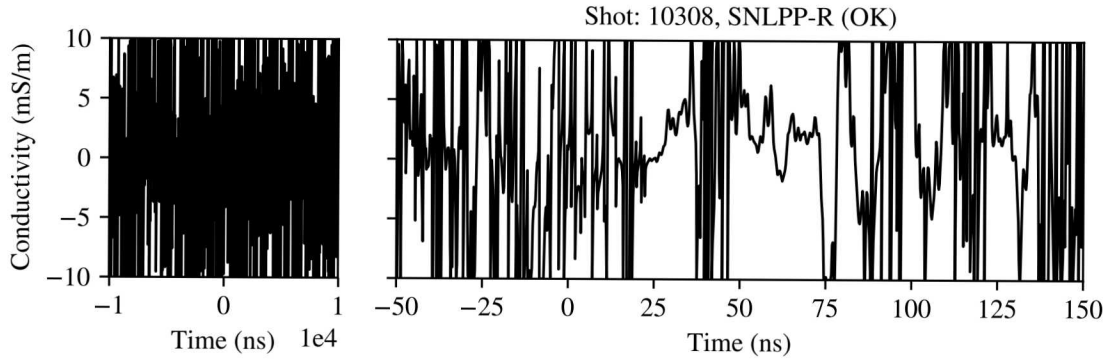
Shot: 10308, SNLPP-R (OK)
Conductivity (mS/m)
10
5
0
−5
−10
−1
0
1
Time (ns)
1e4
−50
−25
0
25
50
75
100
125
150
Time (ns)

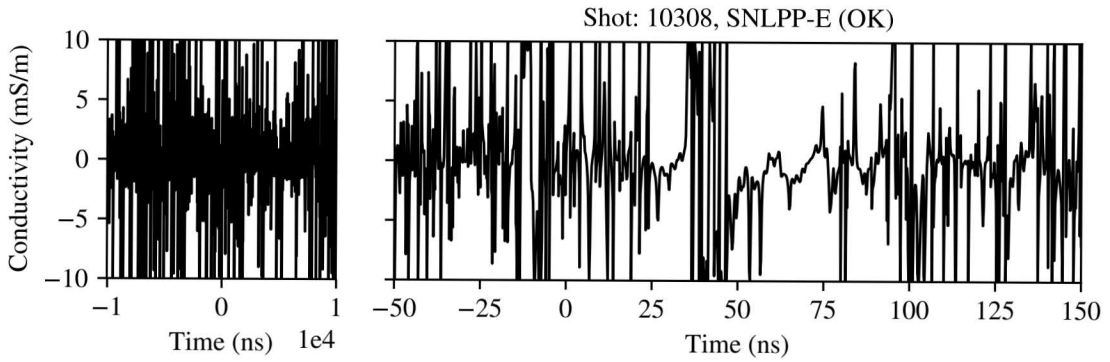
Shot: 10308, SNLPP-E (OK)
Conductivity (mS/m)
10
5
0
−5
−10
−1
0
1
Time (ns)
1e4
−50
−25
0
25
50
75
100
125
150
Time (ns)

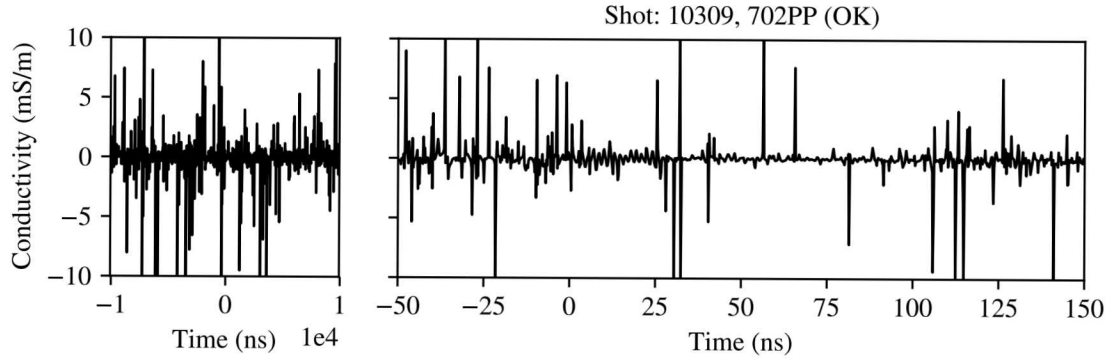
Shot: 10309, 702PP (OK)
Conductivity (mS/m)
10
5
0
−5
−10
−1
0
1
Time (ns)
1e4
−50
−25
0
25
50
75
100
125
150
Time (ns)

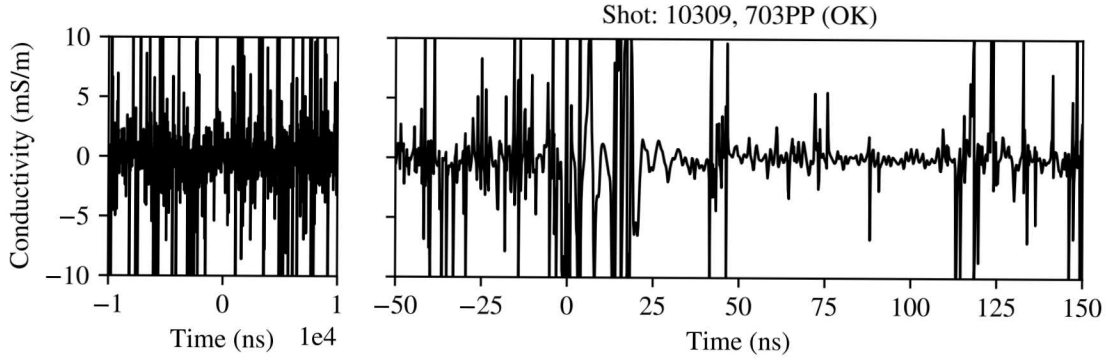
Shot: 10309, 703PP (OK)
Conductivity (mS/m)
10
5
0
−5
−10
−1
0
1
Time (ns)
1e4
−50
−25
0
25
50
75
100
125
150
Time (ns)

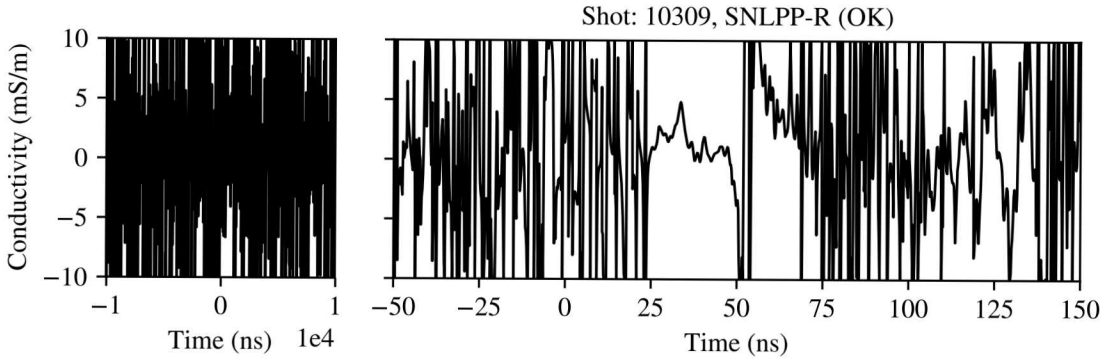
Shot: 10309, SNLPP-R (OK)
Conductivity (mS/m)
10
5
0
−5
−10
−1
0
1
Time (ns)
1e4
−50
−25
0
25
50
75
100
125
150
Time (ns)

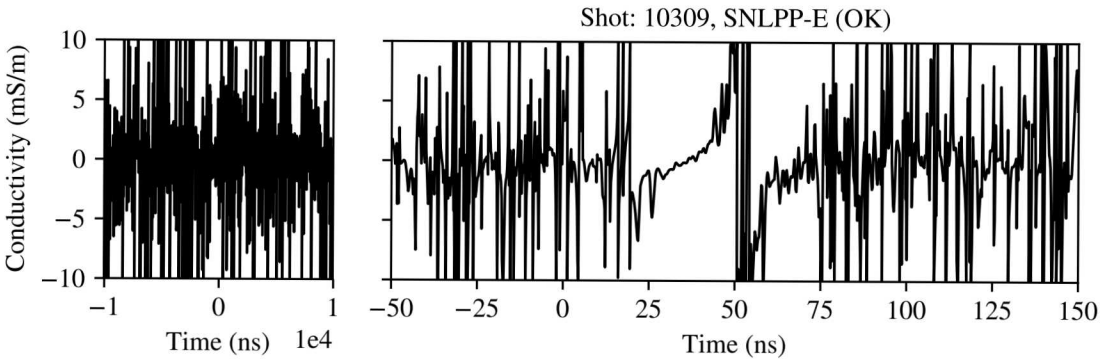
Shot: 10309, SNLPP-E (OK)
Conductivity (mS/m)
10
5
0
−5
−10
−1
0
1
Time (ns)
1e4
−50
−25
0
25
50
75
100
125
150
Time (ns)

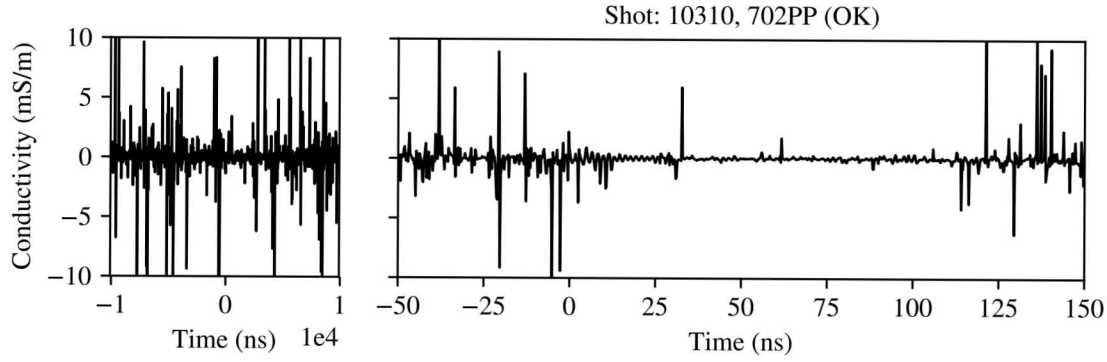
Shot: 10310, 702PP (OK)
Conductivity (mS/m)
10
5
0
−5
−10
−1
0
1
Time (ns)
1e4
−50
−25
0
25
50
75
100
125
150
Time (ns)

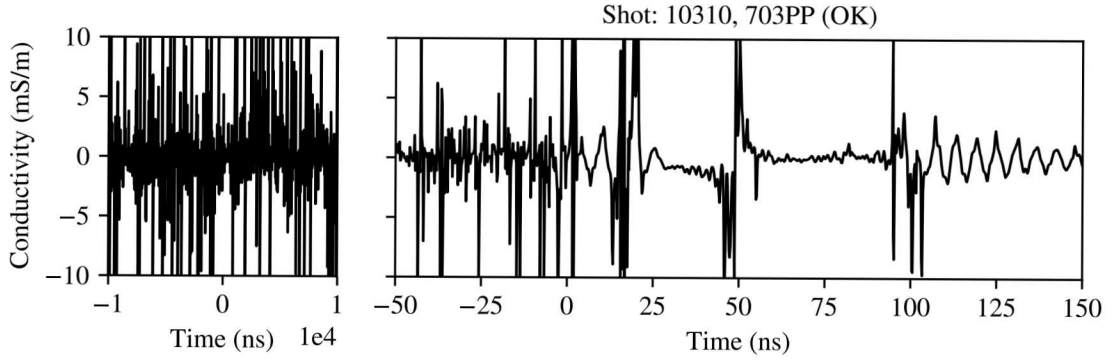
Shot: 10310, 703PP (OK)
Conductivity (mS/m)
10
5
0
−5
−10
−1
0
1
Time (ns)
1e4
−50
−25
0
25
50
75
100
125
150
Time (ns)

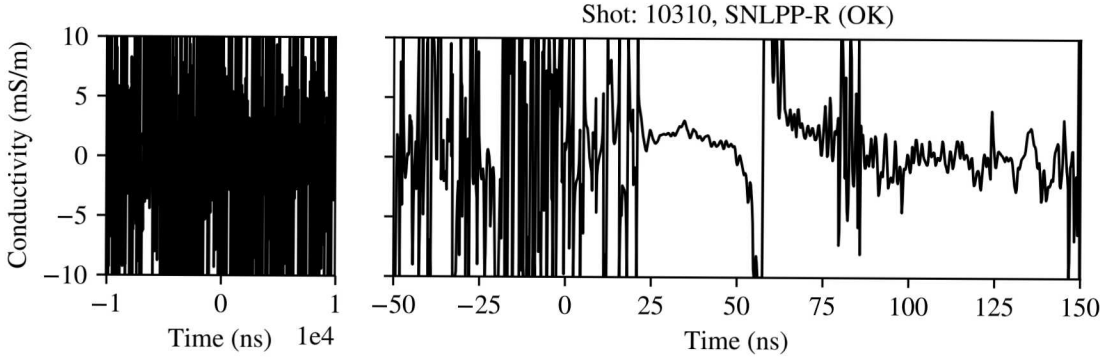
Shot: 10310, SNLPP-R (OK)
Conductivity (mS/m)
10
5
0
−5
−10
−1
0
1
Time (ns)
1e4
−50
−25
0
25
50
75
100
125
150
Time (ns)

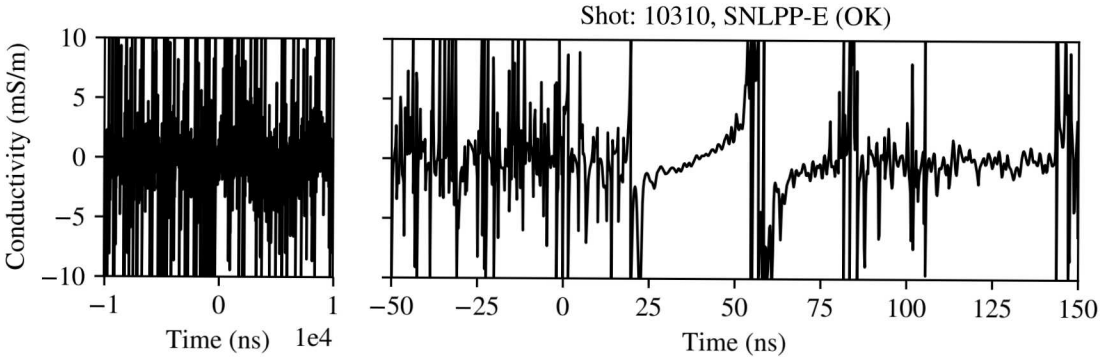
Shot: 10310, SNLPP-E (OK)
Conductivity (mS/m)
10
5
0
−5
−10
−1
0
1
Time (ns)
1e4
−50
−25
0
25
50
75
100
125
150
Time (ns)

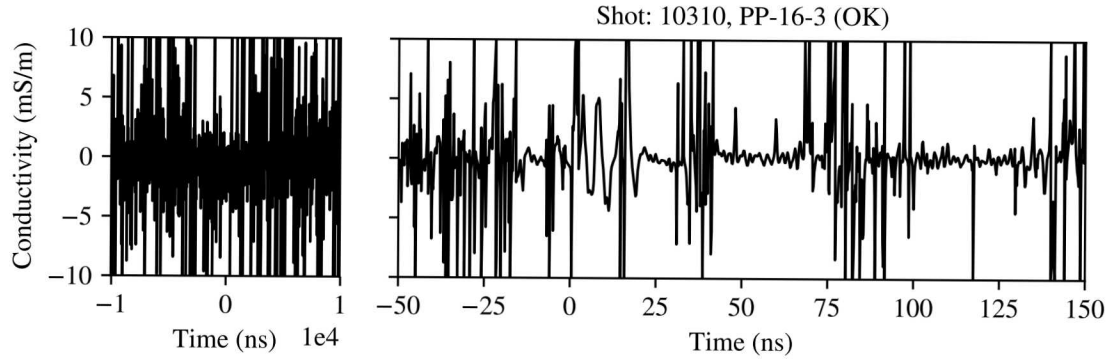
Shot: 10310, PP-16-3 (OK)
Conductivity (mS/m)
10
5
0
−5
−10
−1
0
1
Time (ns)
1e4
−50
−25
0
25
50
75
100
125
150
Time (ns)

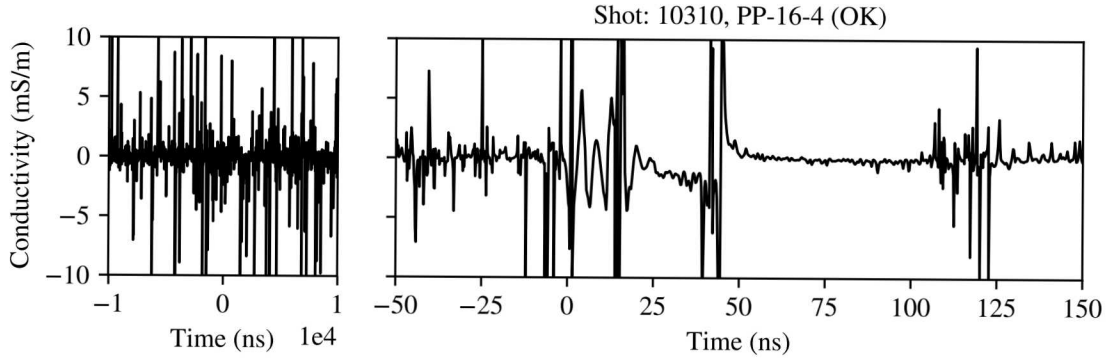
Shot: 10310, PP-16-4 (OK)
Conductivity (mS/m)
10
5
0
−5
−10
−1
0
1
Time (ns)
1e4
−50
−25
0
25
50
75
100
125
150
Time (ns)

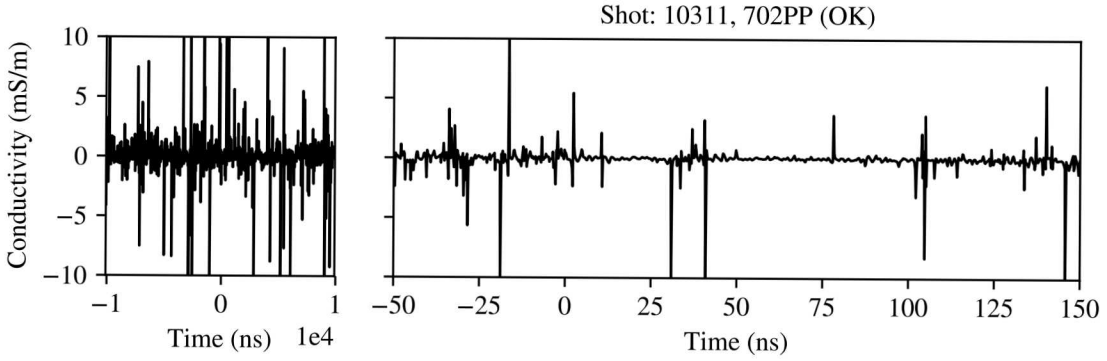
Shot: 10311, 702PP (OK)
Conductivity (mS/m)
10
5
0
−5
−10
−1
0
1
Time (ns)
1e4
−50
−25
0
25
50
75
100
125
150
Time (ns)

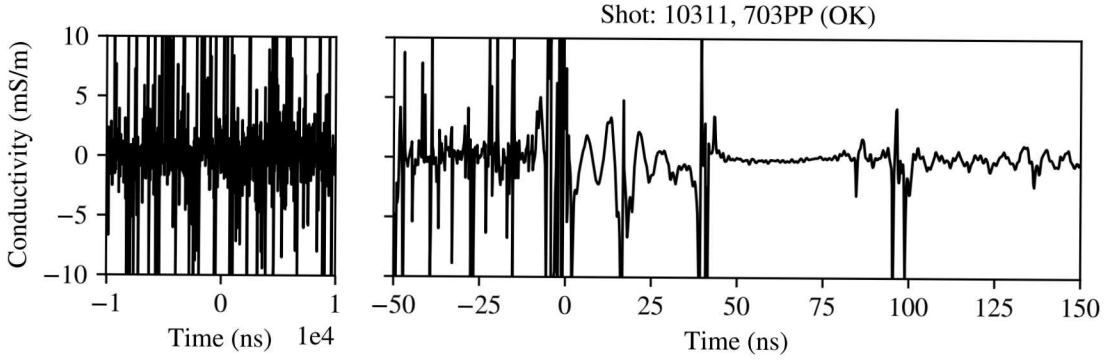
Shot: 10311, 703PP (OK)
Conductivity (mS/m)
10
5
0
−5
−10
−1
0
1
Time (ns)
1e4
−50
−25
0
25
50
75
100
125
150
Time (ns)

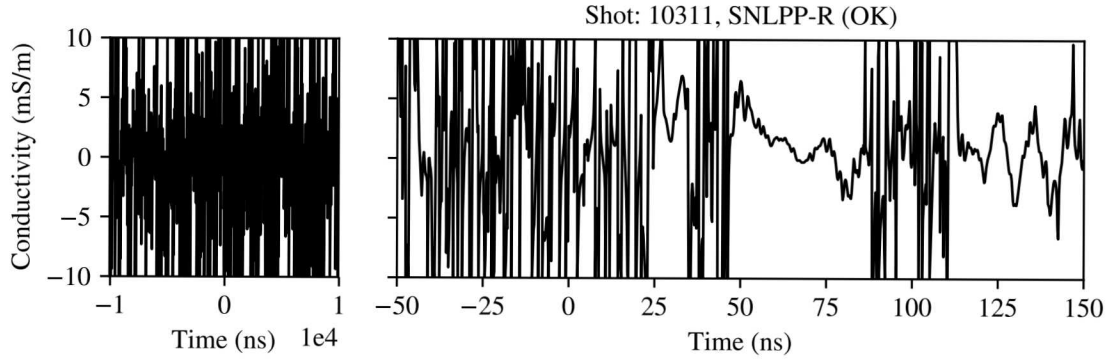
Shot: 10311, SNLPP-R (OK)
Conductivity (mS/m)
10
5
0
−5
−10
−1
0
1
Time (ns)
1e4
−50
−25
0
25
50
75
100
125
150
Time (ns)

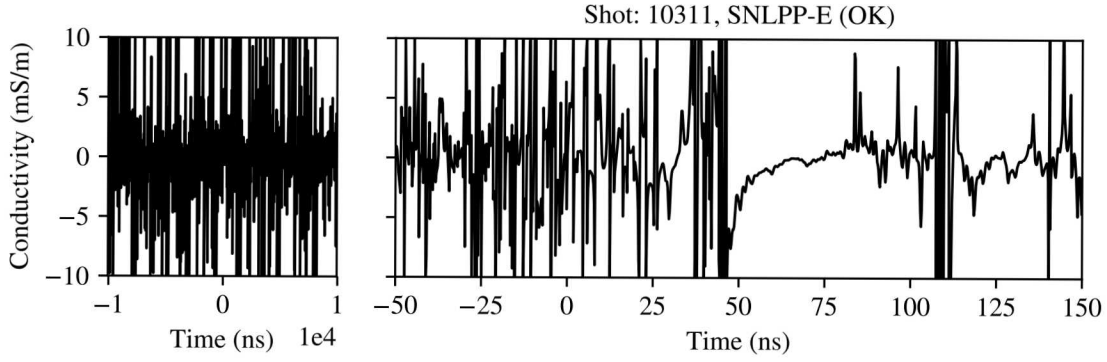
Shot: 10311, SNLPP-E (OK)
Conductivity (mS/m)
10
5
0
−5
−10
−1
0
1
Time (ns)
1e4
−50
−25
0
25
50
75
100
125
150
Time (ns)

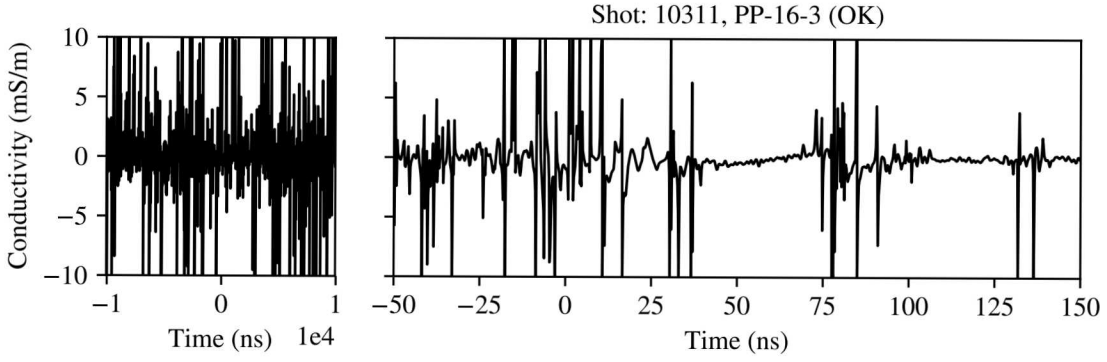
Shot: 10311, PP-16-3 (OK)
Conductivity (mS/m)
10
5
0
−5
−10
−1
0
1
Time (ns)
1e4
−50
−25
0
25
50
75
100
125
150
Time (ns)

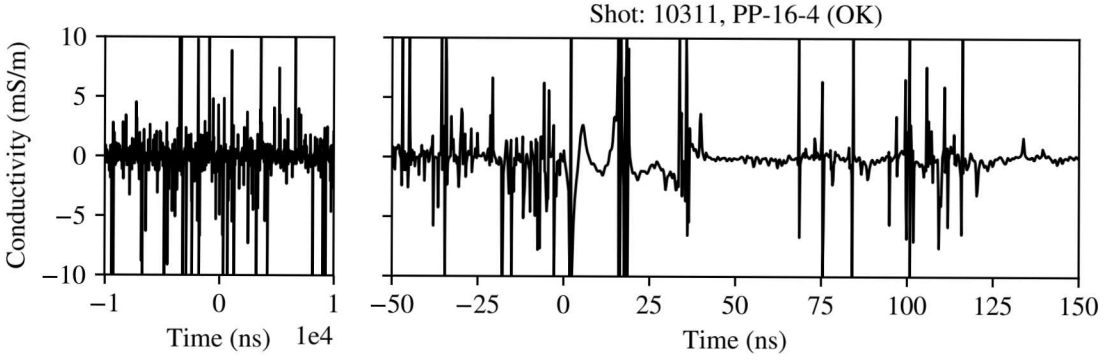
Shot: 10311, PP-16-4 (OK)
Conductivity (mS/m)
10
5
0
−5
−10
−1
0
1
Time (ns)
1e4
−50
−25
0
25
50
75
100
125
150
Time (ns)

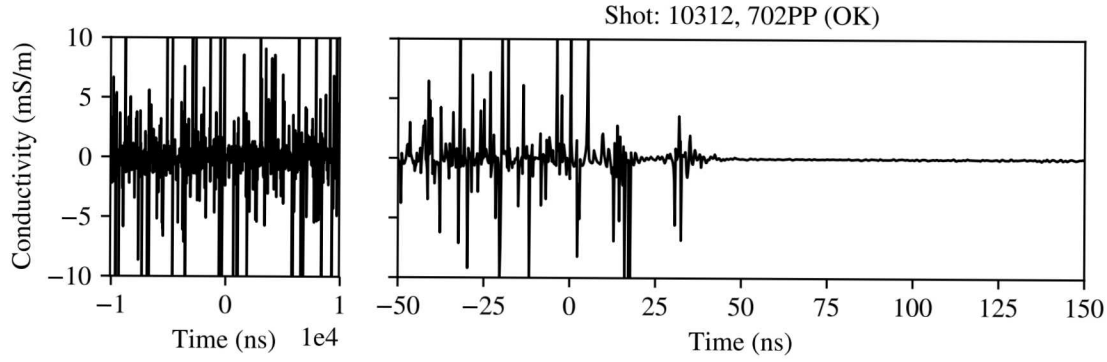
Shot: 10312, 702PP (OK)
Conductivity (mS/m)
10
5
0
−5
−10
−1
0
1
Time (ns)
1e4
−50
−25
0
25
50
75
100
125
150
Time (ns)

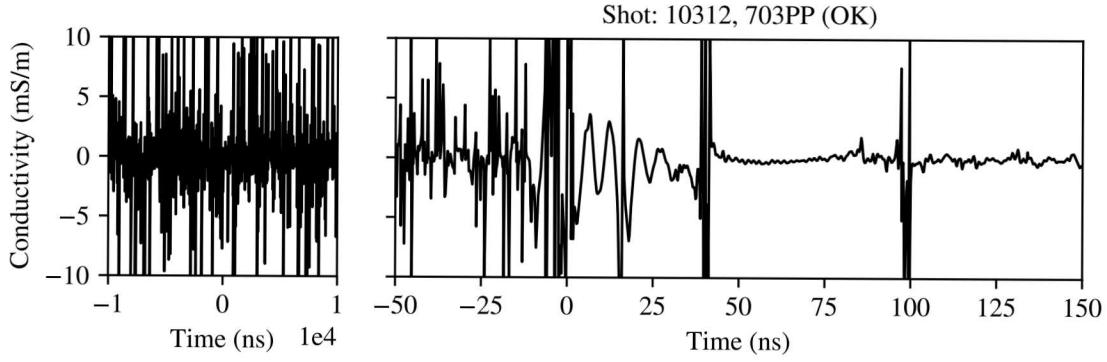
Shot: 10312, 703PP (OK)
Conductivity (mS/m)
10
5
0
−5
−10
−1
0
1
Time (ns)
1e4
−50
−25
0
25
50
75
100
125
150
Time (ns)

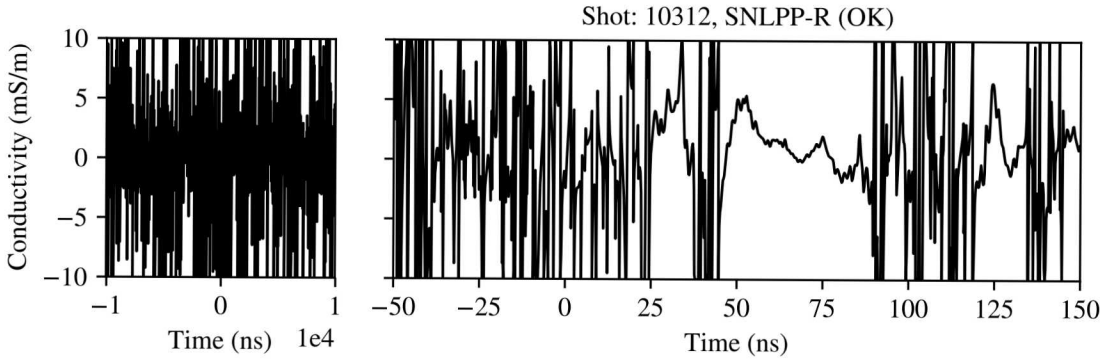
Shot: 10312, SNLPP-R (OK)
Conductivity (mS/m)
10
5
0
−5
−10
−1
0
1
Time (ns)
1e4
−50
−25
0
25
50
75
100
125
150
Time (ns)

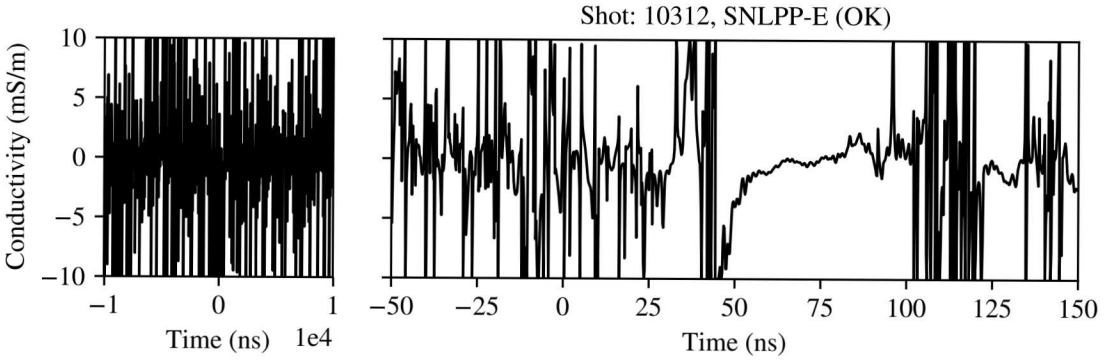
Shot: 10312, SNLPP-E (OK)
Conductivity (mS/m)
10
5
0
−5
−10
−1
0
1
Time (ns)
1e4
−50
−25
0
25
50
75
100
125
150
Time (ns)

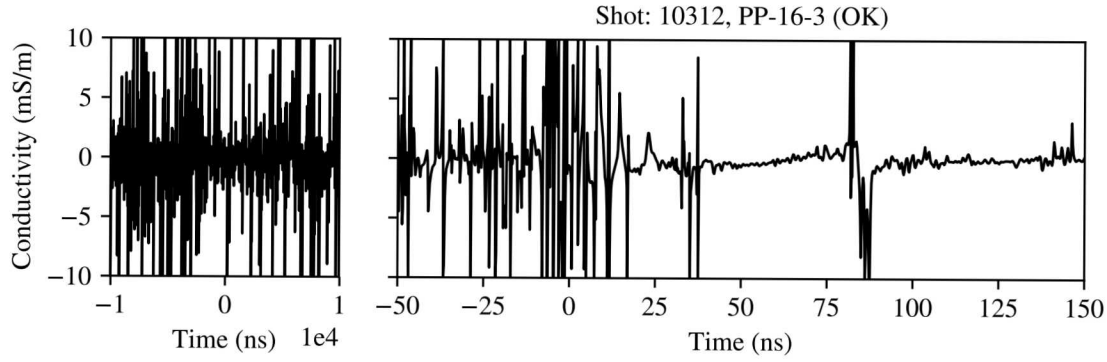
Shot: 10312, PP-16-3 (OK)
Conductivity (mS/m)
10
5
0
−5
−10
−1
0
1
Time (ns)
1e4
−50
−25
0
25
50
75
100
125
150
Time (ns)

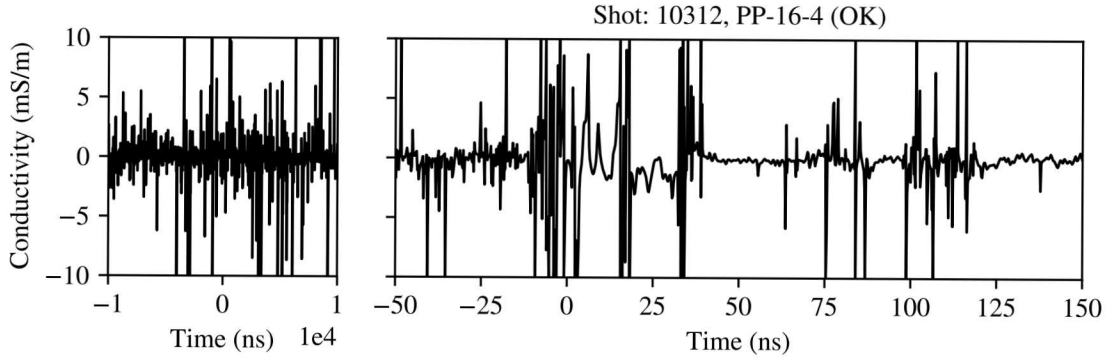
Shot: 10312, PP-16-4 (OK)
Conductivity (mS/m)
10
5
0
−5
−10
−1
0
1
Time (ns)
1e4
−50
−25
0
25
50
75
100
125
150
Time (ns)

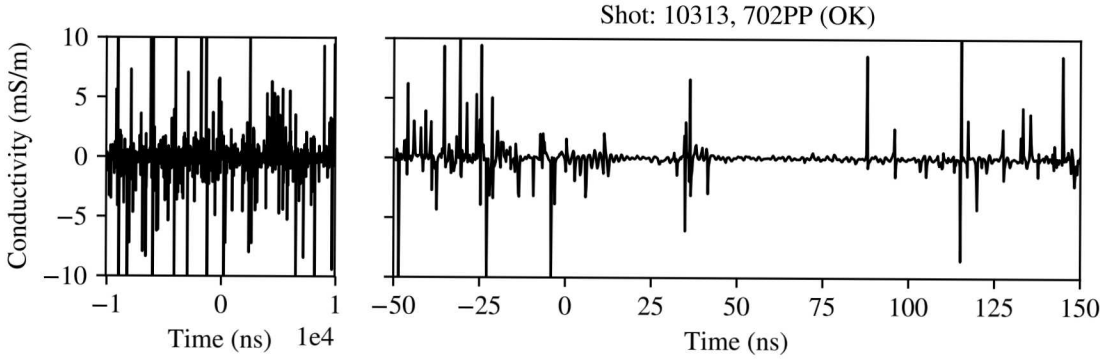
Shot: 10313, 702PP (OK)
Conductivity (mS/m)
10
5
0
−5
−10
−1
0
1
Time (ns)
1e4
−50
−25
0
25
50
75
100
125
150
Time (ns)

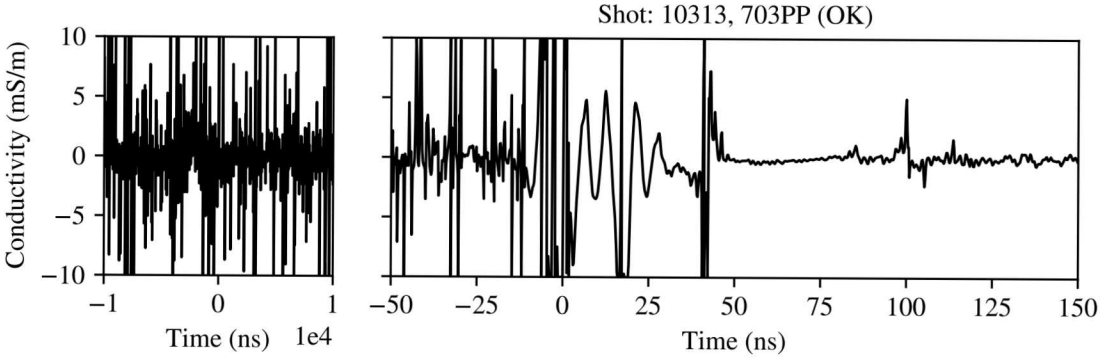
Shot: 10313, 703PP (OK)
Conductivity (mS/m)
10
5
0
−5
−10
−1
0
1
Time (ns)
1e4
−50
−25
0
25
50
75
100
125
150
Time (ns)

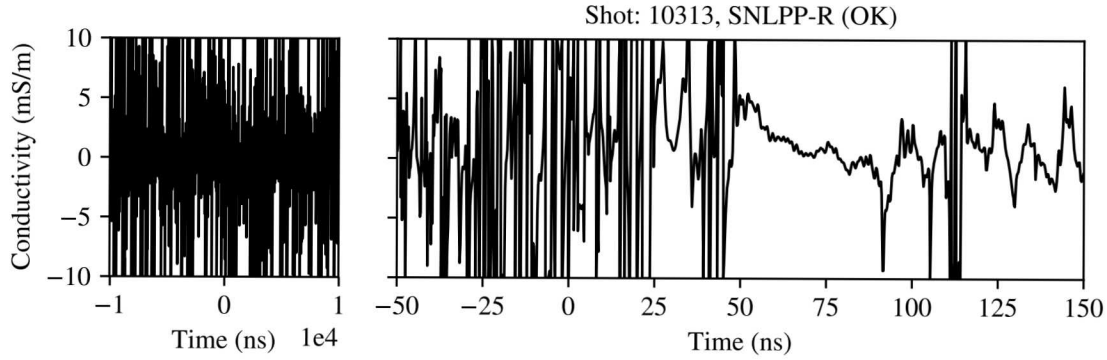
Shot: 10313, SNLPP-R (OK)
Conductivity (mS/m)
10
5
0
−5
−10
−1
0
1
Time (ns)
1e4
−50
−25
0
25
50
75
100
125
150
Time (ns)

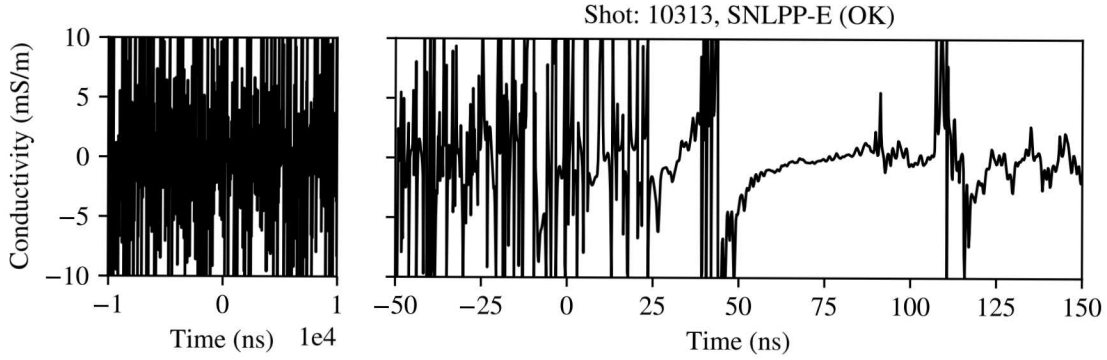
Shot: 10313, SNLPP-E (OK)
Conductivity (mS/m)
10
5
0
−5
−10
−1
0
1
Time (ns)
1e4
−50
−25
0
25
50
75
100
125
150
Time (ns)

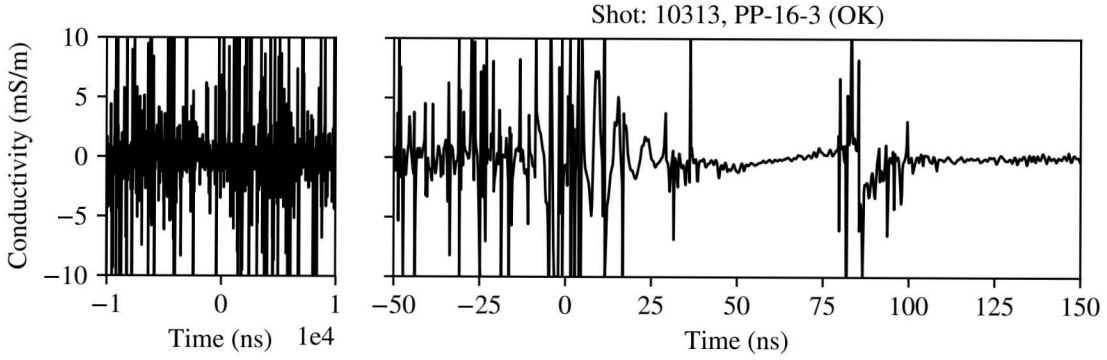
Shot: 10313, PP-16-3 (OK)
Conductivity (mS/m)
10
5
0
−5
−10
−1
0
1
Time (ns)
1e4
−50
−25
0
25
50
75
100
125
150
Time (ns)

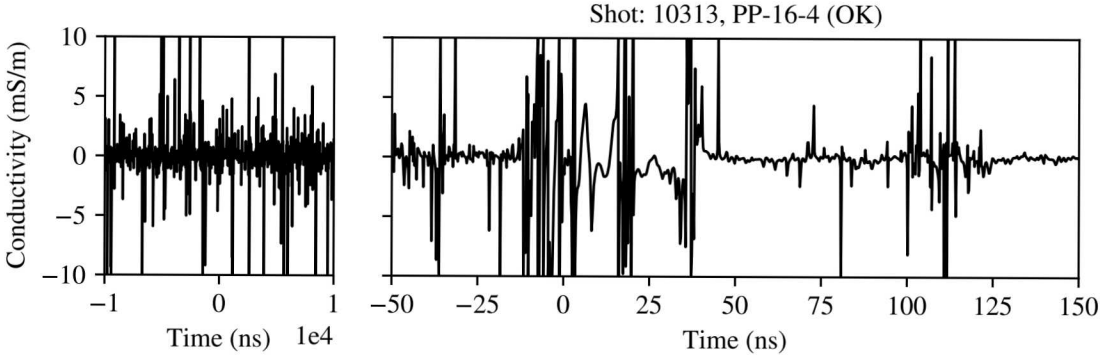
Shot: 10313, PP-16-4 (OK)
Conductivity (mS/m)
10
5
0
−5
−10
−1
0
1
Time (ns)
1e4
−50
−25
0
25
50
75
100
125
150
Time (ns)

DISTRIBUTION:

1 MS 0899 Technical Library, 9536 (electronic copy)


Sandia National Laboratories